# NUMERICAL SIMULATIONS OF THE GRAVITATIONAL GEODYNAMO AND ITS TIME SPECTRUM

**Dissertation**

zur Erlangung des Mathematisch-Naturwissenschaftlichen Doktorgrades
"Doctor rerum naturalium"
der Georg-August-Universität zu Göttingen

vorgelegt von
**VEDAT TANRIVERDİ**
aus Bahadın, Türkei

Göttingen, 2011

Referent: Prof. Dr. A. Tilgner

Korreferent: Prof. Dr. W. Glatzel

Tag der mündlichen Prüfung:

Dedicated to my family...

# Contents

**Figures** i

**Tables** ii

**1 Introduction** 1

**2 Theoretical Background** 3

2.1 Introduction to the Earth's Magnetic Field . . . 3

2.1.1 Historical introduction to geomagnetism . . . 3

2.1.2 Basic properties of the geomagnetic field . . . 4

2.1.3 Earth's magnetic field . . . 6

2.1.4 Earth's magnetic field's structure . . . 7

2.1.5 The main field . . . 9

2.1.6 Earth's structure . . . 11

2.1.7 The effects of Earth's crust on the magnetic field . . . 13

2.1.8 Paleomagnetism . . . 14

2.1.9 Processes of magnetization in rocks . . . 15

2.1.10 Magnetic field reversals . . . 16

2.2 Fluid Dynamics . . . 18

2.2.1 Solids, liquids and gases . . . 18

2.2.2 Fluid flow and kinematic viscosity . . . 19

2.2.3 Stress tensor . . . 21

2.2.4 Navier-Stokes equation . . . 22

2.2.5 Reynolds number . . . 24

2.2.6 Vorticity . . . 26

2.2.7 Coriolis force . . . 26

2.3 Dynamo Theory . . . 29

2.3.1 Origin of cosmological magnetic fields . . . 29

2.3.2 Maxwell's equations . . . 30

2.3.3 Induction equation . . . . . 32
2.3.4 The dynamo theory . . . . . 33
2.3.5 Heat equation and its effect on the dynamo . . . . . 34
2.3.6 The dynamo mechanism . . . . . 35
2.4 Dynamo Experiments . . . . . 38

**3 Numerical Dynamo Simulations 42**
3.1 Gravitational dynamos . . . . . 43
3.2 Convection driven dynamos . . . . . 55

**4 Phenomenological Models 65**
4.1 A single magnetic mode . . . . . 65
4.2 Several magnetic modes . . . . . 69
4.3 Spectral analyses . . . . . 74

**5 Conclusion 78**

**A Simulation results 81**

**Bibliography 87**

# List of Figures

2.1 The main elements of the geomagnetic field. The compass needle lies in the magnetic meridian containing the total field F, which is at an angle I, termed the inclination, to the horizontal. The inclination is reckoned positive downward and negative upward (northern and southern hemisphere, respectively). The deviation, D, of a compass needle from true north is referred to as the declination. The H and Z are horizontal and vertical components of F, respectively ([Merrill et al., 1998]). . . . . 5

2.2 Isogonic chart showing the variation in magnetic declination over the Earth's surface (1990) ([Merrill et al., 1998]). . . . . 6

2.3 Isolines of the radial component of the Earth's magnetic field at the surface ([Mueller and Stieglitz, 2003]). . . . . 7

2.4 Cross-section of the Earth's magnetosphere ([Bone, 2007]). . . . . 8

2.5 Power spectrum density of the dipole variations for the recording 0-160 Ma. Each colour represents a different data set for the magnetic field and reversals as determined by different groups. The black, gray, blue, red, green, brown, orange and pink dotted lines correspond to the work of Cande and Kent ([Cande and Kent, 1995]), intensity study in work of Cande and Kent ([Cande and Kent, 1995]), Constable et al. ([Constable et al., 1998]), Valet and Meynadiner ([Valet and Meynadier, 1993]), Channel ([Channell, 1999]), Gyudo and Valet ([Guyodo and Valet, 1999]), McMillan et al. ([McMillan et al., 2004]), Korte and Constable ([Korte and Constable, 2005]), respectively. For further information, refer to the original paper by Constable and Johnson ([Constable and Johnson, 2005]). . . . . 10

2.6 Earth's structure ([Rose and Kindersley, 2000]). . . . . 11

2.7 The radial component of the Earth's magnetic field at the Earth's core-mantle boundary reveals a strong dipole component ([Buffett, 2009]). . . 13

2.8 Time scale for geomagnetic reversals. The polarity similar to present-day is represented by black and the reverse represented by white one ([Cox, 1969]). . . . . 17

2.9 A schematic sketch of the force between simple un-ionized molecules with respect to distance $d$ between the centers of the molecules ([Batchelor, 1967]). 18

2.10 Viscous stresses in a simple flow ([Acheson, 1990]). . . . . 19

2.11 Fluid flow on a boundary layer ([Acheson, 1990]). . . . . 20

2.12 Development of the boundary layer and turbulence on a flat plate for a fluid ([Davidson, 2001]). . . . . 24

2.13 Characteristic flows in the presence of a cylinder with respect to different $Re$ ([Davidson, 2001]). . . . . 25

2.14 Rotating coordinate system $S'$ is represented with respect to inertial reference frame $S$. ([Dreizler and Ludde, 2010]). . . . . 27

2.15 A schematic sketch of the stretching and twisting of a magnetic field. (a) A torus carrying magnetic flux F is stretched to twice its size (b). (c) The twisted version of the stretched magnetic field. (d) The folded version of it. ([Childress and Gilbert, 1995]). . . . . 35

2.16 (a) A poloidal magnetic field. (b) The generation of an azimuthal magnetic field from a poloidal magnetic field. (c) The generation of a poloidal magnetic field from an azimuthal one ([Russell, 1999]). . . . . 36

2.17 The radial magnetic field and propeller rotation rate of the Riga experiment during one run in July 2003 ([Gailitis et al., 2004]). . . . . 38

2.18 PSD of (a) azimuthal and (b) axial magnetic fields for the Riga experiment for the run in June 2003 ([Gailitis et al., 2004]). . . . . 38

2.19 The x-component magnetic field from the von Karman sodium experiment ([Bourgoin et al., 2002]). . . . . 39

2.20 The PSD of the x-component magnetic field from the von Karman sodium experiment ([Bourgoin et al., 2002]). . . . . 39

2.21 The $B_{y3}$ component of the magnetic field taken from the result of the Karlsruhe experiment ([Muller et al., 2002]). . . . . 40

2.22 The PSD of the $B_{y3}$ component of the magnetic field measured at different sensors [Muller et al., 2002]. . . . . 40

3.1 Numerical results of the reversing gravitational dynamo at $Ra = 1 \cdot 10^6$, $Pm = 20$, $E = 6.5 \cdot 10^{-5}$ and $Pr = 1$. a) Time series of the kinetic energy. b) Time series of the magnetic energy. c) PSD of $u_{rms}$. d) PSD of $B_{rms}$. 45

3.2 Time series of the dipole moment at $Ra = 1 \cdot 10^6$, $Pm = 20$, $E = 6.5 \cdot 10^{-5}$ and $Pr = 1$. . . . . 45

3.3 Structure of the reversing gravitational dynamo at $Ra = 1 \cdot 10^6$, $Pm = 20$, $E = 6.5 \cdot 10^{-5}$ and $Pr = 1$. a) Radial component of the velocity field $u_r$ at $r = (r_i + r_o)/2$. b) Radial component of the magnetic field $B_r$ on the core mantle boundary. c) Radial component of the velocity field $u_r$ in the equatorial plane. d) Radial component of the magnetic field $B_r$ in the equatorial plane. . . . . 46

3.4 Numerical results of the reversing gravitational dynamo at $Ra = 1 \cdot 10^5$, $Pm = 20$, $E = 6.5 \cdot 10^{-5}$ and $Pr = 1$. a) Time series of the kinetic energy. b) Time series of the magnetic energy. c) PSD of $u_{rms}$. d) PSD of $B_{rms}$. 47

3.5 Time series of the dipole moment at $Ra = 1 \cdot 10^5$, $Pm = 20$, $E = 6.5 \cdot 10^{-5}$ and $Pr = 1$. . . . . 48

3.6 Structure of the reversing gravitational dynamo at $Ra = 1 \cdot 10^5$, $Pm = 20$, $E = 6.5 \cdot 10^{-5}$ and $Pr = 1$. a) Radial component of the velocity field $u_r$ at $r = (r_i + r_o)/2$. b) Radial component of the magnetic field $B_r$ on the core mantle boundary. c) Radial component of the velocity field $u_r$ in the equatorial plane. d) Radial component of the magnetic field $B_r$ in the equatorial plane. . . . . 48

3.7 Numerical results of the nonreversing gravitational dynamo at $Ra = 5 \cdot 10^4$, $Pm = 20$, $E = 6.5 \cdot 10^{-5}$ and $Pr = 1$. a) Time series of the kinetic energy. b) Time series of the magnetic energy. c) PSD of $u_{rms}$. d) PSD of $B_{rms}$. 49

3.8 Time series of the dipole moment at $Ra = 5 \cdot 10^4, Pm = 20, E = 6.5 \cdot 10^{-5}$ and $Pr = 1$. . . . . 50

3.9 Structure of the nonreversing gravitational dynamo at $Ra = 5 \cdot 10^4$, $Pm = 20$, $E = 6.5 \cdot 10^{-5}$ and $Pr = 1$. a) Radial component of the velocity field $u_r$ at $r = (r_i + r_o)/2$. b) Radial component of the magnetic field $B_r$ on the core mantle boundary. c) Radial component of the velocity field $u_r$ in the equatorial plane. d) Radial component of the magnetic field $B_r$ in the equatorial plane. . . . . 50

3.10 Numerical results of the reversing gravitational dynamo at $Ra = 1 \cdot 10^6$, $Pm = 5.75, 6, 13, 20, 25, 35$, $E = 6.5 \cdot 10^{-5}$ and $Pr = 1$. a) PSD of $u_{rms}$. b) PSD of $B_{rms}$. . . . . 51

3.11 Numerical results of the reversing gravitational dynamo at $Ra = 1 \cdot 10^5$, $Pm = 20, 30, 35, 50, 70, 100$, $E = 6.5 \cdot 10^{-5}$ and $Pr = 1$. a) PSD of $u_{rms}$. b) PSD of $B_{rms}$. . . . . 51

3.12 Numerical results of the nonreversing gravitational dynamo at $Ra = 5 \cdot 10^4$, $Pm = 7, 8, 10, 12, 15, 20, 30$, $E = 6.5 \cdot 10^{-5}$ and $Pr = 1$. a) PSD of $u_{rms}$. b) PSD of $B_{rms}$. . . . . 52

3.13 Comparison of some calculated parameters of the Earth compared to the simulations' values. There are four input parameter values. There are huge differences between the Earth's parameters and the simulations' parameters. This is also true for the output parameters. In the bottom panel, we see some estimated numbers related to the Earth's core ([D. Schmitt, 2009]). . . . . 54

3.14 Numerical results of the reversing dynamo at $Ra = 5 \cdot 10^5, Pm = 20, E = 6.5 \cdot 10^{-5}, Pr = 1$. a) Time series of the kinetic energy. b) Time series of the magnetic energy. c)PSD of $u_{rms}$. d ) PSD of $B_{rms}$. . . . . 56

3.15 Time series of the dipole moment at $Ra = 5 \cdot 10^5, Pm = 20, E = 6.5 \cdot 10^{-5}$ and $Pr = 1$. . . . . 57

3.16 Structure of the reversing dynamo at $Ra = 5 \cdot 10^5, Pm = 20, E = 6.5 \cdot 10^{-5}, Pr = 1$. a) Radial component of the velocity field $u_r$ at $r = (r_i + r_o)/2$. b) Radial component of the magnetic field $B_r$ on the core mantle boundary. c) Radial component of the velocity field $u_r$ in the equatorial plane. d) Radial component of the magnetic field $B_r$ in the equatorial plane. . . . . 57

3.17 Numerical results of the reversing dynamo at $Ra = 1 \cdot 10^5, Pm = 20, E = 6.5 \cdot 10^{-5}, Pr = 1$. a) Time series of the kinetic energy. b) Time series of the magnetic energy. c)PSD of $u_{rms}$. d ) PSD of $B_{rms}$. . . . . 58

3.18 Time series of the dipole moment at $Ra = 1 \cdot 10^5, Pm = 20, E = 6.5 \cdot 10^{-5}$ and $Pr = 1$. . . . . 59

3.19 Structure of the dynamo at $Ra = 1 \cdot 10^5, Pm = 20, E = 6.5 \cdot 10^{-5}, Pr = 1$. a) Radial component of the velocity field $u_r$ at $r = (r_i + r_o)/2$. b) Radial component of the magnetic field $B_r$ on the core mantle boundary. c) Radial component of the velocity field $u_r$ in the equatorial plane. d) Radial component of the magnetic field $B_r$ in the equatorial plane. . . . . 59

3.20 Numerical results of the reversing dynamo at $Ra = 5 \cdot 10^4, Pm = 20, E = 6.5 \cdot 10^{-5}, Pr = 1$. a) Time series of the kinetic energy. b) Time series of the magnetic energy. c) PSD of $u_{rms}$. d) PSD of $B_{rms}$. . . . . 60

3.21 Time series of the dipole moment at $Ra = 5 \cdot 10^4, Pm = 20, E = 6.5 \cdot 10^{-5}$ and $Pr = 1$. . . . . 60

3.22 Structure of the dynamo at $Ra = 5 \cdot 10^4, Pm = 20, E = 6.5 \cdot 10^{-5}, Pr = 1$. a) Radial component of the velocity field $u_r$ at $r = (r_i + r_o)/2$. b) Radial component of the magnetic field $B_r$ on the core mantle boundary. c) Radial component of the velocity field $u_r$ in the equatorial plane. d) Radial component of the magnetic field $B_r$ in the equatorial plane. . . . . 61

4.1 Numerical solution of Eq.(**??**) for $\langle\alpha\rangle = 0$. a) Time series of $\alpha$. b) Time series of $B$. c) PSD of $\alpha$. d) PSD of $B$; the straight line indicates the power law $1/f^2$. . . . . 67

4.2 Numerical solution of Eq.(**??**) for $\langle\alpha\rangle = 1$ and $\alpha$ has been filtered. a) Time series of $\alpha$. b) Time series of $B$. c) PSD of $\alpha$ and straight line indicates the power law $1/f^4$. d) PSD of $B$; the straight lines indicate the power laws $1/f^2$ and $1/f^6$. . . . . 67

4.3 The PSD of $B$, the solution of eq. **??**, as a function of frequency $f$ for $\langle\alpha\rangle = 1$ (red), 5 (green) and 15 (blue). The straight lines indicate the power laws $1/f^2$ and $1/f^6$. . . . . 69

4.4 Numerical solution of eq.(**??**) for $\langle\alpha_i\rangle = -10$. a) Time series of $\alpha_1$. b) Time series of $\sqrt{\sum B_i^2}$. c) PSD of $\alpha_1$. d) PSD of $\sqrt{\sum B_i^2}$; the straight line indicates the $1/f^2$ power law. . . . . 70

4.5 a) Time series of $\alpha$ with mean -0.01. b) PSD of $\alpha$; the straight line indicates the $1/f$ power law. . . . . 71

4.6 Numerical solutions of eq.(**??**) for $\langle\alpha_i\rangle = -0.01, -0.3, -5$. a) Time series of $\sqrt{\sum B_i^2}$ for $\langle\alpha_i\rangle = -0.01$. b) Time series of $\sqrt{\sum B_i^2}$ for $\langle\alpha_i\rangle = -0.3$. c) Time series of $\sqrt{\sum B_i^2}$ for $\langle\alpha_i\rangle = -5$. d) PSD of $\sqrt{\sum B_i^2}$ for $\langle\alpha_i\rangle = -0.01$; straight lines indicate the $1/f$ and $1/f^3$ power laws. e) PSD of $\sqrt{\sum B_i^2}$ for $\langle\alpha_i\rangle = -0.3$; straight lines indicate the $1/f^2$ and $1/f^3$ power laws. f) PSD of $\sqrt{\sum B_i^2}$ for $\langle\alpha_i\rangle = -5$; straight lines indicate the $1/f$ and $1/f^3$ power laws. . . . . 72

4.7 $cos\theta$ at $\langle\alpha_i\rangle = -0.01$ (green), -0.3 (blue) and -5 (red). . . . . 73

4.8 PSDs of the rhs (red line), ①+② (pink line), ①+③ (orange line), ②+③ (green line), ① (blue line), ② (turquoise line), ③ (black line). Straight lines show the $1/f$, $1/f^3$ and $f$ power laws. a) $\langle\alpha_i\rangle = -0.01$. b) $\langle\alpha_i\rangle = -0.3$. c) $\langle\alpha_i\rangle = -5$. . . . . 74

4.9 PSDs of the ①+② from direct spectrum calculation (red line) and from the correlation (green line) at $\langle\alpha_i\rangle = -5$. The straight lines represent $f$ and $1/f$. . . . . 75

4.10 PSDs of the rhs from direct spectrum calculation (red line) and from the correlation (green line). The straight line represents $1/f$. a) $\langle\alpha_i\rangle = -0.01$ b) $\langle\alpha_i\rangle = -0.3$ c) $\langle\alpha_i\rangle = -5$. . . . . 76

# List of Tables

3.1 *Gravitational dynamo simulation results. The first two column show control parameters $Ra$ and $Pm$. Since two of the parameters are constant for these results, they are not shown and $E = 6.5 \cdot 10^{-3}$ and $Pr = 1$. The next four columns show output parameters $\Lambda$, $Re$, $Rm$ and $Ro$. The 7th and 8th columns show low frequency interval power law ($Lf$ PL) and high frequency interval power law ($Hf$ PL) for the spectrum of $B_{rms}$, respectively. The 9th and 10th columns show similar power laws for the spectrum of $u_{rms}$.* . . . . . 53

3.2 *Convention driven dynamo simulation results. The first two column show control parameters $Ra$ and $Pm$. Since two of the parameters are constant for these results, they are not shown and $E = 6.5 \cdot 10^{-3}$ and $Pr = 1$. The next four columns show output parameters $\Lambda$, $Re$, $Rm$ and $Ro$. The 7th and 8th columns show low frequency interval power law ($Lf$ PL) and high frequency interval power law ($Hf$ PL) for the spectrum of $B_{rms}$, respectively. The 9th and 10th columns show similar power laws for the spectrum of $u_{rms}$.* . . . . . 62

A.1 *Gravitational dynamo simulation results. Columns from left to right: The first three columns show Rayleigh, Ekman and magnetic Prandtl numbers Ra, E and Pm respectively. The* $4^{th}$ *column depicts run duration corresponding to Earth's dipole decay time in years. The* $5^{th}$ *column represents the magnetic reversals (r:reversing, non:non-reversing). The* $6^{th}$ *column is the time average of dipole moment. The* $7^{th}$ *and* $8^{th}$ *columns are* $B_{rms}$ *and* $u_{rms}$ *respectively (in our case* $Ro = u_{rms}$ *due to scalings). The next three columns are three output parameters: Elsasser, Reynolds and magnetic Reynolds numbers* $\Lambda$*, Re and Rm, respectively. The next four columns show power laws for* $B_{rms}$ *and* $u_{rms}$ *in low and high frequencies Lf PL and Hf PL, respectively. The last colums stands for resolution (r1:33-64-64, r2:33-128-128 for spatial resolution and t1:*$5 \cdot 10^{-3}$*, t2:*$5 \cdot 10^{-4}$ *and t3:*$1 \cdot 10^{-3}$ *for the time step). The dashes correspond to either decaying cases or non-calculable situations. In all cases, the magnetic Prandtl number is set to 1,* $Pr = 1$*.* . . . . . 82

A.2 *Gravitational dynamo simulation results. Columns from left to right: The first three columns show Rayleigh, Ekman and magnetic Prandtl numbers Ra, E and Pm respectively. The* $4^{th}$ *column depicts run duration corresponding to Earth's dipole decay time in years. The* $5^{th}$ *column represents the magnetic reversals (r:reversing, non:non-reversing). The* $6^{th}$ *column is the time average of dipole moment. The* $7^{th}$ *and* $8^{th}$ *columns are* $B_{rms}$ *and* $u_{rms}$ *respectively (in our case* $Ro = u_{rms}$ *due to scalings). The next three columns are three output parameters: Elsasser, Reynolds and magnetic Reynolds numbers* $\Lambda$*, Re and Rm, respectively. The next four columns show power laws for* $B_{rms}$ *and* $u_{rms}$ *in low and high frequencies Lf PL and Hf PL, respectively. The last colums stands for resolution (r1:33-64-64, r2:33-128-128 for spatial resolution and t1:*$5 \cdot 10^{-3}$*, t2:*$5 \cdot 10^{-4}$ *and t3:*$1 \cdot 10^{-3}$ *for the time step). The dashes correspond to either decaying cases or non-calculable situations. In all cases, the magnetic Prandtl number is set to 1,* $Pr = 1$*.* . . . . . 83

A.3 *Gravitational dynamo simulation results. Columns from left to right: The first three columns show Rayleigh, Ekman and magnetic Prandtl numbers Ra, E and Pm respectively. The* $4^{th}$ *column depicts run duration corresponding to Earth's dipole decay time in years. The* $5^{th}$ *column represents the magnetic reversals (r:reversing, non:non-reversing). The* $6^{th}$ *column is the time average of dipole moment. The* $7^{th}$ *and* $8^{th}$ *columns are* $B_{rms}$ *and* $u_{rms}$ *respectively (in our case* $Ro = u_{rms}$ *due to scalings). The next three columns are three output parameters: Elsasser, Reynolds and magnetic Reynolds numbers* $\Lambda$*, Re and Rm, respectively. The next four columns show power laws for* $B_{rms}$ *and* $u_{rms}$ *in low and high frequencies Lf PL and Hf PL, respectively. The last colums stands for resolution (r1:33-64-64, r2:33-128-128 for spatial resolution and t1:*$5 \cdot 10^{-3}$*, t2:*$5 \cdot 10^{-4}$ *and t3:*$1 \cdot 10^{-3}$ *for the time step). The dashes correspond to either decaying cases or non-calculable situations. In all cases, the magnetic Prandtl number is set to 1,* $Pr = 1$. . . . . 84

A.4 *Convection driven dynamo simulation results. Columns from left to right: The first three columns show Rayleigh, Ekman and magnetic Prandtl numbers Ra, E and Pm respectively. The* $4^{th}$ *column depicts run duration corresponding to Earth's dipole decay time in years. The* $5^{th}$ *column represents the magnetic reversals (r:reversing, non:non-reversing). The* $6^{th}$ *column is the time average of dipole moment. The* $7^{th}$ *and* $8^{th}$ *columns are* $B_{rms}$ *and* $u_{rms}$ *respectively (in our case* $Ro = u_{rms}$ *due to scalings). The next three columns are three output parameters: Elsasser, Reynolds and magnetic Reynolds numbers* $\Lambda$*, Re and Rm, respectively. The next four columns show power laws for* $B_{rms}$ *and* $u_{rms}$ *in low and high frequencies Lf PL and Hf PL, respectively. The last colums stands for resolution (r1:33-64-64, r2:33-128-128 for spatial resolution and t1:*$5 \cdot 10^{-3}$*, t2:*$5 \cdot 10^{-4}$ *and t3:*$1 \cdot 10^{-3}$ *for the time step). In all cases, the magnetic Prandtl number is set to 1,* $Pr = 1$. . . . . 85

A.5 *Gravitational dynamo simulation results. Columns from left to right: The first three columns show Rayleigh, Ekman and magnetic Prandtl numbers* $Ra$, $E$ *and* $Pm$ *respectively. The* $4^{th}$ *column depicts run duration corresponding to Earth's dipole decay time in years. The* $5^{th}$ *column represents the magnetic reversals (r:reversing, non:non-reversing). The* $6^{th}$ *column is the time average of dipole moment. The* $7^{th}$ *and* $8^{th}$ *columns are* $B_{rms}$ *and* $u_{rms}$ *respectively (in our case* $Ro = u_{rms}$ *due to scalings). The next three columns are three output parameters: Elsasser, Reynolds and magnetic Reynolds numbers* $\Lambda$, $Re$ *and* $Rm$, *respectively. The next four columns show power laws for* $B_{rms}$ *and* $u_{rms}$ *in low and high frequencies* $Lf$ *PL and* $Hf$ *PL, respectively. The last colums stands for resolution (r1:33-64-64, r2:33-128-128 for spatial resolution and t1:*$5{\cdot}10^{-3}$, *t2:*$5{\cdot}10^{-4}$, *t3:*$1{\cdot}10^{-3}$ *and t4:*$5 \cdot 10^{-2}$ *for the time step). The dashes correspond to either decaying cases or non-calculable situations. In all cases, the magnetic Prandtl number is set to 1,* $Pr = 1$. . . . . 86

# 1 Introduction

This work will investigate numerical solutions for the dynamo. Dynamo is the accepted mechanism to explain the generation of a magnetic field. This generation takes place in most cosmological bodies, but it has taken centuries for us to understand the mechanism. Now, the dynamo theory is supported by calculations and experimental observations. In simplest terms, the main dynamo mechanism involves the evolution of the velocity field and the production of a magnetic field from this velocity field. However, there are still ongoing discussions about the dynamo and different mechanisms and structures have been proposed. Some of them are still hot topics in physics. In this work, we will numerically simulate electrically conducting fluid motion to obtain dynamo in spherical shells with two different approaches.

To begin our exploration into dynamo theory, we first give a historical introduction to the magnetic field of the Earth and describe how data has been collected throughout the centuries. Then, we discuss the Earth's magnetic field and its structure. We also explain the data collection regarding the past Earth's magnetic field and the methods of analysis.

In the second part of this work, we provide an introduction to fluid dynamics, since it forms the roots of the dynamo mechanism. Fluid motion is one of the key elements in the induction of the magnetic field and an introductory overview is given. The governing equations of fluid motion are considered and two of the basic elements of these equations, viscosity and stress tensor, are studied and explored. After this, we give a brief overview of Navier-Stokes equation, some related topics and a few non-dimensional parameters, which we will use later in the simulations.

In the third part, we give the basic equations of the dynamo theory together with electrodynamics. The generation of the magnetic field is described by the induction equation and we will derive it starting from the electrodynamics equations. Then we also give an introduction to the heat equation, which is another key factor in the dynamo theory. At

the end of this section, we discuss the generation of the magnetic field via the dynamo mechanism.

The fourth part of this work outlines some important dynamo experiments. The structure, results and spectrum analysis of three significant experiments are given.

The next section contains results in the form of numerical solutions for the dynamo and also interprets and analyzes these results. Firstly, we solve a gravitationally driven dynamo and analyze the results of the numerical solutions. Then we solve convection driven dynamos and compare these results with results from the gravitationally driven dynamo.

In the last section, we introduce a phenomenological model in order to to comprehensively explain the basic working principles of the induction equations and spectral analysis. We also discuss the consistency of our phenomenological model with the results of the numerical simulations of the previous section. Lastly, we summarize the work and make final conclusions.

# 2 Theoretical Background

## 2.1 Introduction to the Earth's Magnetic Field

In this section, we will summarize some basic concepts related with Earth's magnetic field. We will firstly start from the historical roots of geomagnetic research and continue with properties, structure and measurements of the Earth's magnetic field. We will also have a look at the structure of Earth and its effects on the magnetic field. Lastly, we will overview the magnetic reversals.

### 2.1.1 Historical introduction to geomagnetism

Research on geomagnetism has been ongoing for centuries. The first scientific book on the subject of geomagnetism was written by Gilbert in 1600 ([Jacobs, 1987]). Prior to this book, Petrus Peregrinus reported some experiments on magnetism in 1269 and this book was then published in 1558 ([McElhinny and McFadden, 2000]). Later, a number of great scientists also explored this topic, including Halley, Cavendish, Becquerel and Gauss. Presently, there are many scientists studying geomagnetism and many scientific works have been published on the topic. Before discussing developments in geomagnetism, we shall introduce and discuss development of the first geomagnetic tool: the compass. This tool forms the roots of geomagnetic research.

One of the first objects related to magnetism is the lodestone ([Jacobs, 1987]). The lodestone is a naturally magnetized magnetite and attracts iron. It was first studied scientifically by the Chinese. Despite their crude research, investigation of the lodestone by the Chinese led to the invention of the first compass in the first century A.D. ([Merrill and McElhinny, 1983], [Jacobs, 1987]). They discovered that a spoon made from lodestone spun on a polished surface came to rest pointing in the same direction every time ([Jacobs, 1987]). This was the earliest version of the compass. A Greek philosopher named Thales was also interested in magnets. Thales became the first philosopher

to study and observe magnets ([Merrill et al., 1998]). But Thales' work was not as sophisticated as that of the Chinese people. The first compass resembling that of today was described by Shen Kua. He also discussed the inclination of the compass. The compass arrived in Europe ca. 12th century by the sea route in the hands of Arabs ([Merrill et al., 1998]). The first European reference to the compass was made by the English monk Neckham in 1190 ([McElhinny and McFadden, 2000]). However European people did not yet know about inclination angle and this was rediscovered in the $15^{th}$ century. An interesting difference between the early Chinese and European compass was the pointing direction. The Chinese one pointed to the south and the European one to the north ([Merrill et al., 1998]).

A Chinese Buddhist astronomer named I-Hising made the first observations and records on magnetic declination about A.D. 720. However, declination was not known by the European people until Georg Hartman's observations in the early $15^{th}$ century. Hartman also continued his research on the Earth's magnetic field and magnetic inclination was first discovered by Hartman in 1544. Since he did not publish this study, it was rediscovered by Robert Norman in 1576. Another interesting fact about the compass was the crude consideration about its pointing direction. It was previously considered that the compass pointed towards a point in "the heavens". In 1546, George Mercator realized that the compass' needle pointed to somewhere on Earth and could not point toward "the heavens" ([Merrill et al., 1998]).

### 2.1.2 Basic properties of the geomagnetic field

Fig. 2.1 depicts the main elements of the geomagnetic field. The figure shows a 3-dimensional space on the Earth. The x-y plane corresponds to the surface of the Earth and the x-axis and y-axis points to the geographic north and east respectively . The third element of the space, the z-axis, points downward. F represents the Earth's total magnetic field. H represents its projection onto the x-y plane. The angle I is the inclination of the magnetic field from the horizontal and the angle D is the declination and shows the deviation of a compass needle from the geographic north.

Fig. 2.2 shows an isogonic chart which depicts the variation in magnetic declination over the Earth's surface in 1990. The magnetic poles are clearly visible on this graph and the declination angle changes due to the position on Earth. Around the geographic pole, the declination angle can take high values and its maximum value over the Equator is around

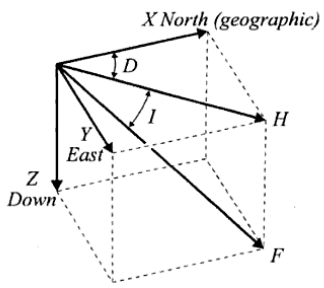


Fig. 2.1: The main elements of the geomagnetic field. The compass needle lies in the magnetic meridian containing the total field F, which is at an angle I, termed the inclination, to the horizontal. The inclination is reckoned positive downward and negative upward (northern and southern hemisphere, respectively). The deviation, D, of a compass needle from true north is referred to as the declination. The H and Z are horizontal and vertical components of F, respectively ([Merrill et al., 1998]).

10°. The reason for this is the 11° angle between the geographic pole and the geomagnetic pole when measured from the center of the Earth. Magnetic declination can change over time, an observation that was first made by Edmund Gunter in 1624. He measured the declination angle of 6.25° east at Limehoue, London, 42 years after William Borough's measurement of 11.25° east. Gunter could not confirm his measurement because of his death; however, his successors confirmed it and also found that the declination angle changes over time. This angle increased to 24° west and then started to decrease in the west again ([Jacobs, 1987]). This was the first evidence that the geomagnetic pole's position changes. This change is reminiscent of a rotation of the geomagnetic pole around the geographic North Pole, since declination angle can take values between the maximums of east and west angles and this angle gradually changes over time.

Gilbert, the writer of the first scientific book on geomagnetism, knew that the strength of the magnetism also changes. However, he could not measure it. The first relative measurement of the geomagnetic field was carried out in America by Baron Alexander von Humboldt, who measured relative intensity in 1798. This was not considered a physical measurement since it did not utilize basic physical quantities. The first physical measurement of magnetic intensity was made by Carl Friedrich Gauss in 1832 in Göttingen, Germany ([Jacobs, 1987]). Following Gauss, this measurement has been made at different locations all over the Earth and the technique only developed after the investments of electrical methods ([Jacobs, 1987]). The intensity of the Earth's magnetic field is measured in Tesla (T) units and its maximum value at the surface of the Earth

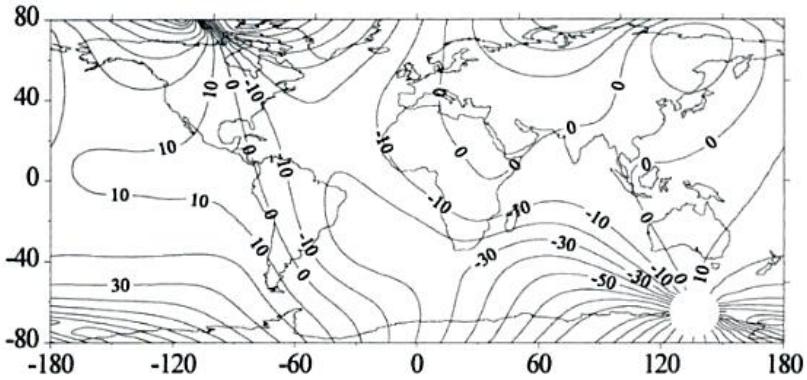


Fig. 2.2: Isogonic chart showing the variation in magnetic declination over the Earth's surface (1990) ([Merrill et al., 1998]).

(measured at the south pole) is 70 $\mu T$ ([McElhinny and McFadden, 2000]).

### 2.1.3 Earth's magnetic field

The Earth's magnetic field changes at every point. Measurement of the Earth's magnetic field F, includes both magnitude and direction. The magnitude and direction of F change with time. After determining direction using inclination and declination angle, one can calculate H and Z. These quantities are shown in fig. 2.1.

The Earth's magnetic field can change very rapidly within seconds and also slowly over decades. There are also changes taking place over millions of years and these slower changes are referred to as the geomagnetic secular variation ([Merrill et al., 1998]) or temporal variation. The main reason for these changes is the internal dynamics of the Earth. Another causative factor is the solar wind. The solar wind carries many charged particles, which can interact with the Earth's magnetic field as well as create their own magnetic fields. These charged particles constantly stream from the sun and affect the Earth's magnetic field each day. There are different factors affecting solar wind strength, the main ones being the 11-year solar cycle, the seasons and latitude. The biggest effects of the Sun on the Earth's magnetic field are observed during major solar eruptions that emit X-rays, ultraviolet radiation and high energy particles. Rarely, these effects can reach the value 5000 nT, which represents 7 per cent of the highest measured value. This interaction results in a change in the Earth's magnetic field. These are the main causes of the short term changes in the measured magnetic field ([Jacobs, 1987]).

The magnetic field measurements can be classified into two groups: 1) quantitative measurements, made by magnetometers, and 2) variations measurements, made by variometers. Previously, we mentioned that Gauss made the first quantitative measurement of the Earth's magnetic field and developments in electrical technology brought forth new techniques. Magnetic sensors can be divided into 5 groups: 1) Torsion magnetometers, 2) Nuclear magnetic resonance magnetometers, 3) Saturable-core magnetometers, 4) Induction magnetometers, and 5) Superconducting magnetometers. There are different magnetometers made from these sensors, e.g., observatory variometers, declinometer, QHM, BMZ, proton precession, Earth inductor, squid ([Jacobs, 1987], [Dyer, 2001]).

### 2.1.4 Earth's magnetic field's structure

We have mentioned the polar structure of the Earth's magnetic field. This polar structure takes a dipole form. In fig. 2.3, the radial component of the Earth's magnetic field at the Earth's surface is illustrated and the dipole structure is easily observed. The radial component of the Earth's magnetic field has negative values at the northern hemisphere and positive values at the southern hemisphere. One can also observe from the figure that its magnitude is greater at the poles compared to points between the poles and the Equator. This is the main property of the dipole field. However, fig. 2.3 also shows that the Earth's magnetic field is not a perfect dipole field. This field is comprised of 90% dipole structure and 10% higher order multipoles ([Mueller and Stieglitz, 2003]). This results mainly from internal dynamics, which will be discussed later.

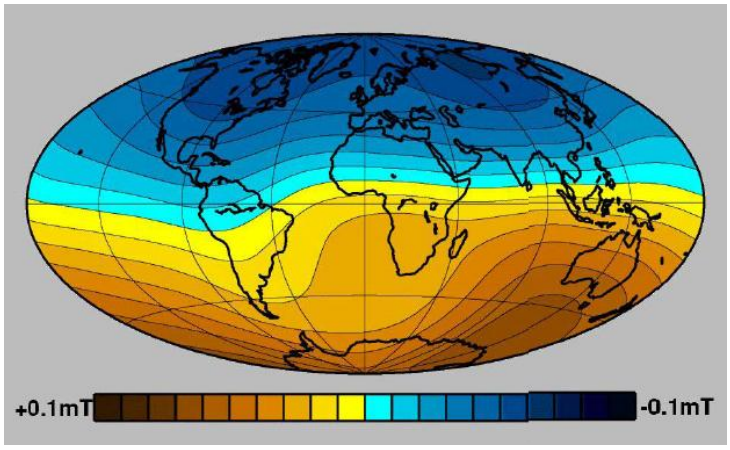


Fig. 2.3: Isolines of the radial component of the Earth's magnetic field at the surface ([Mueller and Stieglitz, 2003]).

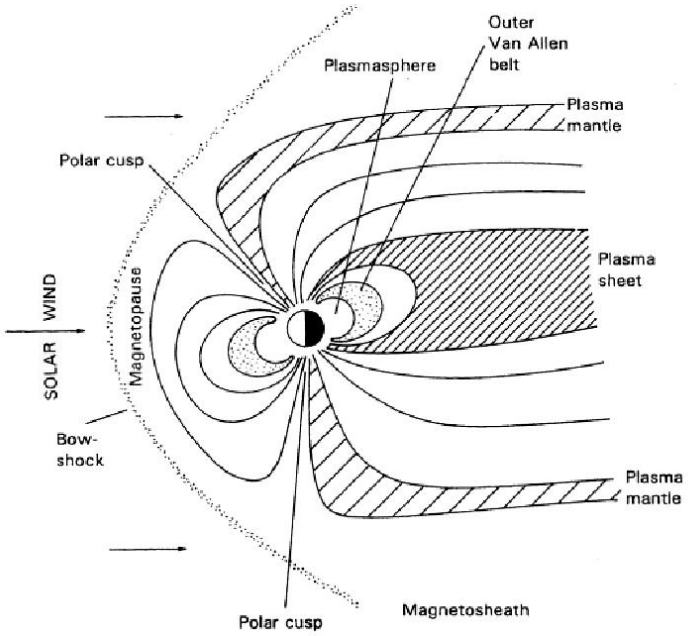


Fig. 2.4: Cross-section of the Earth's magnetosphere ([Bone, 2007]).

Fig. 2.4 depicts the cross-section of the Earth's magnetosphere. This picture was drawn using probes carried by satellites ([Bone, 2007]). The first direcly recognizable property is its asymmetric structure. This asymmetric structure arises due to the solar wind. If the solar wind were not present, the Earth's magnetosphere would look like a mostly dipolar structure. However, the solar wind creates a pressure on the day-side of the Earth's magnetic field due to interactions of the solar wind particles with the magnetic field. Fig. 2.4 also shows the magnetopause, which separates the Earth's environment from the interplanetary space. Because of the ten time faster motion of the Earth through solar wind particles, the solar wind flow is supersonic. This supersonic nature creates the bow shock, which is also shown in the figure. The bow shock is separated from the magnetopause by magnetosheath.

There are other different interactions in this structure. If only the pressure due to the solar wind were present, the magnetopause would resemble a water drop. This structure is not observed, however, due to the existence of the plasma sheet. The plasma sheet is the main cause of the open ends on the night-side of the Earth's magnetosphere. This open magnetic field, referred to as the geomagnetic tail, is considered to be connected with the interplanetary magnetic field ([Merrill et al., 1998]).

An interesting phenomenon related to the Earth's magnetic field is that the sunlight

ionizes some atoms and creates the ionosphere. Some of these ionized charged particles move along the magnetic field lines through the magnetosphere. Another interesting phenomenon can occur at the plasma sheet. When some of the charged particles from the solar wind are injected into the Earth's high atmosphere, this creates the auroras ([Bone, 2007]). Another structure seen in fig. 2.4 is the Van Allen belts. Some of the particles from the solar wind ionosphere can become trapped in regions of the magnetosphere These regions are called the Van Allen belts.

### 2.1.5 The main field

In 1600, Gilbert considered the Earth a great magnet ([Jacobs, 1987]). When a compass is located around the Equator, it points approximately to the geographic North Pole and when located close to the Poles, it can show different directions. This is one simple piece of evidence that demonstrates that the Earth's magnetic field is a vector quantity. As mentioned previously, this magnetic field is affected by the Earth's internal properties and the solar wind. These two factors affect the magnetic field in different ways. The Earth's internal dynamics and crust are two of the important factors that affects the Earth's magnetic field. The solar winds, in general, affect the magnetic field via changes in the ionosphere. In the ionosphere, both the Earth's magnetic field and charged particles traveling in the solar wind are at play. Their interaction changes the motion of charged particles in different ways and this affects the Earth's magnetic field. Thus, the Earth's magnetic field is the total of the magnetic field produced by the Earth's core, crust, ionosphere and other additional minimal effects. The largest contribution comes from the core and this field is referred to as the main field. The approximate values for the Earth's magnetic field is $60\mu T$ at the Pole and $30\mu T$ at the Equator. The maximum change in the magnetic field due to secular variation is about 1% per year. The changes due to Earth's crust, ionosphere and some other effects can vary between 1 nT and thousands nT. Therefore, these changes only result in small fluctations, which do not have a large overall effect on the main field.

Fig. 2.5 shows the power spectrum density (PSD) of the dipole variations. This graph was obtained by using the measurements of the magnetic field and reversal recordings of different laboratory groups; different colours in the graph represent different recordings. There are three regions shown in the graph, each corresponding to different perceptions about the various processes. The first region, reversal rate changes, shows the long-term reversal rate of the dipole variations. The second region, average reversal crypto-chron

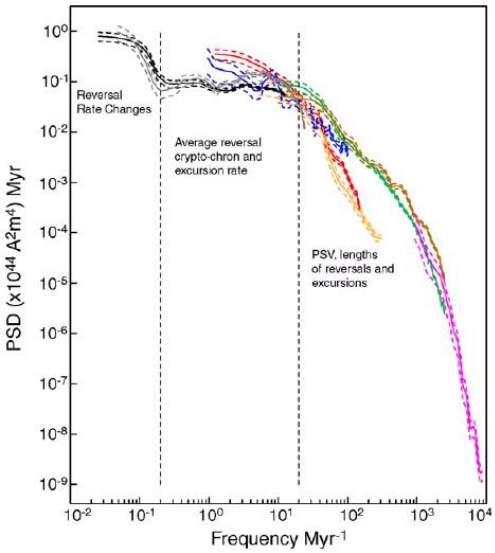


Fig. 2.5: Power spectrum density of the dipole variations for the recording 0-160 Ma. Each colour represents a different data set for the magnetic field and reversals as determined by different groups. The black, gray, blue, red, green, brown, orange and pink dotted lines correspond to the work of Cande and Kent ([Cande and Kent, 1995]), intensity study in work of Cande and Kent ([Cande and Kent, 1995]), Constable et al. ([Constable et al., 1998]), Valet and Meynadiner ([Valet and Meynadier, 1993]), Channel ([Channell, 1999]), Gyudo and Valet ([Guyodo and Valet, 1999]), McMillan et al. ([McMillan et al., 2004]), Korte and Constable ([Korte and Constable, 2005]), respectively. For further information, refer to the original paper by Constable and Johnson ([Constable and Johnson, 2005]).

and excursion rate, shows the average reversal rate between 0.02 and $10Myr^{-1}$. There is an inconsistency in this region between the black and red curves. In this region, the PSD of the black curve is constant and reversals occur at each frequency with nearly equal power distribution. The red curve has a slope of nearly $1/f$. This inconsistency may be due to the long-term paleointensity variations for different reversal rates. The last region shows paleosecular variation (PSV), lengths of reversals and excursions. The power falls off faster in this region, which is related to the changes for 0-50 ka time intervals ([Constable and Johnson, 2005]).

In previous sections, we introduced the dipole property of the Earth's magnetic field and supported these properties with observational results. We also showed that there can be many changes to this field and this field can be represented by using Maxwell's equations.

The best way to write the solution is to use spherical harmonics. The advantages for using spherical harmonics as well as the description of spherical harmonics can be found in books ([Jacobs, 1994]).

### 2.1.6 Earth's structure

We have known for thousands of years that the Earth has a spherical shape. However, less is known about its inner structure. The occurrence of earthquakes as well as magma eruptions provides some information as to the Earth's inner structure. Earthquakes send out seismic waves in all directions. Larger intensity earthquakes send out seismic waves and the velocity of these waves depend on the composition, mineralogy, temperature and pressure of the Earth's inner components. This helps us to learn more about the Earth's inner structure. Fig. 2.6 is a representative illustration of the Earth's inner structure. It is composed of 3 main parts: inner core, outer core and mantle. The crust forms the outermost layer ([Brown et al., 1992]).

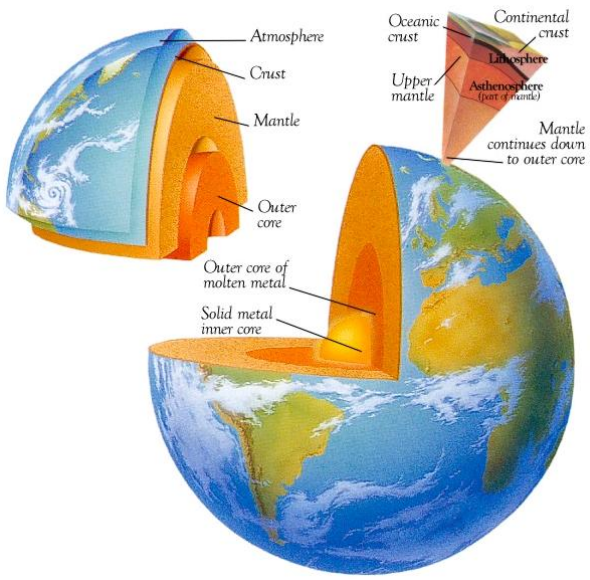


Fig. 2.6: Earth's structure ([Rose and Kindersley, 2000]).

Further details on these components will follow after a short description of the formation of the Earth. Scientific evidence shows that the Sun, Earth and other components of the solar system were formed from the remaining solar nebula of the supernova explosion. There is a similarity in the abundances of the elements in these. These abundances are

also affected by gravitational interactions, other types of interactions and the positions and sizes of the components of the solar system. These parameters and interactions also determine the abundances of the elements in the Earth's components.

The solid inner core is the centremost part of the Earth. Its radius is about $1200km$, which is comparable with the radius of the Moon ($1700km$) ([Fix, 2004]). However, the density of the inner core is much higher than the average values of the Earth and Moon. This is because it is constituted from iron-nickel alloy and also some sulfur-iron alloy ([Pater and Lissauer, 2001]). Some models predict that the temperature of the inner core is $5000 - 7500K$, but these are only model results and therefore not fully reliable ([McFadden, 2007]). Directly after formation, the Earth was more or less uniform in terms of composition and the distribution of chemicals. Later, due to the gravitational interaction, dense materials sank down to the center of the Earth. The denser elements (iron and nickel) accumulated at the center and over time, with the help of pressure, these elements constituted an alloy and solidified. Another property of the inner core is its differential rotation. Seismic studies have provided some evidence showing that the inner core rotates $1^\circ$ of longitude per year faster than the other parts of the Earth ([Fix, 2004]).

The Earth's outer core completely surrounds the inner solid core and it is liquid. Its shape looks like a spherical shell and it begins at the $1200km$ point where the inner core ends. The transition region is termed the inner core boundary (ICB). This liquid outer core continues to $3500km$, where the mantle starts. This region between the outer core and the mantle is called the core mantle boundary (CMB). The outer core is also mainly composed of iron, but density calculations estimate that there should be a 10% lighter elements composition. The models predict an outer core temperature between 3000 and $5000K$ ([McFadden, 2007]). Due to this high temperature, nearly all elements are in their ionized forms. This means that the outer core is completely electrically conducting and the motion of this electrically conducting material produces a magnetic field, which will be described in detail later.

The mantle can be subdivided into the lower mantle, transition zone and upper mantle, with all maintaining a spherical shell shape. The lower mantle lies in the radius between 3500 and $5700km$ ([McFadden, 2007]). Seventy percent of the mass of the solid Earth is located in the lower mantle, which is mainly composed of magnesium silicate rocks ([Schubert et al., 2001]). This region is mostly solid; however, high temperatures ($900 - 3000K$) provide a slow flow within the lower mantle. The next stage is the transition

zone, which lies between the radius of 5700 and 5960$km$ ([McFadden, 2007]). This region is defined due to seismic wave velocity discontinuity and is mostly composed of olivine and pyroxene-garnet ([Schubert et al., 2001]). The last subdivision of the mantle is the upper mantle, which lies between the radius of 5960 and 6335$km$. This regions begins 25$km$ below the crust. It is composed of olivine, pyroxene and some magnesium and iron ([McFadden, 2007]).

### 2.1.7 The effects of Earth's crust on the magnetic field

The main source of the Earth's magnetic field is dynamo action in the core. As mentioned earlier, the crust also affects the magnetic field and this effect can be both constructive and destructive. There are two main reasons for this effect. The first reason is related to the magnetic susceptibility of the rocks. This effect can change depending on whether the magnetic susceptibility is positive or negative. If the rocks are diamagnetic (negative magnetic susceptibility), then the effect is destructive. On the other hand, for paramagnetic, ferromagnetic or ferrimagnetic rocks, the effect is constructive . We will elaborate on these effects later in the next section. The second reason for the constructive or destructive effect is permanent magnetization. Permanent magnetization occurs if the temperature is below Curie isotherm. This effect is observed for cooled lavas. When hotter rocks are cooled under the magnetic field, then there will be a frozen magnetization inside the rocks and this will also contribute the Earth's magnetic field. Since the Earth's magnetic field changes with time, this effect is can also be constructive or destructive.

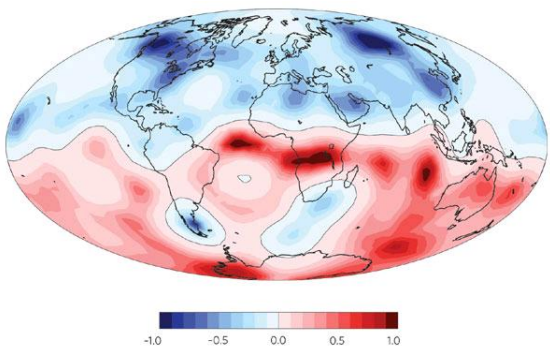


Fig. 2.7: The radial component of the Earth's magnetic field at the Earth's core-mantle boundary reveals a strong dipole component ([Buffett, 2009]).

Fig. 2.7 depicts reproduced large-scale patches of magnetic fluxes at the Earth's core-mantle boundary. These are similar to structures inferred at the Earth's core-mantle

boundary from surface observations. As with the Earth's surface fig. 2.3, the dipole field is still the strongest. However, its dipolar structure is changed compared to at the surface. Higher moments are also in play, which can be easily seen from the patterns around the Equator. Comparing fig. 2.3 with fig. 2.7, higher moments' contributions can be observed.

The mentioned effects of the crust on the Earth's magnetic field are region-dependent, intense and have a short wavelength. It is not always possible to calculate the crust effects; however, taking advantage of these properties, one can find them in some cases. To do so, ship or aircraft data are used. In general, if the isolation of the field is determined within a region, then it is said that these fields originate from the crust.

### 2.1.8 Paleomagnetism

The study of magnetism in fossil records of the Earth magnetism is called paleomagnetism. The crust's magnetic field discussed above is related to this topic. At the end of the $18^{th}$ century, it was known that some rocks possessed magnetization and this magnetization could affect the compass. In the $19^{th}$ century, intense magnetization in rock exposures were explained this way. The first studies made by Delesse and Melloni determined that some recent lavas were magnetized parallel to the Earth magnetization. At the beginning of the $20^{th}$ century, David and Brunhes reported that some older lavas were magnetized approximately anti-parallel to the Earth's magnetic field. Later confirmation of this study led people to conclude that the polarity of the Earth's magnetic field had reversed ([McElhinny and McFadden, 2000]). These findings became the starting points for paleomagnetism.

Paleomagnetism makes use of a few magnetic materials inside formed rocks. These magnetic materials mainly consist of different iron oxides and sulphides. Primary magnetization occurs when the rock formation process is complete. This provides the main source of the knowledge about the magnetic field of the Earth. After the formation of a rock, this primary magnetization can be partly or wholly damaged and new magnetization may occur. These new magnetizations are referred to as secondary magnetization. They can cause a sort of "noise" for magnetic field measurements and should not be utilized. Eliminating these confounding effects of secondary magnetization is one of the main problems in paleomagnetism research ([Jacobs, 1994]). The magnetic materials in rocks are used to find both the magnitude and direction of the Earth's magnetic field.

Some archaeological materials are also used to measure the Earth's past magnetic field and this technique is called archeomagnetism ([McElhinny and McFadden, 2000]).

The materials have different magnetic properties, and are classified according to these properties as: diamagnetic, paramagnetic, ferromagnetic and ferrimagnetic. Diamagnetism is common to all substances. It occurs due to the motion of orbital electrons. The motion of electrons under a magnetic field produces a negative induced magnetic moment. This reduces the total magnetic field, which is called diamagnetism. Although diamagnetism is valid for all substances, it becomes negligible in the presence of any other magnetic effect. The magnetic susceptibility of the diamagnetic materials is negative and is of the order of $10^{-5}$. If a material has a net positive magnetic moment, this magnetic moment is aligned in the direction of the applied magnetic field. This alignment, known as paramagnetism, contributes to the magnetic field in a positive way and its value lies between $10^{-5}$ and $10^{-3}$. On the other hand, some magnetic materials can strongly contribute to the magnetic field. This material is then said to be ferromagnetic. Ferromagnetic materials have more valance electrons, and these electrons and their spins are aligned with the applied magnetic field. This is also observed if the external magnetic field is zero. However, for this to occur, the temperature of the substance should be less than the Curie temperature. Above the Curie temperature, all electrons move freely and no magnetization is present in the material. These alignments are in general found in domains. In some cases, these domains can cancel each others' effect and then an antiferromagnetism phenomenon occurs. Occasionally, due to these random alignments, the magnetic property is reduced and this is named ferrimagnetism ([McElhinny and McFadden, 2000]). Magnetite is an iron-oxides and a ferrimagnetic material. Its naturally magnetized form is called the lodestone, a material which initiated the study of magnetism (Section 2.1.1). In paleomagnetism, magnetite is one of key materials for studying magnetic field records.

### 2.1.9 Processes of magnetization in rocks

There are different processes of magnetization in rocks and understanding these types of magnetization are important for defining reversals. The following section will briefly describe these processes.

The first type of magnetization is called thermoremanent magnetization (TRM). In TRM, rocks from lavas cool from a temperature higher than the Curie temperature. The iron

oxides in these rocks align in the direction of the Earth's magnetism. After cooling, magnetization due to this alignment becomes "frozen" inside the rocks. Other types of magnetization are referred to as depositional and post-depositional remanent magnetization (DRM and PDRM). These types of magnetization require sediments of magnetized particles. These magnetized particles are eroded from previously formed rocks. During, deposition, these magnetized particles are aligned in the direction of Earth's magnetic field; this procedure is named DRM. If the remanent magnetization is free to rotate in the sediments, then they can be aligned later, which is referred to the PDRM. The next type of magnetization is termed isothermal remanent magnetization (IRM), which occurs when magnetic materials acquire magnetization without heating. Viscous remanent magnetization (VRM) is a type of magnetization closely connected to IRM. This type of magnetization occurs in slowly occurring IRM. As time passes, more parts of the magnetic material become magnetized in the VRM process. The last type of magnetization is chemical remanent magnetization (CRM). After the formation of certain rocks, their magnetization grains will grow due to chemical changes. After reaching its critical volume, the rock's magnetization aligns with the Earth's magnetic field and this magnetization will be dated at this time ([Jacobs, 1994]).

### 2.1.10 Magnetic field reversals

We have geomagnetic records dating back to the $19^{th}$ century from scientists and mariners. However, records of the Earth's magnetic reversals are different because they occur over thousands to millions of years . Paleomagnetism has provided some indirect data on magnetic reversals. These data show that magnetic pole reversals have occurred many times. This is one of the great successes of paleomagnetism. As shown in fig. 2.3, Earth's magnetic field is mainly dipole. Therefore, a nearly 180° change in the axial dipole field is defined as a magnetic field reversal of the Earth ([McElhinny and McFadden, 2000]). The paleomagnetic observations can create problems for interpreting and/or predicting the occurrence of reversals.

Self-reversals can also occur after the first magnetization in the magnetized rocks. After some time passes from the magnetic alignment along the Earth's magnetic field, domains inside the magnetized substance can be produced. These domains reverse due to interactions with the main and first magnetization. So, these self-reversals should be carefully analyzed. However, this procedure hardly occurs and most of the reversals shown in chronology are real reversals ([McElhinny and McFadden, 2000]).

There are some tests that can be conducted to determine the reliability of reversal data. Firstly, there should be an agreement between the magnetization polarity of the igneous rock and the baked rock for studies of the baked contacts. Secondly, different rocks around the world should show an agreement in polarity. Lastly, polarity reversals should be found in sequences. These are considered the basic requirements for defining a magnetic reversal ([McElhinny and McFadden, 2000]).

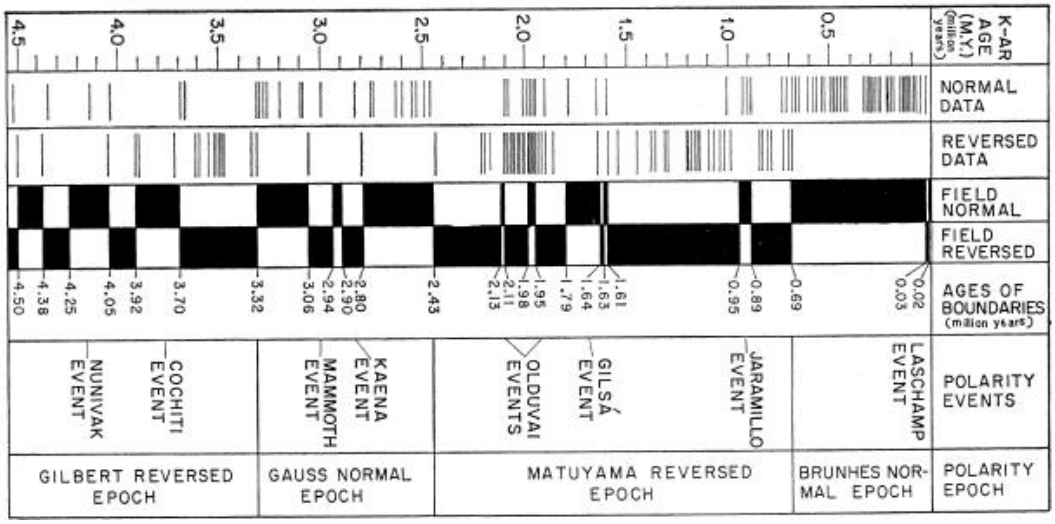


Fig. 2.8: Time scale for geomagnetic reversals. The polarity similar to present-day is represented by black and the reverse represented by white one ([Cox, 1969]).

Fig. 2.8 shows the magnetic polarity reversals of the Earth. The black parts correspond to polarity similar to present day and white parts correspond to reversed ones. The first row shows the dates, the second and third rows show data for the direction of magnetic field (the normal and reversed magnetic fields, respectively). The $4^{th}$ and $5^{th}$ rows show black and white representations. The $6^{th}$ row shows the age boundaries and the 7th row names the reversal events. The last row shows the names of epochs. The time-scale dates back to 4.5 million ages. In the previous magnetizations, the error in measurements are too great, so the data is not exact. This figure shows some of the studied reversals and it is clear that magnetic reversals are common occurrences throughout the history of the Earth.

## 2.2 Fluid Dynamics

In this section, we will start with the properties of the different phases of materials. Then we will continue with the analyze of the fluid motion by considering viscosity and stress tensor and we will give the derivation of Navier-Stokes equation. Then we will consider Reynolds number and its relation with fluid flow. Lastly, we will overview the vorticity and Coriolis force.

### 2.2.1 Solids, liquids and gases

The distinction between solids, liquids and gases is not always clear. Liquids and gases can be combined into one class called fluids. The basic difference between solids and fluids is that solids have a preferred shape, while fluids do not.

If one applies force to a solid or fluid, the solid will take back its original form after withdrawal of the force; the fluid, however, will not. Some substances show simultaneous properties of both solids and fluids, such as jelly, polymer solutions and egg whites. These substances are said to be viscoelastic ([Kundu and Cohen, 2002]). For these substances, there is order among the molecules, but this order is different than solids and is not as regular. In fluids, there is not any order among molecules.

The difference between liquids and gases is related to the environment. Pressure is a key factor for discrimination of fluids. In the absence of pressure, all liquids will turn to gases. However, in the presence of pressure, a gas expands and occupies the available volume, while a liquid does not.

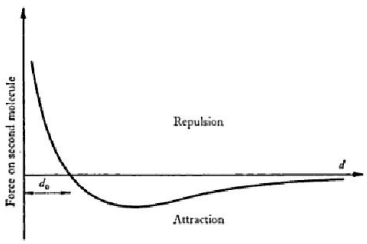


Fig. 2.9: A schematic sketch of the force between simple un-ionized molecules with respect to distance $d$ between the centers of the molecules ([Batchelor, 1967]).

Fig. 2.9 shows how the force between molecules changes with respect to the distance $d$ between the centers of the molecules. As shown in the figure, the force is repulsive for

distances smaller than the $d_0$, and attractive for greater distances. The distance $d_0$, where the force between molecules is zero, is different for different types of molecules. In solids, $d_0$ is smaller and the minimum point on this graph is lower. This is due to the strong attraction among the molecules of solids. As a substance changes from solid to liquid and gas, $d_0$ becomes greater and the minimum of this curve approaches zero. Therefore, at a fixed temperature, since the force for solids is stronger, the movements of the molecules due to temperature are small. Since a solid preserves its form, the movements should be very small compared to $d_0$. For liquids, this motion should be at the order of $d_0$ since the molecules can change their order. Lastly, for gases, the bonds between the molecules are really weak and molecules move independently from one another. In this case, the movements of molecules should be much bigger than $d_0$.

Thus, a solid is defined as the form of a substance that has strong molecular interactions, an ordered molecular arrangement and small thermal motions of the molecules compared to $d_0$. For a liquid, the molecular interactions are mid-range between a solid and gas; the molecules are partially ordered; and thermal motion is at the order of $d_0$. Lastly, a gas has weak molecular interactions, no order at all in molecular arrangement and a much larger thermal motion than $d_0$ [Batchelor, 1967].

### 2.2.2 Fluid flow and kinematic viscosity

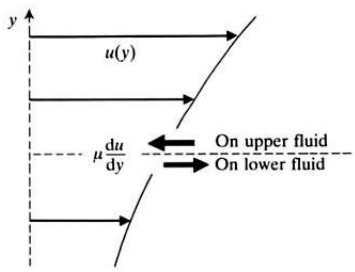


Fig. 2.10: Viscous stresses in a simple flow ([Acheson, 1990]).

Fig. 2.10 illustrates simple shear flow. Molecules flow in a fluid and there is an interaction among these molecules, as previously shown in fig. 2.9. This interaction, in combination with collisions, plays a crucial role in determining the motion of the fluid. This is a really complicated process. However, there is simple way of handling this. First, consider velocity as a function of $u(y)$. As shown in fig. 2.10, $u(y)$ also increases as y increases. Due to mentioned interactions, the faster part of fluid motion forces the remaining slower

part of fluid to move faster and the slower part of the fluid also forces the remaining faster part of fluid to move slower. This is represented by the bold arrows in fig. 2.10. The mentioned shear stress can be expressed in terms of velocity gradient as

$$\tau = \mu \frac{du}{dy} \tag{2.1}$$

where $\mu$ is related with the properties of the fluid and is called the coefficient of viscosity ([Acheson, 1990]). This relation is valid for Newtonian viscous fluids. The main property of Newtonian fluids is that the proportionality of flow to the viscosity is linear. For non-Newtonian fluids, viscosity is not constant and can be nonlinear and time dependent. There are many different properties of these fluids, which will not be discussed. Referring back to Newtonian fluids, the coefficient of viscosity can be defined in a more common way: as kinematic viscosity $\nu$

$$\nu = \mu/\rho \tag{2.2}$$

where $\rho$ is the density of the fluid. In general, these are dependent on substance and temperature.

Fig. 2.10 shows only one aspect of fluid flow. However, in general, fluids flow on surfaces and these surfaces affect flow. To understand this point, we should consider boundaries and corresponding boundary layers. Fig. 2.11 shows the motion of fluid on a boundary surface. After a point, a boundary layer is produced and in that layer, the velocity gradient is not equal to zero. In the other parts of the fluid motion, flow is steady and the velocity gradient is much smaller than the velocity gradient at the boundary layer. If the boundary surface is fixed, then there is not any motion in the surface and no-slip boundary conditions are valid. The velocity should decrease gradually to zero as one approaches the boundary layer.

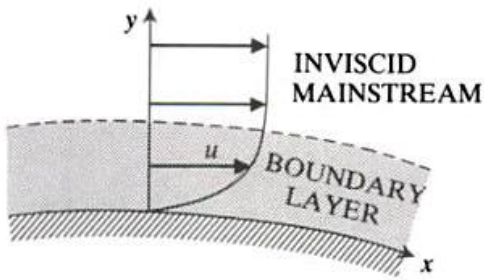


Fig. 2.11: Fluid flow on a boundary layer ([Acheson, 1990]).

If there is no boundary layer, this is referred to as free-slip boundary conditions. In some

cases with boundaries, free-slip boundary conditions can also be used. In these cases, the viscosity of the fluid should be very small and this small viscosity produces a really thin boundary layer. The thin boundary layer, in general, does not affect the motion of the fluid overall. In some cases, however, even if the viscosity is really small, turbulences may arise due to the boundary layer. When these turbulences are observed, usage of free-slip boundary conditions will fail ([Acheson, 1990]).

### 2.2.3 Stress tensor

Eq. 2.1 is valid for flow shown in the fig. 2.10. In the general case, however, velocity can depend on all components, and not solely on $y$. Then eq. 2.1 must be generalized and in this case, $\tau$ replaced by stress tensor $\tau_{ij}$ . For a fluid at rest, stress is independent of orientation and can be written as

$$\tau_{ij} = -p\delta_{ij} \tag{2.3}$$

where $p$ is the thermodynamic pressure and $\delta_{ij}$ is the Kronecker delta. If $i = j$ it is equal to 1; otherwise it is equal to zero. This means that only diagonal components of the stress tensor survives and the other components are zero for fluids at rest.

For a moving fluid, the stress tensor is not a diagonal tensor. Shear forces are present due to the motion of the fluid and the non-diagonal elements are different than zero. So, stress tensor can be written as

$$\tau_{ij} = -p\delta_{ij} + \sigma_{ij} \tag{2.4}$$

In this equation, $p$ is still thermodynamic pressure, but there are some differences from the previous equation. Thermodynamic pressure is defined in the equilibrium state and since the fluid is in motion, the system is not in equilibrium. This makes some differences in the definition of pressure. However if the relaxation time of the molecules is small enough compared with the time scale of flow, one can still assume it to be equal to thermodynamic pressure by ignoring some tiny effects.

The $\sigma_{ij}$ in the eq. 2.4 is called the deviatoric stress tensor. As stated in the previous section, the deviatoric stress tensor should be proportional to velocity gradient. To find this dependence on the velocity gradients, firstly we decompose velocity gradient into symmetric and antisymmetric components as

$$\frac{\partial u_i}{\partial x_j} = \frac{1}{2}\left(\frac{\partial u_i}{\partial x_j} + \frac{\partial u_j}{\partial x_i}\right) + \frac{1}{2}\left(\frac{\partial u_i}{\partial x_j} - \frac{\partial u_j}{\partial x_i}\right) \tag{2.5}$$

In this equation, the antisymmetric part (second term from the right side) is related to rotations and cannot contribute to the stress. So the stresses comes from only the symmetric part, called the strain tensor. Then $\sigma_{ij}$ is proportional to the symmetric part of the velocity gradient and we can write

$$\sigma_{ij} = K_{ijmn}\frac{1}{2}\left(\frac{\partial u_m}{\partial x_n} + \frac{\partial u_n}{\partial x_m}\right) \tag{2.6}$$

where $K_{ijmn}$ is a tensor with 81 components. We do not need to calculate all these 81 constants. If we assume the case of an isotropic medium and symmetric stress tensor, only a few of them will survive and using tensor algebra, we can write that

$$\sigma_{ij} = \Big(\mu\delta_{im}\delta_{jn} + \mu\delta_{in}\delta_{jm} + \lambda\delta_{ij}\delta_{mn}\Big)\frac{1}{2}\left(\frac{\partial u_m}{\partial x_n} + \frac{\partial u_n}{\partial x_m}\right) \tag{2.7}$$

The right-most term gives $\lambda\nabla\cdot\vec{u}$ and for incompressible fluids, $\nabla\cdot\vec{u} = 0$. If fluids are compressible, they allow for some phenomena like shock waves. We will not deal with such issues in this work.

After some simple algebra for incompressible fluids, we get

$$\sigma_{ij} = \mu\left(\frac{\partial u_i}{\partial x_j} + \frac{\partial u_j}{\partial x_i}\right). \tag{2.8}$$

Then we obtain the equation for stress

$$\tau_{ij} = -p\delta_{ij} + \mu\left(\frac{\partial u_i}{\partial x_j} + \frac{\partial u_j}{\partial x_i}\right). \tag{2.9}$$

This equation gives the stress for an incompressible fluid and it has two parts: pressure and stresses due to velocity gradients ([Kundu and Cohen, 2002]).

### 2.2.4 Navier-Stokes equation

The Navier-Stokes equation gives the relationship between the acceleration of fluid and effecting forces. By the definition of acceleration, there is a difference in fluid dynamics due to the motion of the fluid. Since the fluid moves and its velocity changes with respect to position, acceleration of the fluid is different than the ordinary definition of classical acceleration $\vec{a} = \partial\vec{u}/\partial t$. If we consider $\vec{u} = \vec{u}(\vec{x}, t)$ and take the total time derivative of velocity, we obtain

$$\frac{D\vec{u}}{Dt} = \frac{\partial\vec{u}}{\partial t} + \vec{u}\cdot\nabla\vec{u} \tag{2.10}$$

This operator $D/Dt$ has different names, such as total time, material, substantial or particle derivative ([Kundu and Cohen, 2002]). The first part of this operator $\partial/\partial t$ corresponds to the local rate of change with respect to time. The second part $\vec{u} \cdot \nabla$ corresponds to advection, which is present because of the motion of fluid. If this motion changes with respect to position, then this advection term plays a role. If this operator is applied in the presence of heat, then the second term is named convection.

Now we must determine the force on an infinitesimal volume of fluid. In the previous section, we obtained the stress on it. We can decompose stress into normal and shear stresses and the relationship between force and stress is

$$\tau_n = \frac{dF_n}{dA} \qquad \tau_s = \frac{dF_s}{dA} \tag{2.11}$$

If we consider the forces in $x_1$ direction, then we can write

$$\begin{aligned} dF_{x_1} &= \left(\tau_{11} + \frac{\partial \tau_{11}}{\partial x_1}\frac{dx_1}{2} - \tau_{11} + \frac{\partial \tau_{11}}{\partial x_1}\frac{dx_1}{2}\right) dx_2 dx_3 \\ &+ \left(\tau_{21} + \frac{\partial \tau_{21}}{\partial x_2}\frac{dx_2}{2} - \tau_{21} + \frac{\partial \tau_{21}}{\partial x_2}\frac{dx_2}{2}\right) dx_1 dx_3 \\ &+ \left(\tau_{31} + \frac{\partial \tau_{31}}{\partial x_3}\frac{dx_3}{2} - \tau_{31} + \frac{\partial \tau_{31}}{\partial x_3}\frac{dx_3}{2}\right) dx_1 dx_2 \\ &= \left(\frac{\partial \tau_{11}}{\partial x_1} + \frac{\partial \tau_{21}}{\partial x_2} + \frac{\partial \tau_{31}}{\partial x_3}\right) dx_1 dx_2 dx_3 \\ &= \frac{\partial \tau_{j1}}{\partial x_j} dx_1 dx_2 dx_3 \end{aligned} \tag{2.12}$$

Using eq. 2.9, we can write the force on an infinitesimal volume of an incompressible fluid as

$$\vec{F} = -\nabla p + \mu \nabla^2 \vec{u} \tag{2.13}$$

Eq. 2.10 corresponds to the acceleration of a fluid according to Newton's second law. We also know the force from eq. 2.13. Then, by using Newton's second law $\vec{F} = m\vec{a}$ for this fluid with mass density $\rho$, we can write an equation concerning change in velocity in the presence of gravity as

$$\rho \frac{\partial \vec{u}}{\partial t} + \rho \vec{u} \cdot \nabla \vec{u} = -\nabla p + \rho \vec{g} + \mu \nabla^2 \vec{u} \tag{2.14}$$

This is the Navier-Stokes equation, which describes how velocity of a incompressible fluid evolves ([Kundu and Cohen, 2002]). We can also write this equation in a similar form by using the definition of kinematic viscosity $\nu = \mu/\rho$

$$\frac{\partial \vec{u}}{\partial t} + \vec{u} \cdot \nabla \vec{u} = -\frac{1}{\rho}\nabla p + \vec{g} + \nu \nabla^2 \vec{u} \tag{2.15}$$

### 2.2.5 Reynolds number

The left hand side of eq. 2.15 corresponds to inertial forces and $\nu\nabla^2\vec{u}$ corresponds to viscous forces. We can use dimensions of these two forces to be able to compare them. The inertial forces are of the order $f_{in} \sim u^2/l$ where $l$ is a typical geometric length scale. The viscous forces are of the order $f_{vis} \sim \nu|\vec{u}|/l_\perp^2$ where $l_\perp$ is a characteristic length scale perpendicular to the streamlines ([Davidson, 2001]). If we consider the length scales equal, then we can define the ratio of these as Reynolds number and it is

$$Re = \frac{ul}{\nu}. \tag{2.16}$$

If $Re$ is small, then the contribution of viscous forces in the Navier-Stokes equation is high. In the contrary case, the viscous forces are small and play a lesser role. If we consider the characteristic length scale of the flows and calculate $Re$, it would be really high. In this case, we can consider the viscous forces unimportant. However, this consideration is inaccurate since most flows have turbulent properties. This is valid even for very small $Re$ cases and relates to the boundary layers.

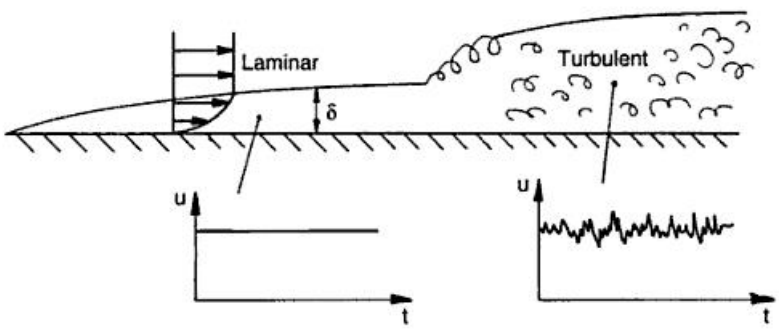


Fig. 2.12: Development of the boundary layer and turbulence on a flat plate for a fluid ([Davidson, 2001]).

Fig. 2.12 depicts the development of the boundary layer. As shown in the figure, at the beginning of fluid flow, the boundary layer is thin. As flow occurs over time, it becomes thicker. At a point, the size of the boundary layer $\delta$ becomes large enough and flow becomes turbulent. This $\delta$ corresponds to the $l_\perp$ characteristic length scale in the calculation of the order of viscous forces. Another length scale in the calculation of $Re$ is the typical geometric length scale $l$. This is the span of the boundary surface. If we consider these two lengths as characteristics lengths in the calculation of $Re$, we obtain a

more convenient way to consider $Re$. In the calculation of eq. 2.16 and the considerations after it, we have taken the lengths as equal and used the geometric length scale. This was the misleading part in the first conclusions about $Re$, where viscosity was considered an ignorable factor. Now it is obvious that viscous forces are always important and their importance is observed when the chosen length scale and span of the boundary layer are suitable sizes.

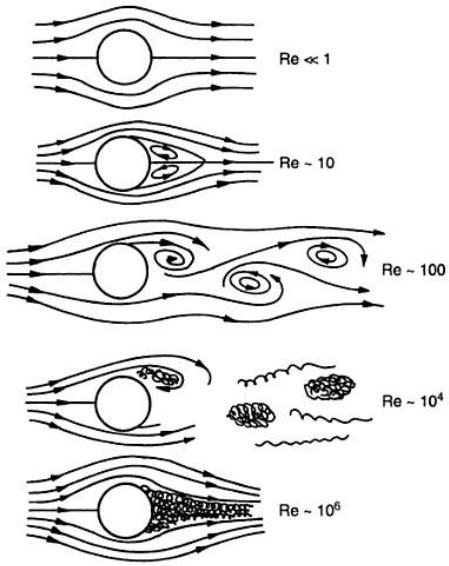


Fig. 2.13: Characteristic flows in the presence of a cylinder with respect to different $Re$ ([Davidson, 2001]).

Fig. 2.13 shows characteristic flows in the presence of a cylinder at different $Re$. In this example, the flow is laminar if $Re < 10^4$. But there are different types of laminar flows. For small $Re$, there is symmetry in the flow. If $Re << 1$, flow resembles inviscid flow. When the order of $Re$ is just above unity, steady vortices appear. The symmetry of flow is lost if $Re > 10$. This is shown in the example where $Re \sim 100$. In this case, periodic vortices known as Karman's vortex street appear. The laminar structure of flow disappears around $10^4$. At this value, there is still a vortex street, but it is not as regular as Karman's. At really high $Re$, $10^6$, this street structure is lost and some small vortices can be observed ([Davidson, 2001]).

### 2.2.6 Vorticity

In eq. 2.5 we mentioned that the antisymmetric part of this equation $\frac{1}{2}\left(\frac{\partial u_i}{\partial x_j} - \frac{\partial u_j}{\partial x_i}\right)$ is related to rotations. Now we will deal with these rotations as well as vorticity. Vorticity is defined as ([Davidson, 2001])

$$\vec{\omega} = \nabla \times \vec{u} \tag{2.17}$$

and its components can be written as ([Kundu and Cohen, 2002])

$$\omega_1 = \frac{\partial u_3}{\partial x_2} - \frac{\partial u_2}{\partial x_3} \qquad \omega_2 = \frac{\partial u_1}{\partial x_3} - \frac{\partial u_3}{\partial x_1} \qquad \omega_3 = \frac{\partial u_2}{\partial x_1} - \frac{\partial u_1}{\partial x_2} \tag{2.18}$$

As it is easily seen these are twice the related antisymmetric components. These antisymmetric components of the stress tensor are the source of shear forces. If $\frac{\partial u_i}{\partial x_j} = \frac{\partial u_j}{\partial x_i}$, there is no rotation and $\vec{\omega} = 0$ ([Kundu and Cohen, 2002]). However if one of these is greater than the other, there will be a rotation.

By dropping the gravitational force in the Navier-stokes equation and using the relationship $\nabla(u^2/2) = (\vec{u} \cdot \nabla)\vec{u} + \vec{u} \times \vec{\omega}$, we can write

$$\frac{\partial \vec{u}}{\partial t} = -\nabla\left(p/\rho + u^2/2\right) + \nu\nabla^2\vec{u} + \vec{u} \times \vec{\omega} \tag{2.19}$$

For steady inviscid fluids $C = \left(p/\rho + u^2/2\right)$ is constant. This is Bernoulli's theorem and $C$ is Bernoulli's function. Here, if we take the curl of this equation, we obtain the vorticity equation as ([Davidson, 2001])

$$\frac{\partial \vec{\omega}}{\partial t} = \nu\nabla^2\vec{\omega} + \nabla \times (\vec{u} \times \vec{\omega}) \tag{2.20}$$

### 2.2.7 Coriolis force

There are additional effects in a rotating reference frame and to see these, we will firstly look at the transformation of a vector between a rotating reference frame and an inertial one. Similar derivations can be found in books and in the reference lists of ([Batchelor, 1967],[Kundu and Cohen, 2002],[Pedlosky, 1979]). Fig. 2.14 shows two coordinate systems: the rotating one $S'$ $(q_1, q_2, q_3)$ has angular velocity $\vec{\Omega}$ with respect to the inertial one $S$ $(x_1, x_2, x_3)$. In the rotating frame, we can write an ordinary vector $\vec{A}$ as

$$\vec{A} = A_1\hat{q}_1 + A_2\hat{q}_2 + A_3\hat{q}_3 \tag{2.21}$$

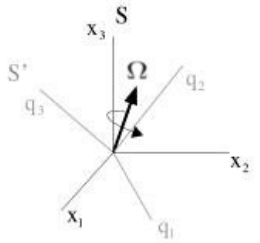


Fig. 2.14: Rotating coordinate system $S'$ is represented with respect to inertial reference frame $S$. ([Dreizler and Ludde, 2010]).

If this vector changes with time, the observers in both reference frames will see this change. However, there will be some differences, which can be understood by writing the time derivative of $\vec{A}$ explicitly

$$\left(\frac{d\vec{A}}{dt}\right)_i = \frac{dA_1}{dt}\hat{q}_1 + \frac{dA_2}{dt}\hat{q}_2 + \frac{dA_3}{dt}\hat{q}_3 + A_1\frac{d\hat{q}_1}{dt} + A_2\frac{d\hat{q}_2}{dt} + A_3\frac{d\hat{q}_3}{dt}. \tag{2.22}$$

The first three terms on the right side of the equation are due to changes in the rotating frame and the last three correspond to changes in the unit vectors due to rotation. The length of the unit vectors is always unity and the only change is in their directions. Now let us consider $\hat{q}_1$ and call the angle between it and $\vec{\Omega}$ as $\psi$. The parallel component of $\hat{q}_1$ to the $\vec{\Omega}$, $|\hat{q}_1|cos\psi$, will not change with rotation. Only $|\hat{q}_1|sin\psi$ will change due to rotation and $\frac{dsin\psi}{dt} = \frac{dsin\psi}{d\theta}\frac{d\theta}{dt}$ where $\theta$ is the angle of rotation and $|\vec{\Omega}| = \frac{d\theta}{dt}$. As the reference frame rotates, only the direction of the $|\hat{q}_1|sin\psi$ will change. Its magnitude will be constant throughout the motion. So we can write $\frac{d\hat{q}_1}{dt} = \vec{\Omega} \times \hat{q}_1$. Then for all components we have

$$\begin{aligned}\left(\frac{d\vec{A}}{dt}\right)_i &= \left(\frac{d\vec{A}}{dt}\right)_r + A_1\vec{\Omega} \times \hat{q}_1 + A_2\vec{\Omega} \times \hat{q}_2 + A_3\vec{\Omega} \times \hat{q}_3 \\ &= \left(\frac{d\vec{A}}{dt}\right)_r + \vec{\Omega} \times \vec{A}.\end{aligned} \tag{2.23}$$

This equation gives the transformation between observed vectors in an inertial and a rotating reference frame for any vector. If the vector $\vec{A}$ is the vector showing the position of an object $\vec{r}$, we have the relation for the velocities as follows

$$\left(\frac{d\vec{r}}{dt}\right)_i = \left(\frac{d\vec{r}}{dt}\right)_r + \vec{\Omega} \times \vec{r} \tag{2.24}$$

and this can also be written as $\vec{u}_i = u_r + \vec{\Omega} \times \vec{r}$. For the accelerations, we have

$$\left(\frac{d\vec{u}_i}{dt}\right)_i = \left(\frac{d\vec{u}_i}{dt}\right)_r + \vec{\Omega} \times \vec{u}_i. \tag{2.25}$$

Using the definition of velocity in eq. 2.25, we obtain

$$\left(\frac{d\vec{u}_i}{dt}\right)_i = \left(\frac{d(\vec{u}_r + \vec{\Omega} \times \vec{r})}{dt}\right)_r + \vec{\Omega} \times (u_r + \vec{\Omega} \times \vec{r}). \tag{2.26}$$

If $\vec{\Omega}$ is constant, we have

$$\vec{a}_i = \vec{a}_r + 2\vec{\Omega} \times u_r + \vec{\Omega} \times \vec{\Omega} \times \vec{r}. \tag{2.27}$$

The extra terms on the right side of the equation are present due to the Coriolis and centripetal forces. Then, for a rotating reference frame, the Navier-Stokes equation becomes

$$\frac{\partial \vec{u}}{\partial t} + \vec{u} \cdot \nabla \vec{u} = -\frac{1}{\rho}\nabla p - 2\vec{\Omega} \times u_r - \vec{\Omega} \times \vec{\Omega} \times \vec{r} + \vec{g} + \nu \nabla^2 \vec{u} \tag{2.28}$$

The centripetal force is mostly unimportant and can be written as $\vec{\Omega}\times\vec{\Omega}\times\vec{r} = -\nabla(\Omega^2 r'^2/2)$ where $r'$ is the distance measured from the axis of rotation. This gradient term can be included in the pressure term and after redefining a new pressure, one can totally omit this term ([Tritton, 1988]).

We can compare the Coriolis force with inertial and viscous forces. There are two non-dimensional numbers for this purpose and they are called the Rossby and Ekman number, respectively. Then the Ekman and Rossby numbers are

$$E = \nu/\Omega l^2 \qquad Ro = U/\Omega l. \tag{2.29}$$

These numbers, $E$ and $Ro$, are special for rotating systems. Since rotating systems are noninertial frames, there are some other forces present and in the above derivation we have obtained them. One of them is the Coriolis force and these numbers compare the strength of the Coriolis force with inertial and viscous forces. For smaller $E$, the effect of viscous forces are weak compared to the Coriolis force and vice versa. For smaller $Ro$, the effect of inertial forces are weak compared to the Coriolis force and vice versa.

## 2.3 Dynamo Theory

In this section, we will start with the origin of cosmological magnetic fields and give an introduction to the dynamo theory. We will also consider electromagnetic relations and derive the induction equation. Then we will give the basics for the dynamo theory and the effect of the heat equation on it. Lastly we will discuss the dynamo mechanism.

### 2.3.1 Origin of cosmological magnetic fields

Previous sections only mentioned the Earth's magnetic field. Earth is not alone in the universe, however, and most cosmological bodies have magnetic fields. Planets, the Sun, stars, some of the moons of the planets and even the galaxies have their own magnetic fields. The origins of these magnetic fields have been debated for a long time and many different theories have been proposed.

Firstly, let us consider the sources of the magnetic fields. There are two possible sources. The first one is the magnetization of matter. This can have different origins, however, the main source of this magnetization is electron spin alignment. The second source for the magnetic field is electric current, which is explained by one of the basic laws of electrodynamics. Due to Faraday's law of induction, electric currents can induce magnetic field.

The first potential source, magnetization, cannot explain the origin of these magnetic fields for several reasons. To be able to produce a strong magnetic field, a material should have the ferromagnetic property. However, in most cases, the temperature of the fluid producing the magnetic field is higher than the Curie temperature. Since ferromagnetic properties cannot exist above this temperature, magnetization cannot be the origin of cosmological magnetic fields. We know that for the Earth and Sun, there are reversals and these reversals take place repeatedly throughout the history of these cosmological bodies. These reversals also cannot be explained by magnetization.

The second possibility, induction of magnetic field from electric current, is likely the source of cosmological magnetic fields. Since the temperature of the Sun is much higher than ionization temperature, all atoms constituting the Sun are in ionized form. So an electrical current is generated due to the thermally and gravitationally driven motion of these charged particles. This current induces magnetic field. A similar phenomenon

occurs at the cores of the Earth, other planets and the moons of these planets. There are some differences between solar and planetary induction of magnetic fields, mostly due to high temperature and the fast motion of the Sun and stars. The induction of a magnetic field due to the motion of electrically conducting fluid is described by dynamo theory. The first self-exited dynamo theory was proposed by von Siemens (1866) ([Krause and Radler, 1980]). However, in 1919, Larmor made a proposal that Earth's magnetic field is generated by dynamo action at the Earth's core due to the motion of the liquid metal in the core. This dynamo action is a complicated procedure and will be described in the following sections. Before, we will overview Maxwell's eqautions and the induction equation.

### 2.3.2 Maxwell's equations

Maxwell's equations and Lorentz force are the main components of electrodynamics. Maxwell's equations describe how electric field $\vec{E}$ and magnetic field $\vec{B}$ changes and Lorentz force describes how these fields affect charged particles. There are four Maxwell equations and each describes different electromagnetic phenomena.

One equation is Gauss's law. It is related to Coulomb's law, which describes electrostatic force. Coulomb's law originated from experimental observations related to the force between two small charged bodies. The force on test particle with charge $q_t$ is $\vec{F} = q_t\vec{E}$ and electric field at $\vec{x}$ due to charge $q$, which is at position $\vec{x}'$ is

$$\vec{E} = kq\frac{\vec{x} - \vec{x}'}{|\vec{x} - \vec{x}'|^3} \tag{2.30}$$

Gauss's law concerns the integration of an electric field over a surface which encloses a volume. It states that integration of the normal component of $\vec{E}$ over an entire surface gives zero if there is no charge inside the enclosed volume and $4\pi q$ if there is a charge $q$. If there is a charge $q$ inside the volume we can write Gauss's law as

$$\oint_S \vec{E} \cdot \vec{n} da = 4\pi q \tag{2.31}$$

where $\vec{n}$ is the unit vector perpendicular to the surface $S$. Using the divergence theorem $\oint_S \vec{A} \cdot \vec{n} da = \int_V \nabla \cdot \vec{A} d^3x$ and $q = \int_V \rho(\vec{x}) d^3x$ where $\rho$ is the charge density, we can also write this law in differential form as

$$\nabla \cdot \vec{E} = \rho/\epsilon_0 \tag{2.32}$$

where $\epsilon_0$ is the permittivity of free space. This is the differential and more commonly used form of Gauss's law ([Jackson, 1962]).

The second and third of the Maxwell's equations are related to magnetism and can be obtained by considering the induction of a magnetic field from current density $\vec{J}(\vec{x})$. The induced magnetic field due to current density is

$$\begin{aligned} \vec{B} &= \int \vec{J}(\vec{x}') \times \frac{\vec{x}-\vec{x}'}{|\vec{x}-\vec{x}'|^3} d^3x' \\ &= \nabla \times \int \frac{\vec{J}(\vec{x}')}{|\vec{x}-\vec{x}'|} d^3x'. \end{aligned} \tag{2.33}$$

This equation directly requires that

$$\nabla \cdot \vec{B} = 0 \tag{2.34}$$

and this is one of the Maxwell's equations. Conceptually, this equation means that there are no magnetic monopoles. The third of the Maxwell's equations can be obtained by taking the curl of eq. 2.33. The result of this curl is

$$\nabla \times \vec{B} = \mu_0 \vec{J} + \nabla \int \frac{\nabla \cdot \vec{J}(\vec{x}')}{|\vec{x}-\vec{x}'|} d^3x'. \tag{2.35}$$

where $\mu_0$ is the permeability of free space. If we consider steady currents $\nabla \cdot \vec{J} = 0$, eq. 2.35 in that limit reduces to Ampere's law. If we consider currents varying with time, using the continuity equation $\nabla \cdot \vec{J} = \frac{\partial \rho}{\partial t}$ and the definition of the electric field, we obtain

$$\nabla \times \vec{B} = \mu_0 \vec{J} + \mu_0 \epsilon_0 \frac{\partial \vec{E}}{\partial t}. \tag{2.36}$$

This equation is Ampere's law with Maxwell's displacement current $\mu_0 \epsilon_0 \frac{\partial \vec{E}}{\partial t}$. The equation describes how the curl of a magnetic field depends on the current density and time variation of the electric field ([Jackson, 1962]).

The last equation is related to the magnetic flux $F$ and electromotive force $\varepsilon$. The electromagnetic force is the integral sum of the electric field over the closed circuit

$$\varepsilon = \oint_C \vec{E} \cdot d\vec{l}. \tag{2.37}$$

This circuit creates a magnetic field around it and the magnetic flux linking it is

$$F = \int_S \vec{B} \cdot \vec{n} da \tag{2.38}$$

where $S$ represents the open surface bounded by $C$ and $\vec{n}$ is the unit normal to this surface. Faraday's experiments and observations concerning magnetic flux and electromotive force gave the formula

$$\varepsilon = -\frac{dF}{dt}. \tag{2.39}$$

This formula shows that time variation in magnetic flux is proportional to the electromotive force. It also reveals that the change in magnetic flux can deduce electromotive force. This is the basic principle for some electronic tools, i.e. electric dynamo, electric motors. Using the Stoke's theorem, eq. 2.39 can be written as

$$\nabla \times \vec{E} = -\frac{\partial \vec{B}}{\partial t} \tag{2.40}$$

and this is the differential form of Faraday's law.

In addition to Maxwell's equations, we need another relationship to get a comprehensive formulation for electromagnetism: the Lorentz force. Lorentz force defines the interaction between charged particles and electromagnetic fields and is given by

$$\vec{f} = q(\vec{E} + \vec{v} \times \vec{B}) \tag{2.41}$$

where $q$ is the charge of the particle and $\vec{v}$ is its velocity.

Maxwell's equations, the continuity equation and Lorenz force are the basic equations for electromagnetism.

### 2.3.3 Induction equation

As stated in the introductory part of this chapter, dynamo theory proposes an explanation for the produced magnetic field of cosmological bodies. Within the framework of dynamo theory, there is a flowing electrically charged fluid and this flow induces magnetic field. Maxwell's equations must be modified for the induction procedure due to some properties of the flowing fluid's structure. One of the basic assumptions of this structure is that it has no net electrical charge. In this assumption, Maxwell's displacement current $\mu_0\epsilon_0\frac{\partial \vec{E}}{\partial t}$ is zero and then we obtain $\vec{J} = \sigma(\vec{E} + \vec{u} \times \vec{B})$. Another effect of this assumption is that $\frac{\partial \rho}{\partial t}$ can be considered zero and the continuity equation becomes $\nabla \cdot \vec{J} = 0$. Then by using $\vec{J} = \sigma(\vec{E} + \vec{u} \times \vec{B})$, $\nabla \times \vec{E} = -\frac{\partial \vec{B}}{\partial t}$, $\nabla \times \vec{B} = -\mu\vec{J}$ and $\nabla \cdot \vec{B} = 0$ we can write ([Davidson, 2001])

$$\frac{\partial \vec{B}}{\partial t} = \nabla \times (\vec{u} \times \vec{B}) + \frac{1}{\mu\sigma}\nabla^2\vec{B} \tag{2.42}$$

where $\sigma$ is electrical conductivity and $\mu$ is the permeability of the conducting medium. This equation is sometimes called the induction equation. In dynamo theory, this equation describes how a magnetic field is induced from the velocity field. The first term on the right-hand side of the equation gives the relationship for the generation of the magnetic field from the velocity field. The second term stands for diffusivity of the magnetic field. We can write the induction equation in a non-dimensional form as

$$\frac{\partial \vec{B}}{\partial t} = \nabla \times (\vec{u} \times \vec{B}) + \frac{E}{Pm} \nabla^2 \vec{B} \tag{2.43}$$

where $Pm = \nu/\eta = \nu\mu\sigma$ is the magnetic Prandtl number and is the ratio of the kinematic viscosity to the magnetic diffusivity. To obtain this non-dimensional form one can use $d$, $\Omega$, $l\Omega$ and $\mu_0 \rho l^2 \Omega^2$ as length, time, velocity and magnetic field scale. Here $\Omega$ is the angular speed and $d$ is the typical length, in general it is the distance between the boundaries.

### 2.3.4 The dynamo theory

The dynamo theory describes the process of magnetic field generation by the inductive action of a conducting fluid. This occurs, in general, via stretching and twisting of magnetic field lines, which converts mechanical energy to magnetic energy ([Davidson, 2001]). This procedure is the known source of the magnetic field for most of the cosmological bodies.

The conversion of mechanical energy to magnetic energy is described by the induction equation, which was introduced in the previous section. This equation gives the source of the magnetic field in fluid motion for fluids, including electrically conducting material. The fluid is usually above the Curie temperature and, at that temperature, metals are in ionized form. Due to this ionization, electrically charged particles move with the fluid. According to this motion, there is a current and this current produces a magnetic field. Both the current and the magnetic field are in the same medium and Lorentz force should affect the fluid. This force must be included in the Navier-Stokes equation, and it becomes

$$\frac{\partial \vec{u}}{\partial t} + (\vec{u} \cdot \vec{\nabla})\vec{u} + 2\vec{\Omega} \times \vec{u} = \nabla\phi + (\nabla \times \vec{B}) \times \vec{B} + E\nabla^2 \vec{u}. \tag{2.44}$$

where $\phi$ corresponds to the pressure and the term due to $\vec{\Omega} \times \vec{\Omega} \times \vec{u}$ since this term corresponds to the total divergence. To obtain this non-dimensional form one can use the scaling used in the non-dimensionalization of the induction equation. This equation and the induction equation form the basis of the dynamo theory. The Navier-Stokes

equation and the induction equation describe how the velocity field and magnetic field evolve, respectively. The velocity field depends on the effects of the Coriolis, pressure, Lorentz and viscous forces. Both the velocity and magnetic field depend on each other. So these two equations are coupled and must be solved simultaneously. This is only possible with computer simulations. In some cases, the Navier-stokes equation can include more terms and then more equations must be considered in these circumstances.

### 2.3.5 Heat equation and its effect on the dynamo

There is a temperature difference between the inner and outer boundary for most of the cases, including Earth and Sun. Due to this difference, heat flows from the high temperature boundary condition to the low temperature boundary condition. This heat flow is defined by the heat equation

$$\frac{\partial T}{\partial t} + \vec{u} \cdot \nabla T = \frac{1}{Pr} \nabla^2 T \tag{2.45}$$

where $T$ represents temperature and $Pr$ is the Prandtl number. $Pr = \nu/\kappa$ is the ratio of momentum diffusivity to thermal diffusivity and $\kappa$ is the thermal diffusivity. Here one can also use abovementioned scaling with temperature scaling $\Delta T$, the temperature difference between the boundaries.

The temperature difference in a fluid changes the density of the fluid and this density change produces another force due to gravitational interactions. In general, the inner boundary has a higher temperature than the outer boundary. Then, the density at the outer boundary is higher than the inner boundary. In the case of spherical geometry, gravitation force pulls the higher density material towards the center. So there must be another term in the Navier-Stokes equation due to this density difference. In the non-dimensional form, we can write the modified Navier-Stokes equation as

$$\frac{\partial \vec{u}}{\partial t} + (\vec{u} \cdot \vec{\nabla})\vec{u} + 2\vec{\Omega} \times \vec{u} = \nabla \phi + (\nabla \times \vec{B}) \times \vec{B} + E\nabla^2 \vec{u} + \frac{ERa}{Pr} \frac{\vec{r}}{r_o} T \tag{2.46}$$

where $\vec{r}$ is the radius vector, $r_o$ is the outer boundary radius and $Ra$ is the Rayleigh number. This non-dimensional equation is also obtained using previously mentioned scalings. The Rayleigh number describes the relationship between buoyancy and viscosity and is defined as $Ra = g\beta\Delta T d^3/\nu\kappa$. In this definition, $g$ stands for gravitation, $\beta$ is the expansion coefficient of the fluid.

The heat equation can also be used to describe the buoyancy variable. If density changes due to some other effects, this density change can also have effects. Then we can add a

source term for buoyancy in eq. 2.45. This time, a modification to the Rayleigh number is needed. So, other effects concerning density changes can also be described by this equation. We will use the buoyancy variable in subsequent sections and due to its usage, we will make modifications to $Ra$ as well.

### 2.3.6 The dynamo mechanism

The dynamo takes place mainly in the fluid part of cosmological bodies. In general, this fluid is highly conducting and can stretch and twist a magnetic field ([Davidson, 2001]). The stretching, twisting and folding of a magnetic flux tube is shown in fig. 2.15. As shown in the figure, the flux tube is first stretched to twice its size. Then, this stretched flux is twisted and finally folded. This is a schematic representation of conversion of mechanical energy to magnetic energy.

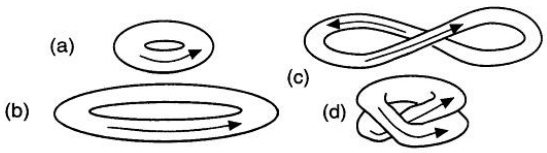


Fig. 2.15: A schematic sketch of the stretching and twisting of a magnetic field. (a) A torus carrying magnetic flux F is stretched to twice its size (b). (c) The twisted version of the stretched magnetic field. (d) The folded version of it. ([Childress and Gilbert, 1995]).

By considering a velocity field that is steady on average, it is possible to obtain dynamo action. For dynamo action, the following properties are needed and these can differ due to the structure of the system. The first necessary key property is a large magnetic Reynolds number $Rm$, which is defined as $Rm = \mu\sigma ul$. At the very least, it should be greater than $5\pi$ ([Davidson, 2001]). Otherwise, the dynamo will lose its magnetic energy due to ohmic losses and the magnetic field will disappear. This can be understood from the induction equation. If we multiply the induction equation by the magnetic field, after some arrangements, we get the energy relation as

$$\frac{\partial}{\partial t}\left(\frac{B^2}{2\mu}\right) = -\nabla \cdot (\vec{E} \times \vec{B}/\mu) - \vec{J} \cdot \vec{E}. \tag{2.47}$$

In this equation, the first term corresponds to the Poynting flux and if we integrate over

all space, it is equal to zero. Then by using $\vec{E} = \vec{J}/\sigma - \vec{u} \times \vec{B}$ we can get

$$\frac{\partial E_B}{\partial t} = \frac{1}{\mu} \int \vec{u} \cdot \left[ \vec{B} \times (\nabla \times \vec{B}) \right] dV - \frac{1}{\sigma} \int J^2 dV \tag{2.48}$$

where $E_B = \int \frac{B^2}{2\mu} dV$ is the magnetic energy and the first term on the right side of the equation corresponds to the rate of the working Lorentz force. The second term is the Joule or Ohmic dissipation. So the work done by the Lorentz force must be greater than the dissipation for a non-decaying dynamo.

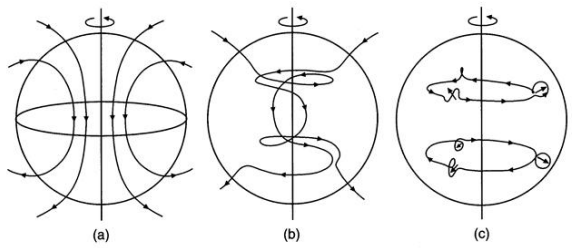


Fig. 2.16: (a) A poloidal magnetic field. (b) The generation of an azimuthal magnetic field from a poloidal magnetic field. (c) The generation of a poloidal magnetic field from an azimuthal one ([Russell, 1999]).

The second key point is that an axisymmetric dynamo is not possible. We can separate the field into an azimuthal and poloidal field, i.e. $\vec{B} = \vec{B}_p + \vec{B}_\theta$. Using the induction equation and this separation, we can show that an axisymmetric velocity field cannot intensify a poloidal magnetic field ([Davidson, 2001]). The poloidal magnetic field generates an azimuthal magnetic field and this azimuthal magnetic field can also generate poloidal magnetic field. The last step cannot be axisymmetric. Thus, an axisymmetric dynamo is not possible. The mechanisms for generation of these fields are $\alpha$ and $\Omega$ effects. The $\alpha$ effect is the generation of a poloidal magnetic field from an azimuthal magnetic field. We can see this procedure from a schematic shown in fig. 2.16. In this figure, a poloidal magnetic field at the beginning is affected by differential rotation. Differential rotation causes a velocity field which rotates faster in the inner boundary and this faster velocity field changes the orientation of the magnetic flux tubes. An azimuthal magnetic field is generated due to this change in orientation. There can also be some eddies or small scale motions in the fluid. The last picture in fig. 2.16 shows these eddies and small scale motions of the fluid. These small scale motions can change the orientation of the magnetic fluxes The small-scale magnetic fields can also arrange themselves to align in the main magnetic field, which is poloidal. This procedure can be shown by dividing the

magnetic field into two components: main magnetic field, which can be considered as the average magnetic field and small scale magnetic field, i.e. $\vec{B} = \vec{B}_0 + \vec{b}$. Here $\vec{B}$ represents the total magnetic field, $\vec{B}_0$ represents the main magnetic field and $\vec{b}$ represents the small scale or fluctuating magnetic field. Then, using the induction equation, we can obtain

$$\partial \vec{B}_0/\partial t = \nabla \times (\vec{u}_0 \times \vec{B}_0) + \alpha \nabla \times \vec{B}_0 + 1/(\mu\sigma)\nabla^2 \vec{B}_0. \tag{2.49}$$

This extra term in the induction equation is the mathematical representation of the $\alpha$ effect. This is one of the generally accepted mechanisms for magnetic field generation in dynamo theory and is known as $\alpha - \Omega$ dynamo ([Davidson, 2001]).

There are also some other dynamo mechanisms. One of them is $\alpha^2$ dynamo. If we do not consider differential rotation, then the generation of the azimuthal magnetic field due to differential rotation is eliminated. In $\alpha^2$ dynamos, we can consider that azimuthal magnetic field can be generated from the poloidal magnetic field via small scale motions. Then, these small scale motions appear and again generate a poloidal magnetic field. This is the basic working principle for the $\alpha^2$ dynamo ([Davidson, 2001]).

## 2.4 Dynamo Experiments

Some laboratory dynamo experiments have been conducted. Here, we will mention three of them: Riga, Karlsruhe and the von Karman sodium experiment. These are the three successful experiments.

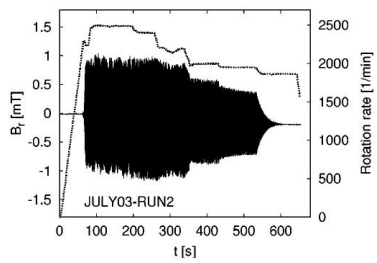


Fig. 2.17: The radial magnetic field and propeller rotation rate of the Riga experiment during one run in July 2003 ([Gailitis et al., 2004]).

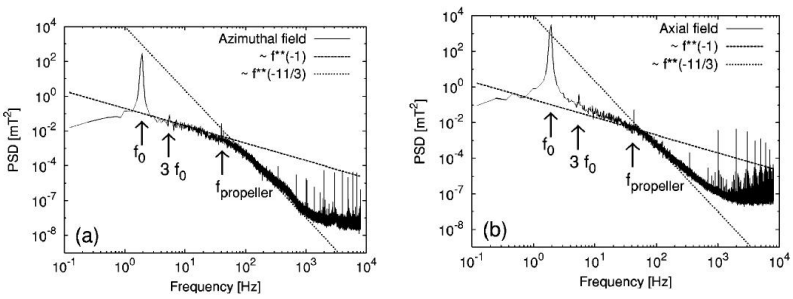


(a) (b)

Fig. 2.18: PSD of (a) azimuthal and (b) axial magnetic fields for the Riga experiment for the run in June 2003 ([Gailitis et al., 2004]).

The Riga experiment has been carried out with two electric motor propellers. The setup consists of three concentric cylinders for different flow structures. The flowing fluid is sodium with a total volume $2m^3$. The central flow has azimuthal and axial velocity components and these flow components are the main factors generating the magnetic field. There are published results for this experiment ([Gailitis et al., 2004], [Gailitis et al., 2003], [Gailitis et al., 2001]). Fig. 2.17 shows the results of one experimental run in the Riga experiment. In this graph, the radial magnetic field and the rotation rate of the propeller are shown. The PSDs of this run for the axial and azimuthal magnetic fields are shown in 2.18. Both have nearly $1/f$ frequency dependence in the low frequency range. In the high frequency range, the frequency dependence

changes to $1/f^{11/3}$.

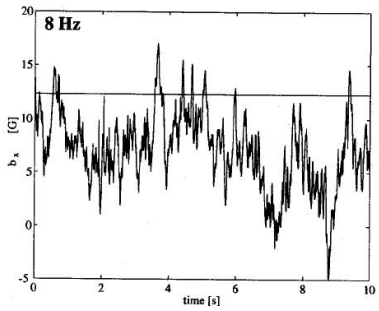


Fig. 2.19: The x-component magnetic field from the von Karman sodium experiment ([Bourgoin et al., 2002]).

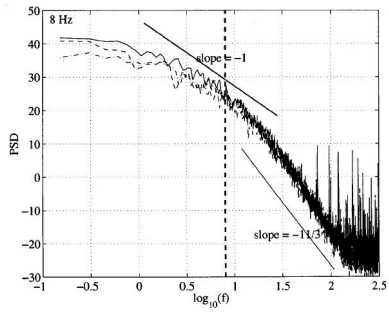


Fig. 2.20: The PSD of the x-component magnetic field from the von Karman sodium experiment ([Bourgoin et al., 2002]).

The second experiment that we will mention is the von Karman sodium experiment. There is a cylindrical vessel with diameter $40cm$ for this experiment. Two coaxial impellers generate the flow. One can find published researches on this experiment ([Monchaux et al., 2009], [Volk et al., 2006], [Bourgoin et al., 2006]). We will consider the experiment result shown in fig. 2.19. In this figure, only one of the magnetic field measurements is considered: the measurement close to the $8Hz$ propeller. The other propeller runs at $17Hz$ and produces similar results. As seen in fig. 2.19, the x-component of the magnetic field is fluctuating.

Fig. 2.20 shows the PSD of the magnetic field shown in fig. 2.19. Again, there is $1/f$ frequency dependence in the low frequency range and $1/f^{11/3}$ dependence in the high frequency range. This frequency dependence is similar to the previously shown Riga experiment results.

The third experiment is the Karlsruhe experiment. In this experimental setup, there are

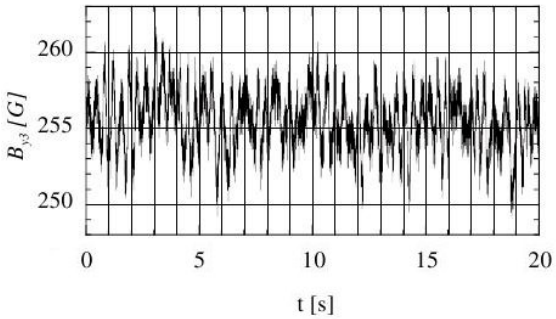


Fig. 2.21: The $B_{y3}$ component of the magnetic field taken from the result of the Karlsruhe experiment ([Muller et al., 2002]).

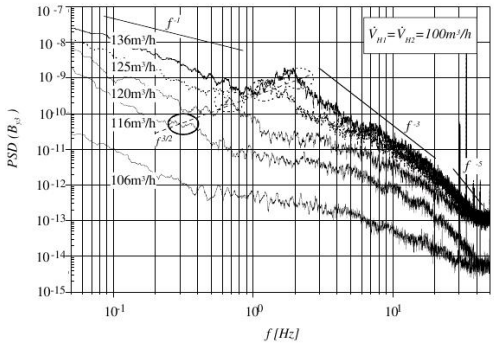


Fig. 2.22: The PSD of the $B_{y3}$ component of the magnetic field measured at different sensors [Muller et al., 2002].

52 cylindrical vortex generators which are connected to three different loops. Different sensors measure magnetic fields at different positions. Detailed information concerning this experiment and its specially designed configuration can be found in different papers ([Muller et al., 2002], [Stieglitz and Muller, 2001]). In fig. 2.21, the $B_{y3}$ component of the magnetic field from the cited paper is shown in that work. The $B_{y3}$ component shows some fluctuations and the PSD of a similar time series measured at different flow rates are shown in fig. 2.22. The flow rates are $136m^3/h$, $125m^3/h$, $120m^3/h$, $116m^3/h$ and $106m^3/h$. Five different PSDs result from these different flow rates because as flow rate changes, properties of PSD change. For the fastest flow rate, 4 different power laws show the frequency dependence of the PSD. These are $1/f$, $f^{3/2}$, $1/f^3$ and $1/f^5$. As frequency increases, these power laws follow one another for the flow rate $136m^3/h$. These power laws are not valid for other flow rates. However, $1/f$ is a general power law for all flows.

We have seen that different power laws describe frequency dependence in these dynamo experiments. However, in general, $1/f$ power law for the low frequency regime is valid for all three experiments. These experiments are vastly different from the Earth's dynamo, where heat conditions, shapes, fluid type and many other factors are all different. However, the dynamo experiments all have one thing in common: the success of a dynamo experiment relies on the generation of a magnetic field that does not decay.

# 3 Numerical Dynamo Simulations

There are several classifications of the dynamo mechanism. In one classification, we use the $\alpha-\Omega$ and $\alpha^2$ dynamos as generation mechanisms of the magnetic field. The $\alpha-\Omega$ dynamo is the most widely accepted and is used in research. The $\alpha^2$ dynamo is another type of magnetic field generation and both were introduced in Section 2.4.6. There are many studies on $\alpha^2$ type of generation ([Soward and Jones, 2005], [Barenghi and Jones, 1991], [Barenghi, 1992], [Hollerbach and Ierley, 1991]).

Another classification arises due to the driving force of fluid motion. This classification includes convection driven dynamo, gravitational dynamo and precession driven dynamo. The most popular and accepted one is convection driven dynamo and there is a lot of published research on this mechanism ([Kutzner and Christensen, 2002], [Soward, 1974]), [Jones and Roberts, 2000], [Childress and Soward, 1972], [Christensen and Aubert, 2006], [Olson and Christensen, 2006], [Busse et al., 1998], [Jones, 2000], [Soward, 1974]). In the convection driven dynamo, there is a temperature difference between the boundaries. This temperature difference causes density differences and gravitation pulls the higher density part and convection takes place. This is the main idea behind the convection driven dynamo. The second one, gravitational dynamo, is not as popular as convection driven dynamo, but there is a similarity between them. Both employ the heat equation. It is used as the heat transfer equation in convection driven dynamo and as the buoyancy transport equation in gravitational dynamo. Similar to the convection driven dynamo, convection and gravitation are also at play in the gravitational dynamo. The difference between these two dynamo types is related to the source of the density difference. It is observed due to the solidification of higher density material in the inner boundary. The name "gravitational dynamo" was given by another author and we have followed him. It is also said compositional convection dynamo for this mentioned type. There is also an abundance of published research on gravitational dynamo ([Olson, 2007], [Lister and Buffett, 1995], [Loper, 2007]). Lastly, precession driven dynamo is different compared to the first two because the driving force in the dynamo is precession. The

heat equation effect is ignored in this consideration and a force due to the precession is included. This was first carried out by Tilgner and further research has explored this mechanism ([Tilgner, 2005], [Wu and Roberts, 2008], [Zhang et al., 2010]).

A third classification type of the dynamo mechanism is referred to as kinematic dynamo. In this classification, the Lorentz force in the Navier-stokes equation is removed and only kinematic forces effects on the motion of the fluid are considered. There is also published research on this topic ([Tilgner, 1997], [Pekeris et al., 1973], [Roberts, 1972]).

Here, we will only model gravitationally driven and convection driven dynamos. The abovementioned stretching and twisting take place due to the forces in the Navier-Stokes equation. Stretching and twisting are essential for the generation of the magnetic field, but we do not need to consider these separately because their calculations are carried out numerically within our models.

## 3.1 Gravitational dynamos

To investigate the gravitational numerical geodynamo, the following dimensionless equations are simultaneously solved: the Navier-Stokes equation, buoyancy transport equation, magnetic induction equation and continuity equations for mass and magnetic field.

$$\begin{aligned}
\frac{\partial \vec{u}}{\partial t} + (\vec{u}\cdot\vec{\nabla})\vec{u} + 2\hat{z}\times\vec{u} &= \nabla\phi - \frac{E^2 Ra}{Pr} T \frac{\vec{r}}{r_0} + (\nabla\times\vec{B})\times\vec{B} + E\nabla^2\vec{u} \\
\frac{\partial T}{\partial t} + (\vec{u}\cdot\vec{\nabla})T &= \frac{E}{Pr}\nabla^2 T - E\epsilon \\
\frac{\partial \vec{B}}{\partial t} + \nabla\times(\vec{B}\times\vec{u}) &= \frac{E}{Pm}\nabla^2\vec{B} \\
\vec{\nabla}\cdot\vec{u} = 0 \qquad & \qquad \vec{\nabla}\cdot\vec{B} = 0
\end{aligned}$$

where $B$, $u$, $\phi$, $T$ and $\epsilon$ are the magnetic field, fluid velocity, pressure perturbation, buoyancy variable and buoyancy source, respectively. $E$, $Pr$, $Pm$ and $Ra$ are the Ekman, Prandtl, magnetic Prandtl and Rayleigh numbers, respectively. In the numerical solutions, the ratio of inner to outer radii $d = r_i/r_o$ is fixed at 0.35; the dimensionless outer radius $r_0 = 1/0.65$; and the variable modeling the buoyancy source ([Olson, 2007]) $\epsilon$ is fixed at 1. This buoyancy source is inserted in these equations to represent the solidification in the inner boundary. Nondimensionalization is achieved by using the radius ratio $d$ as the length scale and the inverse of angular speed $1/\Omega$ as the time scale. The fluid velocity is scaled by $d\Omega$ and the magnetic field is scaled by $(\mu_0\rho_0 d^2\Omega^2)^{1/2}$ where

$\rho_0$ is the outer core mean density. The buoyancy variable $T$ is scaled by $\frac{\dot{T}_0 d^2}{\nu}$ where $\dot{T}_0$ is the time derivative of the spatially uniform slowly increasing part of the light element concentration in the outer core. We consider the same physical model described in ([Olson, 2007]). It is a model for a rotating spherical shell with its gap filled with fluid and its motion driven by gravitational convection. Here, we change the boundary conditions and add a buoyancy source term. To better fit gravitational or compositional convection, we employ the following boundary conditions: fixed buoyancy variable at the inner boundary $T = 1$ at $r = r_i$ and zero flux through the outer boundary $\partial T/\partial t = 0$ at $r = r_o$. Both velocity boundary conditions are taken as no slip and magnetic boundary conditions are considered to be electrically insulating.

Here, we will again define the dimensionless numbers, since there are changes in some of the definitions. The Ekman number, the ratio of viscous forces to Coriolis forces, is defined as $E = \frac{\nu}{d^2\Omega}$ where $\nu$ is the kinematic viscosity. The Prandtl number, the ratio of kinematic viscosity to thermal diffusivity, is defined as $Pr = \frac{\nu}{\kappa}$ where $\kappa$ is the diffusivity of the buoyancy variable. The magnetic Prandtl number, the ratio of kinematic viscosity to magnetic diffusivity, is defined as $Pm = \frac{\nu}{\eta}$ where $\eta = 1/\mu_0\sigma$ is the magnetic diffusivity and $\sigma$ is the electrical conductivity. The Rayleigh number, the ratio of buoyancy forces to the product of thermal and momentum diffusivities, is defined as $Ra = \frac{\alpha g_0 d^5 \dot{T}_0}{\nu^2 \kappa}$ where $\alpha = (\rho_0 - \rho_{Le})/\rho_0$, $\rho_{Le}$ is the light element end member mixture and the subscript $Le$ represents light element concentration and $g_0$ is the gravity at the core-mantel boundary. This last parameter $Ra$ controls the strength of the buoyancy forces, which drives the convection. In gravitational dynamos cooling of the core and solidification of iron and nickel result in an increase in the partition of the light elements in the liquid near the inner core boundary. As the light elements concentration increases, the density of the liquid at the inner core boundary decreases, which enhances the buoyancy forces ([Olson, 2007]).

To be able to comment on the time scale of this dynamo model within the geomagnetic time scale, we can use the dipole free decay time. The dimensionless dipole free decay time is

$$t_d = \frac{Pm}{E}\left(\frac{r_0}{\pi d}\right)^2. \tag{3.1}$$

The dipole decay time corresponds to approximately 20 kyr for Earth ([Olson, 2007]).

The equations were solved using the spectral method described in Tilgner's work with a resolution of 33 Chebychev polynomials in radius and spherical harmonics of degree up to 128 ([Tilgner, 1999]). From these solutions, we get different outputs, but we will mostly

use: the axial component of dipole moment, kinetic and magnetic energies and radial component of the velocity and magnetic field. The kinetic and magnetic energies were calculated through the formulas $E_{kin} = \frac{1}{2}\int \vec{u}^2 d^3x$ and $E_{mag} = \frac{1}{2}\int \vec{B}^2 d^3x$, respectively. From these energies, we extracted the root mean square values of the velocity field and magnetic field $u_{rms}$ and $B_{rms}$. Then we calculated the PSD of these rms values and obtained power laws. We also showed the radial component of the velocity field at $r = (r_i + r_o)/2$ and in the equatorial plane and the magnetic field on the outer boundary and in the equatorial plane. Some of the results of this section were previously published ([Tanriverdi and Tilgner, 2011]). Following the numerical solution of the equations, we will comment on the results.

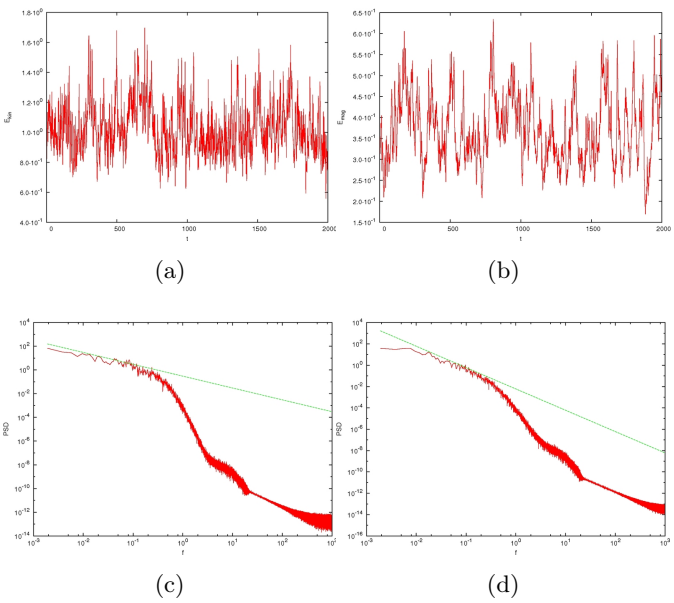


Fig. 3.1: Numerical results of the reversing gravitational dynamo at $Ra = 1 \cdot 10^6$, $Pm = 20$, $E = 6.5 \cdot 10^{-5}$ and $Pr = 1$. a) Time series of the kinetic energy. b) Time series of the magnetic energy. c) PSD of $u_{rms}$. d) PSD of $B_{rms}$.

Fig.3.1, fig.3.2 and fig.3.3 show the results and the analysis of the simulation for $Ra = 1 \cdot 10^6, Pm = 20, E = 6.5 \cdot 10^{-5}, Pr = 1$. Fig.3.1 shows the time series of the magnetic and kinetic energy and PSDs of $u_{rms}$ and $B_{rms}$. We see that the power spectrum of the rms velocity field has $1/f$ dependence for low frequencies and the power spectrum of the rms magnetic field decreases as $1/f^2$ for the same frequency interval. For the high frequency spectrum, there are different power laws and these are detailed in tab. 3.1.

Another output of this solution is depicted in fig.3.2 which shows the axial component

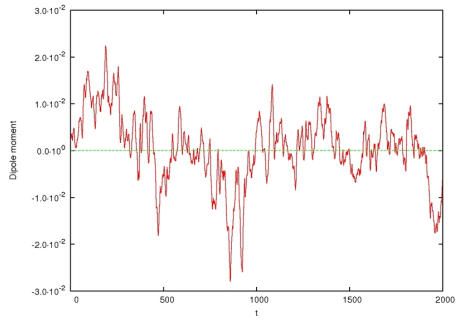


Fig. 3.2: Time series of the dipole moment at $Ra = 1 \cdot 10^6$, $Pm = 20$, $E = 6.5 \cdot 10^{-5}$ and $Pr = 1$.

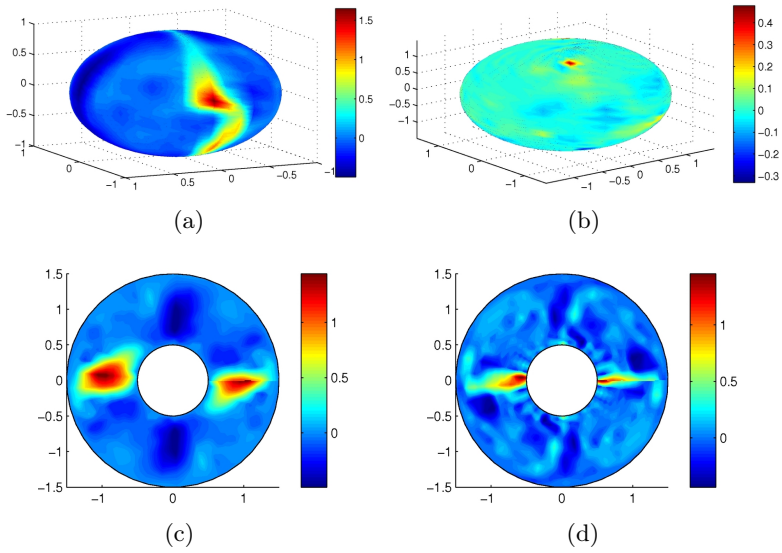


Fig. 3.3: Structure of the reversing gravitational dynamo at $Ra = 1 \cdot 10^6$, $Pm = 20$, $E = 6.5 \cdot 10^{-5}$ and $Pr = 1$. a) Radial component of the velocity field $u_r$ at $r = (r_i + r_o)/2$. b) Radial component of the magnetic field $B_r$ on the core mantle boundary. c) Radial component of the velocity field $u_r$ in the equatorial plane. d) Radial component of the magnetic field $B_r$ in the equatorial plane.

of the dipole moment versus time. It has positive values at some time intervals, and negative values at others. This pattern is repeated many times over the simulation time and means that there are many magnetic reversals for this solution. To compare these reversals, we can use the decay time formula given by eq.3.1. The dipole decay time for this solution is $t_d = 702$. If we use the value for the estimated decay time for Earth in this simulation, the whole simulation time corresponds to 57kyr. Earth's dipole decay time is approximately 20kyr. On the other hand, we observe many reversals in the simulation.

This shows that the decay does not takes place and the velocity field generates enough magnetic field.

Fig.3.3 shows the radial components of the velocity field at $r = (r_i + r_o)/2$ and in the equatorial plane and the magnetic field on the core mantle boundary and in the equatorial plane. In the equatorial plane, we see two cyclonic and two anticyclonic vortices in the velocity field. The velocity field at $r = (r_i + r_o)/2$ also shows these vortices. The magnetic field on the core mantle boundary shows a structure similar to a dipole field. In the equatorial plane, we see cross sections of two magnetic flux tubes. However, the structure of these flux tubes is not as smooth as those observed in the velocity field. This should be related to the magnetic Prandtl number. Since it is bigger than 1 in our simulations, magnetic diffusivity takes place slowly and the structures of these flux tubes are not as smooth as vortices in the velocity field. To be able to compare the simulation to Earth's magnetic field, we should consider the magnetic field over the mantle. If we consider the magnetic field over the mantle, the magnetic field will be smoother and, similar to the Earth's magnetic field, its structure will look more like a dipole field.

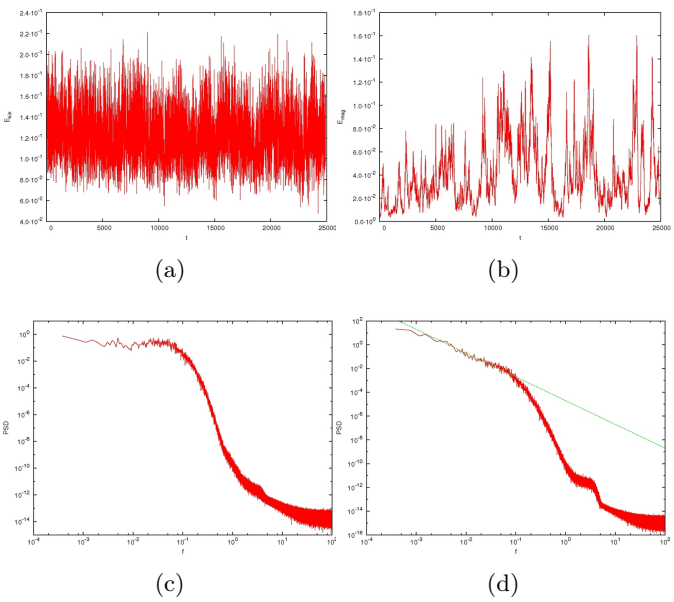


Fig. 3.4: Numerical results of the reversing gravitational dynamo at $Ra = 1 \cdot 10^5$, $Pm = 20$, $E = 6.5 \cdot 10^{-5}$ and $Pr = 1$. a) Time series of the kinetic energy. b) Time series of the magnetic energy. c) PSD of $u_{rms}$. d) PSD of $B_{rms}$.

Fig.3.4, fig.3.5 and fig.3.6 show the results and the analysis of the simulation for $Ra = 1 \cdot 10^5, Pm = 20, E = 6.5 \cdot 10^{-5}, Pr = 1$. Fig.3.4 shows the time series of the magnetic and

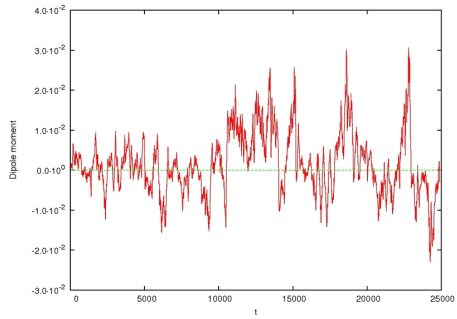


Fig. 3.5: Time series of the dipole moment at $Ra = 1 \cdot 10^5$, $Pm = 20$, $E = 6.5 \cdot 10^{-5}$ and $Pr = 1$.

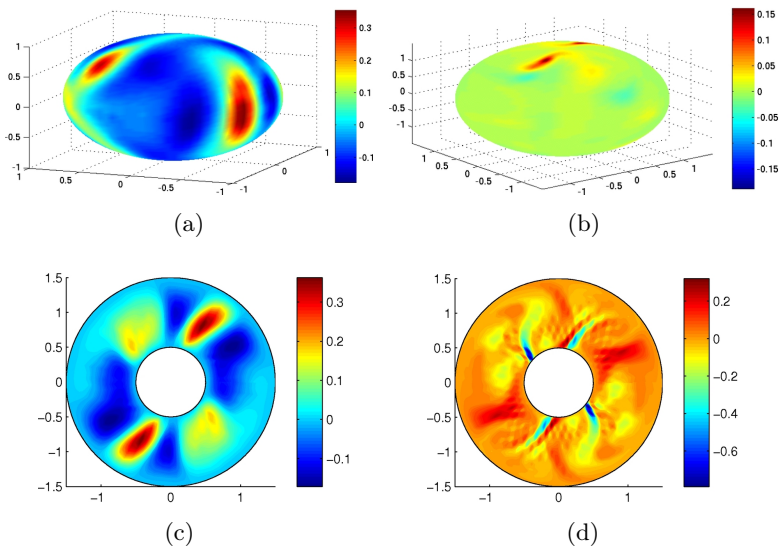


Fig. 3.6: Structure of the reversing gravitational dynamo at $Ra = 1 \cdot 10^5$, $Pm = 20$, $E = 6.5 \cdot 10^{-5}$ and $Pr = 1$. a) Radial component of the velocity field $u_r$ at $r = (r_i + r_o)/2$. b) Radial component of the magnetic field $B_r$ on the core mantle boundary. c) Radial component of the velocity field $u_r$ in the equatorial plane. d) Radial component of the magnetic field $B_r$ in the equatorial plane.

kinetic energy and PSDs of $u_{rms}$ and $B_{rms}$. We see that the PSD of $u_{rms}$ is constant for low frequencies and the PSD of $B_{rms}$ reduces with $1/f^2$ for the same frequency interval. The most interesting difference between fig.3.1 and fig.3.4 is that the power law for the PSD of $u_{rms}$ has changed from $1/f$ to constant for low frequencies. There are different power laws for the high frequency spectrum and these are detailed in tab. 3.1.

Another output of this solution is the axial component of the dipole moment, which is

shown in fig.3.5. Similar to the previous solution, there are many magnetic reversals for this solution. The dipole decay time is again $t_d = 702$ and this time, the whole simulation time corresponds to 712kyr. There are more than 30 reversals in the simulation. Again, the velocity field generates enough magnetic field and the dissipation due to the Joule dissipation does not takes place.

Fig.3.6 shows the radial components of the velocity field at $r = (r_i + r_o)/2$ and in the equatorial plane and the magnetic field on the core mantle boundary and in the equatorial plane. The number of vortices are doubled in the velocity field if compared to the previous case. We see four cyclonic and four anticyclonic vortices in the equatorial plane. In the velocity field, this structure with four paired vortices is also seen at $r = (r_i + r_o)/2$. The magnetic field on the core mantle boundary again shows a structure similar to the dipole field and will be smoothed if we consider the field over the mantle. The magnetic field shows two paired flux tubes in the equatorial plane. However these are not as smooth as in the velocity field.

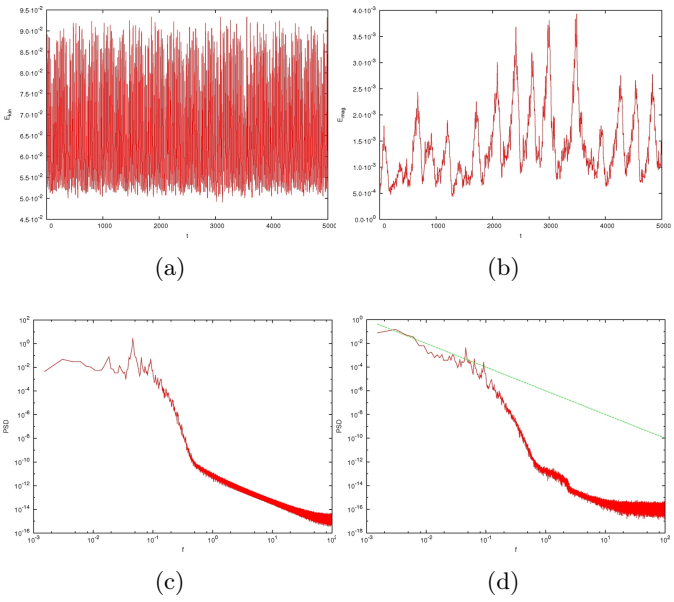


Fig. 3.7: Numerical results of the nonreversing gravitational dynamo at $Ra = 5 \cdot 10^4$, $Pm = 20$, $E = 6.5 \cdot 10^{-5}$ and $Pr = 1$. a) Time series of the kinetic energy. b) Time series of the magnetic energy. c) PSD of $u_{rms}$. d) PSD of $B_{rms}$.

Fig.3.7, fig.3.8 and fig.3.9 show the results and the analysis of the simulation for $Ra = 5 \cdot 10^4, Pm = 20, E = 6.5 \cdot 10^{-5}, Pr = 1$. Fig.3.7 shows the time series of magnetic and kinetic energy and PSDs of $u_{rms}$ and $B_{rms}$. There is a repeated structure in both

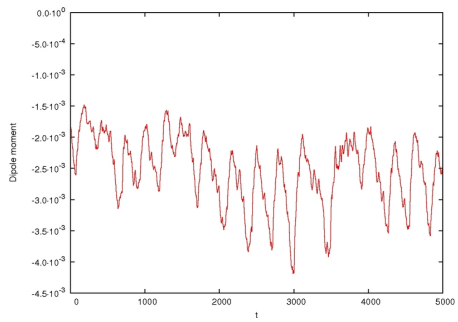


Fig. 3.8: Time series of the dipole moment at $Ra = 5 \cdot 10^4, Pm = 20, E = 6.5 \cdot 10^{-5}$ and $Pr = 1$.

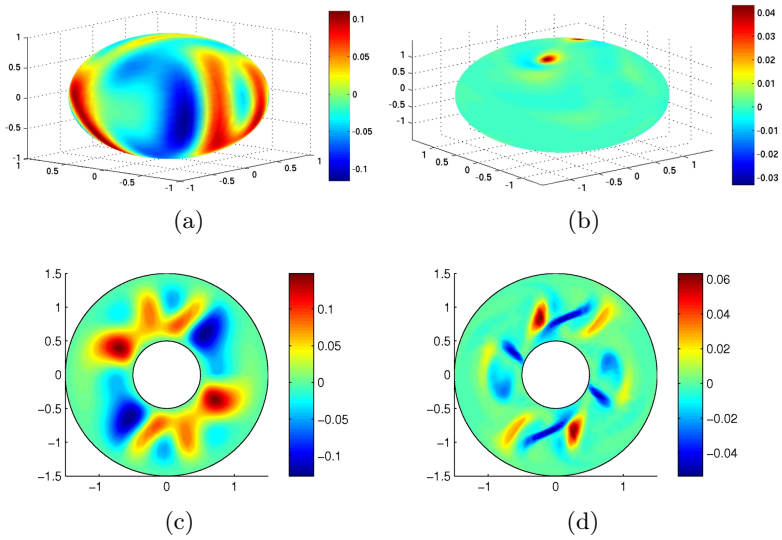


Fig. 3.9: Structure of the nonreversing gravitational dynamo at $Ra = 5 \cdot 10^4$, $Pm = 20$, $E = 6.5 \cdot 10^{-5}$ and $Pr = 1$. a) Radial component of the velocity field $u_r$ at $r = (r_i + r_o)/2$. b) Radial component of the magnetic field $B_r$ on the core mantle boundary. c) Radial component of the velocity field $u_r$ in the equatorial plane. d) Radial component of the magnetic field $B_r$ in the equatorial plane.

kinetic and magnetic energies, which shows itself as peaks in the spectra. Other than these peaks, the PSD of $u_{rms}$ is more or less constant for the low frequency interval and the PSD of $B_{rms}$ decreases as $1/f^2$ for the same frequency interval. Different power laws governing the high frequency intervals are presented in tab. 3.1 in detail.

The axial component of the dipole moment is shown in fig.3.8. In contrast to the previous solutions, there are no magnetic reversals for this solution and the axial component of the dipole moment is always a negative value. The decrease in the Rayleigh number results

with a nonreversing result. The dipole decay time is again $t_d = 702$ and this time, the whole simulation time corresponds to 142kyr.

Fig.3.9 shows the radial components of the magnetic field on the core mantle boundary and in the equatorial plane and the velocity field at $r = (r_i + r_o)/2$ and in the equatorial plane. In the velocity field, there are six cyclonic and six anticyclonic vortices, which are easily observed in the equatorial plane. At $r = (r_i + r_o)/2$, we also see this columnar structure in the velocity field. The magnetic field on the core mantle boundary again shows a structure similar to the dipole field and will be much smoother if we consider the field over the mantle. The magnetic field also shows paired flux tubes in the equatorial plane. However, these have a different structure than the velocity field vortices. Again this difference is related with $Pm$.

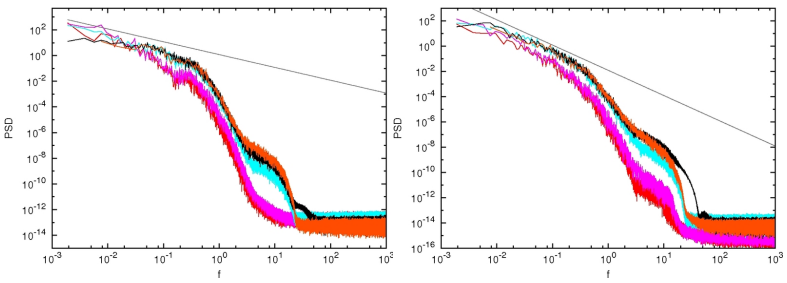


(a) (b)

Fig. 3.10: Numerical results of the reversing gravitational dynamo at $Ra = 1 \cdot 10^6$, $Pm = 5.75, 6, 13, 20, 25, 35$, $E = 6.5 \cdot 10^{-5}$ and $Pr = 1$. a) PSD of $u_{rms}$. b) PSD of $B_{rms}$.

Fig.3.10 shows a set of PSD graphs of $u_{rms}$ and $B_{rms}$ at $Ra = 1 \cdot 10^6$, $E = 6.5 \cdot 10^{-5}$, $Pr = 1$ and $Pm = 5.75, 6, 13, 20, 25, 35$. The PSDs of $u_{rms}$ show $1/f$ dependence on $f$ for low frequencies and the PSDs of $B_{rms}$ decrease as $1/f^2$ for the same frequency interval. It is obvious that the low frequency power law does not depend on $Pm$.

Fig.3.11 shows a set of PSD graphs of $u_{rms}$ and $B_{rms}$ at $Ra = 1 \cdot 10^5$, $E = 6.5 \cdot 10^{-5}$, $Pr = 1$ and $Pm = 20, 30, 35, 50, 70, 100$. The PSDs of $u_{rms}$ are more or less constant for low frequencies and the PSDs of $B_{rms}$ decrease as $1/f^2$ for the same frequency interval. Again, there is no $Pm$ dependence of the low frequency power law.

Fig.3.12 shows a set of PSD graphs of $u_{rms}$ and $B_{rms}$ at $Ra = 5{\cdot}10^4$, $E = 6.5{\cdot}10^{-5}$, $Pr = 1$ and $Pm = 7, 8, 10, 12, 15, 20, 30$. The PSDs of $u_{rms}$ are more or less constant for low

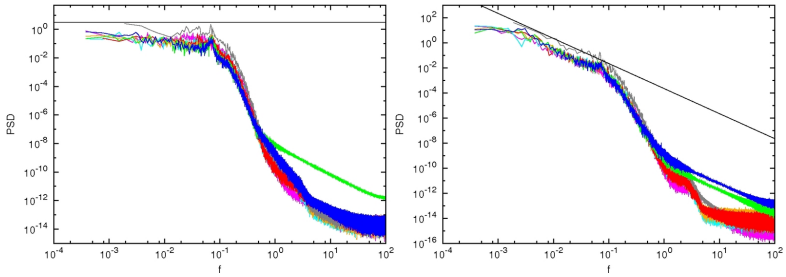


(a) (b)

Fig. 3.11: Numerical results of the reversing gravitational dynamo at $Ra = 1 \cdot 10^5$, $Pm = 20, 30, 35, 50, 70, 100$, $E = 6.5 \cdot 10^{-5}$ and $Pr = 1$. a) PSD of $u_{rms}$. b) PSD of $B_{rms}$.

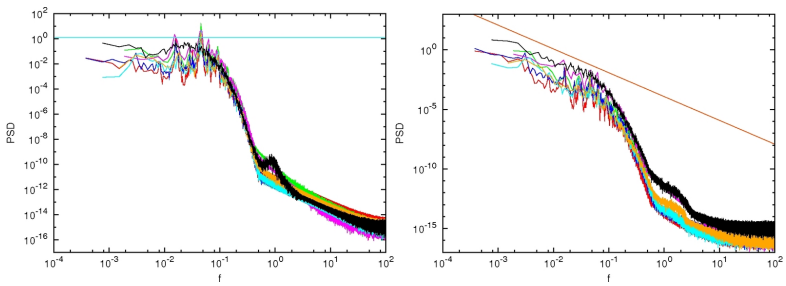


(a) (b)

Fig. 3.12: Numerical results of the nonreversing gravitational dynamo at $Ra = 5 \cdot 10^4$, $Pm = 7, 8, 10, 12, 15, 20, 30$, $E = 6.5 \cdot 10^{-5}$ and $Pr = 1$. a) PSD of $u_{rms}$. b) PSD of $B_{rms}$.

frequencies and the PSDs of $B_{rms}$ decrease as $1/f^2$ for the same frequency interval. Similar to the previous cases, the low frequency power law does not depend on $Pm$.

Table Tab.3.1 provides detailed information on the simulation results shown in fig.3.10, fig.3.11 and fig.3.12. Nearly in all cases for low frequencies, the power law for $B_{rms}$ is -2 and in the corresponding frequency interval, the power law for $u_{rms}$ changes with $Ra$. If $Ra = 1 \cdot 10^6$, the power law is -1 and if $Ra = 1 \cdot 10^5$ or $Ra = 5 \cdot 10^4$ , the power law is 0. Later in this work, we will explain this situation with a simple model. In the high frequency range, the situation is different. The relationship between the power laws for high frequencies can be stated as the power law of $u_{rms}$ at high frequencies is less than the power law of $B_{rms}$ by a approximate value 2 in the same interval. But this is not valid in all cases, which makes it harder to obtain a general relationship. Table 3.1 also shows

| $Ra$ | $Pm$ | $\Lambda$ | $Re$ | $Rm$ | $Ro$ | L$f$ PL ($B_{rms}$) | H$f$ PL ($B_{rms}$) | L$f$ PL ($u_{rms}$) | H$f$ PL ($u_{rms}$) |
|---|---|---|---|---|---|---|---|---|---|
| $1 \cdot 10^6$ | 5.75 | 2.02 | 77.8 | 226 | 0.505 | -2 | -9 | -1 | -10 |
| | 6 | 2.74 | 82.4 | 264 | 0.535 | -2 | -8 | -1 | -10 |
| | 13 | 73 | 65.5 | 362 | 0.426 | -2 | -7 | -1 | -9 |
| | 20 | 171 | 59.9 | 467 | 0.389 | -2 | -6 | -1 | -8.5 |
| | 25 | 243 | 57.5 | 538 | 0.374 | -2 | -6 | -1 | -8.5 |
| | 35 | 408 | 55.6 | 703 | 0.361 | -1.6 | -5.5 | -1 | -8 |
| $1 \cdot 10^5$ | 20 | 16.2 | 20.3 | 53.7 | 0.132 | -2 | -9 | 0 | -12 |
| | 30 | 51 | 20.5 | 82.3 | 0.134 | -2 | -9 | 0 | -12 |
| | 35 | 68.9 | 20.5 | 95.5 | 0.133 | -2 | -9 | 0 | -11 |
| | 50 | 130 | 20.3 | 134 | 0.132 | -2 | -9 | 0 | -11 |
| | 70 | 231 | 19.9 | 181 | 0.130 | -2 | -8 | 0 | -10 |
| | 100 | 386 | 19.6 | 249 | 0.127 | -2 | -7 | 0 | -11 |
| $5 \cdot 10^4$ | 7 | 0.313 | 14.9 | 10.1 | 0.0969 | -2 | -11 | 0 | -13 |
| | 8 | 0.408 | 14.9 | 11.7 | 0.0973 | -2 | -11 | 0 | -13 |
| | 10 | 0.508 | 14.9 | 14.5 | 0.097 | -2 | -11 | 0 | -13 |
| | 12 | 0.778 | 14.8 | 17.2 | 0.0964 | -2 | -11 | 0 | -13 |
| | 15 | 0.455 | 15 | 22 | 0.0977 | -2 | -11.5 | 0 | -15 |
| | 20 | 0.614 | 15 | 29.3 | 0.0976 | -2 | -7.5 | 0 | -15 |
| | 30 | 16.8 | 13.1 | 33.5 | 0.0851 | -2 | -9 | 0 | -14 |

Tab. 3.1: *Gravitational dynamo simulation results. The first two column show control parameters Ra and Pm. Since two of the parameters are constant for these results, they are not shown and* $E = 6.5 \cdot 10^{-3}$ *and* $Pr = 1$. *The next four columns show output parameters* $\Lambda$, *Re, Rm and Ro. The 7th and 8th columns show low frequency interval power law (Lf PL) and high frequency interval power law (Hf PL) for the spectrum of* $B_{rms}$, *respectively. The 9th and 10th columns show similar power laws for the spectrum of* $u_{rms}$.

the Reynolds number $Re = Ro/E$, Elsasser number $\Lambda = B_{rms}^2 Pm/E$, magnetic Reynolds number $Rm = u_{rms}^2 Pm/E$ and Rosby number $Ro = u_{rms}$. It is seen that mostly $Ro$ decreases as $Pm$ increases. This case can be explained by a simple consideration. $Pm$ is the ratio of kinematic viscosity to magnetic diffusivity, so as it increases, we can consider increasing kinematic viscosity. If the kinematic viscosity is higher, it is expected that more kinetic energy will disappear, which will result in decreasing $Ro$. However, this consideration is valid if $Pm$ has reached a saturation value for the dynamo. This also explains the decrease in $Re$ since it is proportional to $Ro$. As $Pm$ increases, $Rm$ also increases due to the direct proportionality to $Pm$. In $\Lambda$, the situation is different and depends on both $u_{rms}$ or $Ro$ and $Pm$; its value is determined due to an increased or decreased rate in these values.

**Control parameters (Input)**

| Parameter | Definition | Force balance | Model value | Earth value |
|---|---|---|---|---|
| Rayleigh number | $Ra = \alpha g_0 \Delta T d/\nu\kappa$ | buoyancy/diffusivity | $1 - 50 Ra_{\text{crit}}$ | $\gg Ra_{\text{crit}}$ |
| Ekman number | $E = \nu/\Omega d^2$ | viscosity/Coriolis | $10^{-6} - 10^{-4}$ | $10^{-14}$ |
| Prandtl number | $Pr = \nu/\kappa$ | viscosity/thermal diff. | $2{\cdot}10^{-2} - 10^{3}$ | $0.1 - 1$ |
| Magnetic Prandtl | $Pm = \nu/\eta$ | viscosity/magn. diff. | $10^{-1} - 10^{3}$ | $10^{-6} - 10^{-5}$ |

**Diagnostic parameters (Output)**

| Parameter | Definition | Force balance | Model value | Earth value |
|---|---|---|---|---|
| Elsasser number | $\Lambda = B^2/\mu\rho\eta\Omega$ | Lorentz/Coriolis | $0.1 - 100$ | $0.1 - 10$ |
| Reynolds number | $Re = ud/\nu$ | inertia/viscosity | $< 500$ | $10^{8} - 10^{9}$ |
| Magnetic Reynolds | $Rm = ud/\eta$ | induction/magn. diff. | $50 - 10^{3}$ | $10^{2} - 10^{3}$ |
| Rossby number | $Ro = u/\Omega d$ | inertia/Coriolis | $3{\cdot}10^{-4} - 10^{-2}$ | $10^{-7} - 10^{-6}$ |

Earth core values: $d \approx 2{\cdot}10^5$ m, $u \approx 2{\cdot}10^{-4}$ m s$^{-1}$, $\nu \approx 10^{-6}$ m$^2$s$^{-1}$

Fig. 3.13: Comparison of some calculated parameters of the Earth compared to the simulations' values. There are four input parameter values. There are huge differences between the Earth's parameters and the simulations' parameters. This is also true for the output parameters. In the bottom panel, we see some estimated numbers related to the Earth's core ([D. Schmitt, 2009]).

Fig. 3.13 provides some of the values of parameters related with the dynamo mechanism estimated for Earth. This mechanism is the source of the Earth magnetic field as mentioned earlier. As evident in the figure, there are huge differences in these parameters when comparing estimates for Earth to our simulations. This shows that we are far from the real Earth case. However, these simulations help us gain a better understanding of the dynamo mechanism. In our simulations, $E = 6.5 \cdot 10^{-5}$ and $Pr = 1$. If we compare these values with the estimated values for Earth, we see that the parameter values are

nearly the same for $Pr$. This shows that the ratio of viscosity to the magnetic diffusivity is almost equal. $E$ is much greater than the estimated Earth values. Hence, the effect of viscous forces compared to Coriolis forces is much greater. In our simulations shown in table 3.1, we have taken $Ra$ as $5 \cdot 10^4$, $1 \cdot 10^5$ and $1 \cdot 10^6$. These values are much smaller than the estimated Earth values. Since $Ra$ measures the ratio among buoyancy and diffusivity, the effect of buoyancy forces compared to the diffusive forces is smaller in the simulations than the estimated Earth effects. For $Pm$, the situation is different compared to $Ra$, and $Pm$ takes values between $5-100$. This time our simulation parameters are much greater. This means that in the simulations, viscous forces are too great compared to those estimated for Earth. $Re$ takes values between $19-80$. Then this means that the ratio of the inertial forces to the viscous forces is much smaller than the estimated Earth ratio. For $Ro$, the simulation values are greater than estimated Earth values. This means that the inertial to Coriolis force ratio is greater in the simulations. In the simulations, $\Lambda$ values include the estimated Earth values. Then, in some cases, the ratio of Lorentz force to Coriolis force is equal to the estimated ratios and in other cases, it is slightly greater. For $Rm$, our simulation results are within the range of the estimated Earth values. So the ratio of induction to magnetic diffusivity is of the order of estimated values. A more detailed table can be found at the end of this work.

The dipole graph for our simulations are not similar to the Earth's estimated dipole. If we consider the case at the surface of the Earth in our simulations, we also obtain a dipole structure for the magnetic field. However, our results do not resemble the dipole shown in fig. 2.7. Based on the large differences between the input parameters and some other effects, this is not an unexpected result.

An interesting coincidence between the Earth's estimates and our simulations is evident in our power laws for $B_{rms}$. The frequency value $f \approx 10^{-3}$ from our calculations is nearly equal to the Earth's estimate of $5Ma^{-1}$. This comparison is done using the dipole decay time. If we examine the PSD graph shown in fig. 2.5, we see that the frequency at that value starts to fall and the power law for this decrease is nearly $1/f^2$. In this graph, this decrease is observed in the third region. In most cases in our simulations, $f \approx 10^{-3}$ is the starting value of the $1/f^2$ power law or the decay at that frequency has already started and the $1/f^2$ power law is observed.

Thus, there is coincidental consistency between the calculated Earth PSD graph and our simulations. We also see another power law in fig. 2.5 just after the $1/f^2$ power law and it is approximately the $1/f^7$ power law. This value was also seen in some of cases in our

simulations.

## 3.2 Convection driven dynamos

In the previous section, we showed the results of the dynamo driven by gravitational convection. Here we will examine a different situation. We will take the buoyancy source as zero, $\epsilon = 0$, in the eqs. 3.1 and use fixed temperature boundary conditions on both inner and outer boundary conditions. This configuration gives a dynamo driven by convection due to the temperature difference. We will solve eqs. 3.1 with the abovementioned conditions. This new configuration changes one of the control parameters. Here, we have scaled temperature by $\Delta T$, the temperature difference between the inner and outer boundaries. This new scaling gives us the Rayleigh number $Ra = \frac{\alpha g_0 d^3 \Delta T}{\kappa \nu}$. All other control parameters and scalings are the same as previously described. The numerical solutions for different configurations of control parameters are given below. These solutions will be compared with the results of the gravitational dynamo.

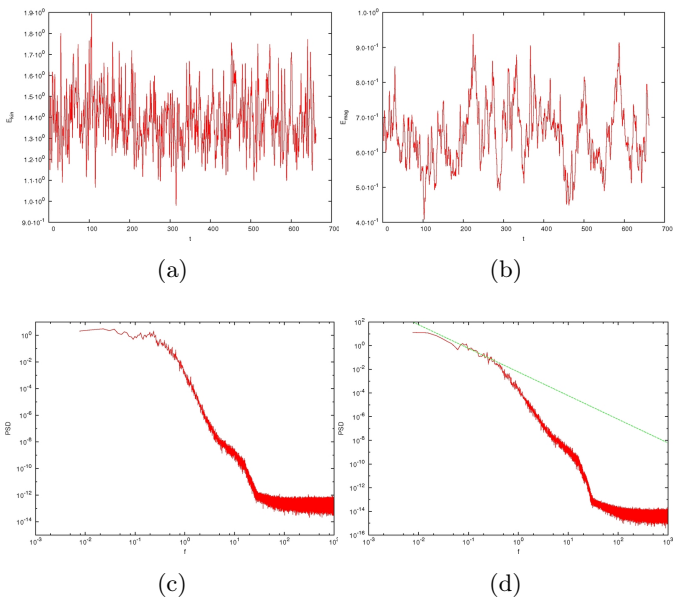

(a) (b)

(c) (d)

Fig. 3.14: Numerical results of the reversing dynamo at $Ra = 5 \cdot 10^5, Pm = 20, E = 6.5 \cdot 10^{-5}, Pr = 1$. a) Time series of the kinetic energy. b) Time series of the magnetic energy. c)PSD of $u_{rms}$. d ) PSD of $B_{rms}$.

Fig.3.14, fig.3.15 and fig.3.16 show the results and the analysis of the simulation at $Ra = 5 \cdot 10^5, Pm = 20, E = 6.5 \cdot 10^{-5}, Pr = 1$. At $Ra = 1 \cdot 10^6$, the numerical solution

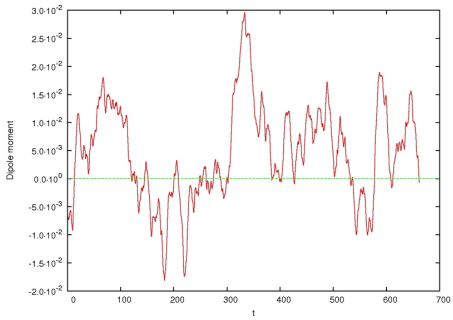


Fig. 3.15: Time series of the dipole moment at $Ra = 5 \cdot 10^5, Pm = 20, E = 6.5 \cdot 10^{-5}$ and $Pr = 1$.

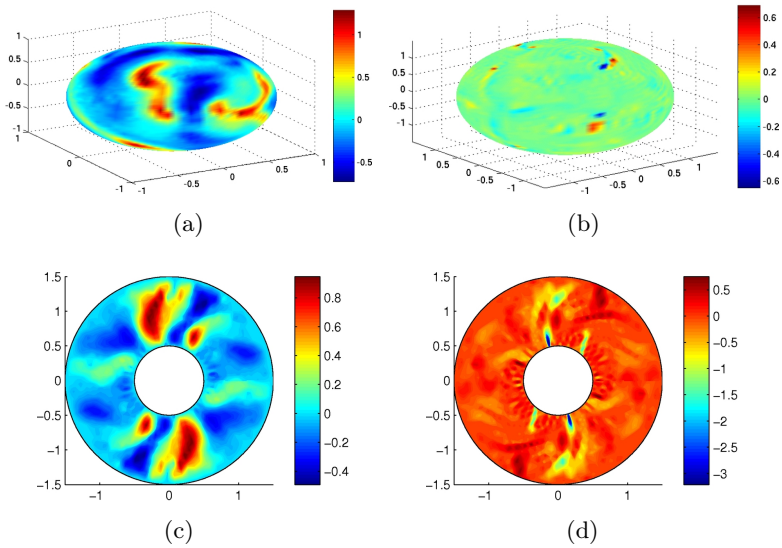


Fig. 3.16: Structure of the reversing dynamo at $Ra = 5 \cdot 10^5, Pm = 20, E = 6.5 \cdot 10^{-5}, Pr = 1$. a) Radial component of the velocity field $u_r$ at $r = (r_i + r_o)/2$. b) Radial component of the magnetic field $B_r$ on the core mantle boundary. c) Radial component of the velocity field $u_r$ in the equatorial plane. d) Radial component of the magnetic field $B_r$ in the equatorial plane.

resulted in infinities. So we have taken $Ra$ as $5 \cdot 10^5$ and will compare this case with the previous gravitational dynamo at $Ra = 1 \cdot 10^6$. Fig.3.14 shows the time series of the magnetic and kinetic energy and PSDs of $u_{rms}$ and $B_{rms}$. The PSD of $u_{rms}$ is nearly constant for low frequencies and the PSD of $B_{rms}$ decreases as $1/f^2$ for the same frequency interval. For the gravitational dynamo at $Ra = 1 \cdot 10^6$, we have $1/f$ dependence on $f$ for the PSD of $u_{rms}$. This is the first difference between these two cases. Different power laws for the high frequency spectrum are detailed in tab. 3.2.

The axial component of the dipole moment is shown in fig.3.15. Magnetic reversals are easily observed, which is nearly identical to the gravitational dynamo results. The dipole decay time is again $t_d = 702$ and the whole simulation time corresponds to 19kyr.

In fig.3.16, we see radial components of the the velocity field at $r = (r_i + r_o)/2$ and in the equatorial plane and the magnetic field on the core mantle boundary and in the equatorial plane. There are six cyclonic and six anticyclonic vortices in the velocity field. However, they are irregular and this is observed in the equatorial plane. The velocity field at $r = (r_i + r_o)/2$ also shows this structure, but the columnar structure is not smooth. The magnetic field on the core mantle boundary shows a structure different than a dipole field and it is difficult to say anything about the field over the mantle. The magnetic field in the equatorial plane is really complicated. But one can still see the effects of the columns of the velocity field. Comparing these results to the gravitational dynamo, we see that the situation is totally different. The deviations from a dipole in the magnetic field are much greater in this solution with respect to the gravitational one.

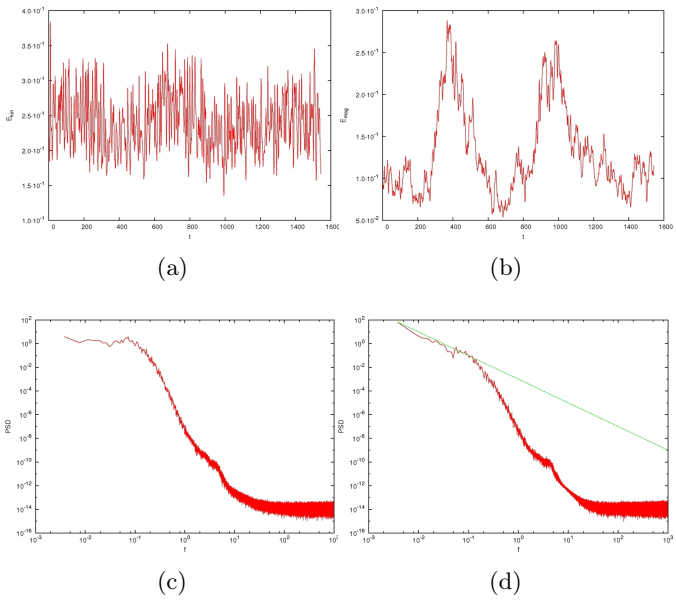


Fig. 3.17: Numerical results of the reversing dynamo at $Ra = 1 \cdot 10^5, Pm = 20, E = 6.5 \cdot 10^{-5}, Pr = 1$. a) Time series of the kinetic energy. b) Time series of the magnetic energy. c)PSD of $u_{rms}$. d ) PSD of $B_{rms}$.

Fig.3.17, fig.3.18 and fig.3.19 are the results and the analysis of the simulation at $Ra = 1 \cdot 10^5, Pm = 20, E = 6.5 \cdot 10^{-5}, Pr = 1$. Fig.3.17 shows the time series of the magnetic and kinetic energy and PSDs of $u_{rms}$ and $B_{rms}$. The PSD of $u_{rms}$ is constant for the low

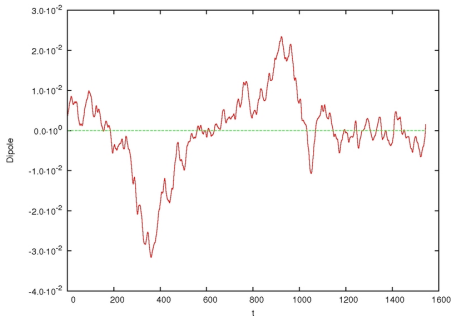


Fig. 3.18: Time series of the dipole moment at $Ra = 1 \cdot 10^5, Pm = 20, E = 6.5 \cdot 10^{-5}$ and $Pr = 1$.

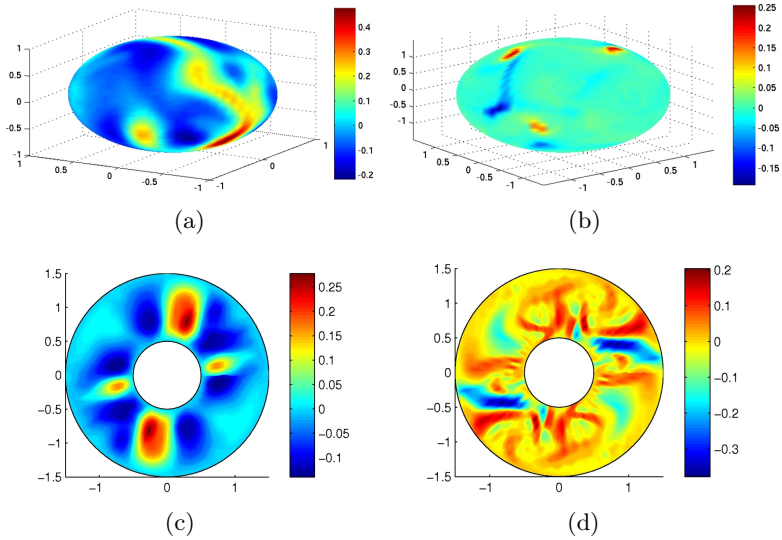


Fig. 3.19: Structure of the dynamo at $Ra = 1 \cdot 10^5, Pm = 20, E = 6.5 \cdot 10^{-5}, Pr = 1$. a) Radial component of the velocity field $u_r$ at $r = (r_i + r_o)/2$. b) Radial component of the magnetic field $B_r$ on the core mantle boundary. c) Radial component of the velocity field $u_r$ in the equatorial plane. d) Radial component of the magnetic field $B_r$ in the equatorial plane.

frequency interval and the PSD of $B_{rms}$ decreases as $1/f^2$ for the same frequency interval. These properties are the same as the gravitational dynamo case for the same control parameters, as shown in fig. 3.4. There are different power laws for high frequencies, which can be found in tab. 3.2.

The axial component of the dipole moment is shown in fig.3.18. Again, there are magnetic reversals just like the gravitational dynamo case. The dipole decay time is $t_d = 702$ and the whole simulation time corresponds to 44kyr.

Fig.3.19 shows the radial components of the the velocity field at $r = (r_i + r_o)/2$ and in the equatorial plane and the magnetic field on the core mantle boundary and in the equatorial plane. In the velocity field, there are four cyclonic and four anticyclonic vortices This is observable in both cases: on the equatorial plane and at $r = (r_i + r_o)/2$. However this structure is irregular. The magnetic field is complex on the core mantle boundary and is hardly reminiscent of a dipole field. The magnetic field also has a complex structure in the equatorial plane. It is really difficult to construct any similarities between the magnetic and velocity fields. In the gravitational dynamo simulation, we also had four columnar structures in the velocity field. However, the situation is different for the magnetic field; here, it is much more complicated than the gravitational dynamo for the same control parameters.

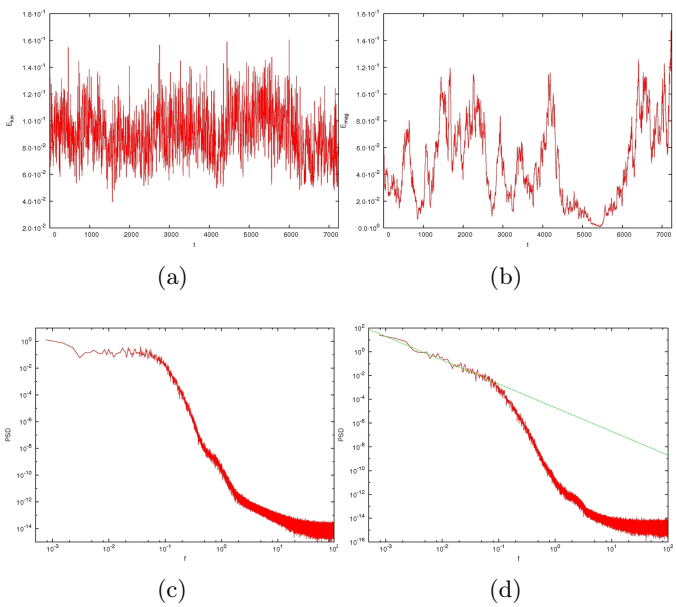


Fig. 3.20: Numerical results of the reversing dynamo at $Ra = 5 \cdot 10^4, Pm = 20, E = 6.5 \cdot 10^{-5}, Pr = 1$. a) Time series of the kinetic energy. b) Time series of the magnetic energy. c) PSD of $u_{rms}$. d) PSD of $B_{rms}$.

Fig.3.20, fig.3.21 and fig.3.22 provide the results and the analysis of the simulation at $Ra = 5 \cdot 10^4, Pm = 20, E = 6.5 \cdot 10^{-5}, Pr = 1$. Fig.3.20 shows the time series of the magnetic and kinetic energy and PSDs of $u_{rms}$ and $B_{rms}$. The PSD of $u_{rms}$ is more or less constant for low frequencies and the PSD of $B_{rms}$ declines with $1/f^2$ for the same frequencies. Apart from the peaks and repeated structures, this solution has similar properties to the gravitational dynamo. For high frequencies, there are different power

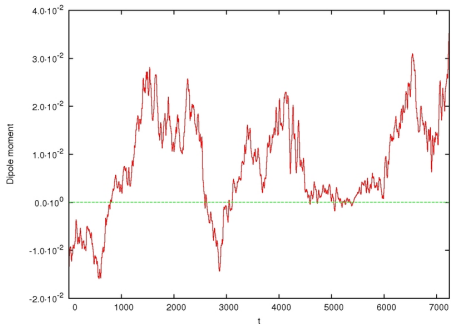


Fig. 3.21: Time series of the dipole moment at $Ra = 5 \cdot 10^4, Pm = 20, E = 6.5 \cdot 10^{-5}$ and $Pr = 1$.

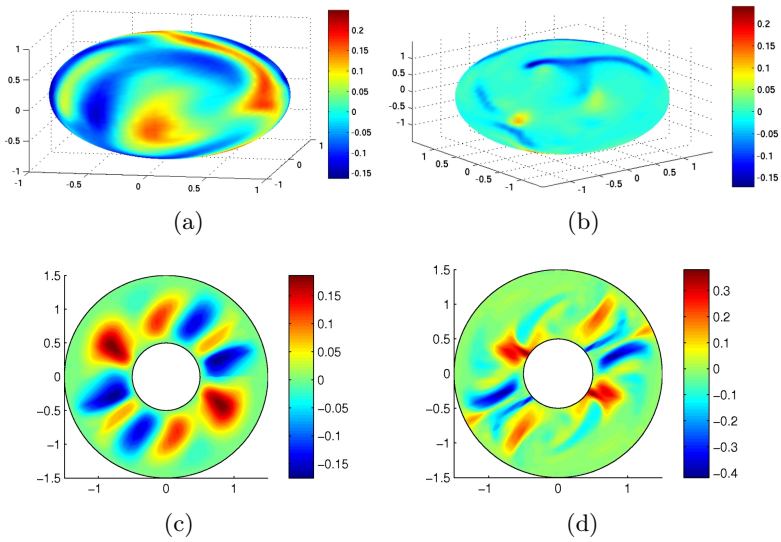


Fig. 3.22: Structure of the dynamo at $Ra = 5 \cdot 10^4, Pm = 20, E = 6.5 \cdot 10^{-5}, Pr = 1$. a) Radial component of the velocity field $u_r$ at $r = (r_i + r_o)/2$. b) Radial component of the magnetic field $B_r$ on the core mantle boundary. c) Radial component of the velocity field $u_r$ in the equatorial plane. d) Radial component of the magnetic field $B_r$ in the equatorial plane.

laws as detailed in tab. 3.2.

Fig.3.21 shows the axial component of the dipole moment. This solution results in some magnetic reversals. However, the gravitational dynamo case for the same configuration had no magnetic reversals. The dipole decay time is again $t_d = 702$, and this time the whole simulation time corresponds to 256kyr.

Fig.3.22 shows the radial components of the velocity field at $r = (r_i + r_o)/2$ and in

| $Ra$ | $Pm$ | $\Lambda$ | $Re$ | $Rm$ | $Ro$ | L$f$ PL ($B_{rms}$) | H$f$ PL ($B_{rms}$) | L$f$ PL ($u_{rms}$) | H$f$ PL ($u_{rms}$) |
|---|---|---|---|---|---|---|---|---|---|
| $5 \cdot 10^5$ | 5 | 26.1 | 79.6 | 206 | 0.517 | -2 | -8 | 0 | -10 |
| | 10 | 110 | 73.5 | 351 | 0.478 | -2 | -7 | -1&0 | -9 |
| | 20 | 292 | 69.4 | 627 | 0.451 | -2 | -6 | -1&0 | -8 |
| | 30 | 516 | 67.5 | 888 | 0.439 | -1.6 | -6 | -1&0 | -8 |
| $1 \cdot 10^5$ | 5 | 0.035 | 32.6 | 34.6 | 0.212 | -2 | -10 | 0 | -12 |
| | 10 | 17.8 | 30.1 | 58.9 | 0.196 | -2.5 | -8 | 0 | -10 |
| | 20 | 57 | 28.7 | 107 | 0.187 | -2 | -8 | 0 | -9 |
| | 30 | 150 | 27.1 | 144 | 0.176 | -2.5 | -8 | 0 | -9 |
| $5 \cdot 10^4$ | 10 | 0.021 | 19.3 | 24.2 | 0.125 | -2 | -10 | 0 | -14 |
| | 20 | 18.9 | 17.6 | 40.2 | 0.114 | -2 | -8 | 0 | -10 |
| | 30 | 48.1 | 16.7 | 54.9 | 0.109 | -2 | -8 | -0.6 | -9 |

Tab. 3.2: *Convention driven dynamo simulation results. The first two column show control parameters $Ra$ and $Pm$. Since two of the parameters are constant for these results, they are not shown and $E = 6.5 \cdot 10^{-3}$ and $Pr = 1$. The next four columns show output parameters $\Lambda$, $Re$, $Rm$ and $Ro$. The 7th and 8th columns show low frequency interval power law (L$f$ PL) and high frequency interval power law (H$f$ PL) for the spectrum of $B_{rms}$, respectively. The 9th and 10th columns show similar power laws for the spectrum of $u_{rms}$.*

the equatorial plane and the magnetic field on the core mantle boundary and in the equatorial plane. There is a complicated structure in the velocity field $r = (r_i + r_o)/2$. There are six cyclonic and six anticyclonic vortices that are observed in the equatorial plane and at $r = (r_i + r_o)/2$. However, two of the anticyclonic vortices are weak and hard to notice. This property is similar to the gravitational dynamo case. The magnetic field on the core mantle boundary is different than a dipole field. The magnetic field in the equatorial plane has a different structure than the velocity field and it is hard to construct a relationship between them. The magnetic field structure has changed from the gravitational dynamo to this solution. Dipole property has been lost.

Table tab.3.2 provides detailed information from the simulation results of the different

configurations. The power law for $B_{rms}$ at low frequencies is -2 in most cases. Within the same frequency interval, the power law for $u_{rms}$ is constant. At high frequencies, the situation is more complicated. There is no clear relationship. If we compare these results with the gravitational dynamo, we see two main differences. The first one is that the -1 power law for $u_{rms}$ is not observed in these solutions. The second difference is that we have a few cases which deviate from the -2 power law for $B_{rms}$. This table also shows the Elsasser number $\Lambda$, Reynolds number $Re$, magnetic Reynolds number $Rm$ and Rosby number $Ro$. The results show that $Ro$ decreases as $Pm$ increases. Since $Re$ is proportional to $Ro$, as $Pm$ increases, $Re$ also decreases. $\Lambda$ and $Rm$ increase as $Pm$ increases due to direct proportionality. A more detailed table is located at the end of this work.

Now let us consider the simulation input and output parameters. In our simulations, we have taken $E = 6.5 \cdot 10^{-5}$ and $Pr = 1$. If we compare these values to the estimated ones for Earth, we see that our parameter for $Pr$ is in the same range as estimates. This means that the ratio of viscosity to the magnetic diffusivity is nearly the same. The $E$ is much bigger than the estimate. So, there is a much larger effect of viscous forces compared to the Coriolis forces. $Ra$ is set to the values $5 \cdot 10^4$, $1 \cdot 10^5$ and $5 \cdot 10^5$ and these values are much smaller than the estimated Earth values. This means that the ratio of buoyancy forces due to the temperature difference between the outer boundary and inner boundary of the liquid core and diffusive forces is much smaller than the estimated Earth values. So, the effect of the buoyancy force is smaller in our simulations. $Pm$ changes between 5 and 30 and this is also greater than the estimated Earth values. This means that the viscous forces compared to the magnetic diffusive forces are stronger. Elsasser number $\Lambda$ values include estimated Earth values. Then the ratio of Lorentz force to Coriolis force is in our simulation is either equal to our greater than the estimated ratios. $Re$ is much smaller and this shows that the inertial forces compared to the viscous forces are also much smaller. Our simulation results for $Rm$ are within the range of estimated Earth values. So the ratio of induction to magnetic diffusivity is of the order of estimated values. The other parameter, $Ro$, is greater and the ratio of inertial forces to the Coriolis force is greater.

The dipole graphs from our simulations are not quite similar to the Earth's dipole shown in fig.2.7. If one considers the case over the crust in our simulations, it is still hard to obtain a dipole structure for the magnetic field. This may be due to differences in the input parameters between our simulations and those estimated for Earth.

If we consider the frequency $f \approx 10^{-3}$ from our calculations, this value is nearly equal to $5Ma^{-1}$ for the Earth, similar to the results of previously shown gravitational dynamo simulations. Again this comparison is done using the dipole decay time. Then, if we compare our PSD graphs with the one shown in fig. 2.5, this frequency coincides with the third region in the graph. Here, the power law for the decay is approximately $1/f^2$. This is same power law as that obtained from our simulations. Just after the $1/f^2$ power law, another power law in fig. 2.5 is approximately $1/f^7$. We also observed this value in some cases in our simulations.

# 4 Phenomenological Models

Eqs. 3.1 ,the dynamo equations, form a complex structure. Here, the velocity is the solution to the Navier-Stokes equation. The velocity is also present in the induction equation and heat or buoyancy source equation. There are many factors that affect the velocity field, an observation which can be easily seen from the Navier-Stokes equation and for stable dynamo solutions. These effects result in a fluctuating velocity field. We can replace the fluctuating variable, in this case velocity field, with a stochastic random variable and use this variable in the other equations. For this purpose, we will consider only the solution of the induction equation and can write it as

$$\frac{\partial \vec{B}}{\partial t} + \nabla \times (\vec{B} \times \vec{v}) = \lambda \nabla^2 \vec{B} \tag{4.1}$$

where $\lambda$ is the magnetic diffusivity, $\vec{v}$ is the velocity and $\vec{B}$ is the magnetic field. In this section we will use phenomenological models and a random variable for the velocity field in order to analyze changes in the magnetic field. After determining the changes in the magnetic field due to this random variable, we will also calculate the PSD of the magnetic field. We will apply two phenomenological models, a single magnetic mode and several magnetic modes. Some of the results presented in this section have already been published ([Tanriverdi and Tilgner, 2011]).

## 4.1 A single magnetic mode

Mean field magnetohydrodynamics have provided a most fruitful simplification of the induction equation ([Krause and Radler, 1980]). In this approach, the effect of small scale fluctuations on the large scales are not computed exactly, but are modeled, in the simplest case, as an $\alpha-$effect. We have also previosly mentioned on this effect. The number of magnetic degrees of freedom which need to be retained is thus reduced; in an extreme simplification, only one mode remains. If we call $B$ the amplitude of that mode,

$\tilde{\alpha}(t)$ and $\beta$ the coefficients describing the $\alpha-$effect and its quenching, respectively, and $\mu$ is a coefficient related to magnetic dissipation, the simplest model reproducing the main features of the induction equation is:

$$\partial_t B = \tilde{\alpha}(t)B - \beta B^3 - \mu B. \tag{4.2}$$

$\tilde{\alpha}$ is allowed to be time dependent in order to reflect a time dependent velocity field. The reduction of the $\alpha-$effect by the term $\beta B^3$ models the retroaction of the magnetic field on the velocity field via the Lorentz force (which is quadratic in the magnetic field) in the Navier-Stokes equation. We now consider $\alpha(t) = \tilde{\alpha}(t) - \mu$ to be a random process with mean square $\langle\alpha^2\rangle$ and remove the dimensions from eq. 4.2 by expressing time in multiples of $\langle\alpha^2\rangle^{-1}$ and the magnetic field amplitude in multiples of $(\langle\alpha^2\rangle/\beta)^{1/2}$. The adimensional quantities $t'$, $\alpha'$ and $B'$ are given by $t' = t\langle\alpha^2\rangle$, $\alpha' = \alpha/\langle\alpha^2\rangle$ and $B' = B\sqrt{\beta/\langle\alpha^2\rangle}$. In the remainder of this section, all quantities are understood to be non-dimensional and the primes are omitted for convenience. The non-dimensional variables then obey the equation:

$$\partial_t B = \alpha(t)B - B^3 \tag{4.3}$$

in which $\alpha(t)$ is a random variable with $\langle\alpha^2\rangle = 1$. As long as $B$ is small, the solution to this equation is

$$B(t) = B(0)\exp\left(\int_0^t \alpha(\tau)d\tau\right). \tag{4.4}$$

For times small enough so that the exponent can be considered small, we have

$$\frac{B(t) - B(0)}{B(0)} \approx \int_0^t \alpha(\tau)d\tau. \tag{4.5}$$

Taking the Fourier transform of this equation, it follows that the spectrum of $B$ is, apart from frequency independent factors, the same as the spectrum of $\alpha$ divided by the square of the angular frequency, $\omega^2$. For example, if the spectrum of $\alpha$ is a white noise, the spectrum of $B$ behaves as $\omega^{-2}$. For large times $t$, eqs. 4.4 and 4.3 become a poor approximation, which means that the $\omega^{-2}$ will not be observable below some cutoff-frequency. If the mean of $\alpha$, $\langle\alpha\rangle$, is different from zero, $B$ will be large enough for the nonlinear term in eq. 4.3 to become dominant after a time to the order of $\langle\alpha\rangle^{-1}$. In that regime, and concentrating on slow fluctuations, eq. 4.3 reduces to $B^2 = \alpha$. Considering again the example of $\alpha(t)$ with a white noise, we find a spectrum of $B$, which is a white noise, too. The transition in the spectrum of $B$ from $\omega^0$ to $\omega^{-2}$ occurs at a frequency which increases with increasing $\langle\alpha\rangle$ because eq. 4.5 fails at earlier times $t$.

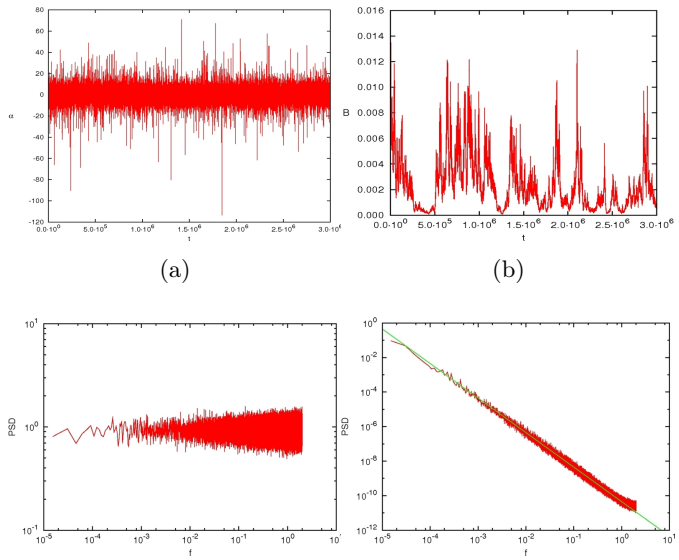


FIG. 4.1: Numerical solution of Eq.(4.3) for $\langle\alpha\rangle = 0$. a) Time series of $\alpha$. b) Time series of $B$. c) PSD of $\alpha$. d) PSD of $B$; the straight line indicates the power law $1/f^2$.

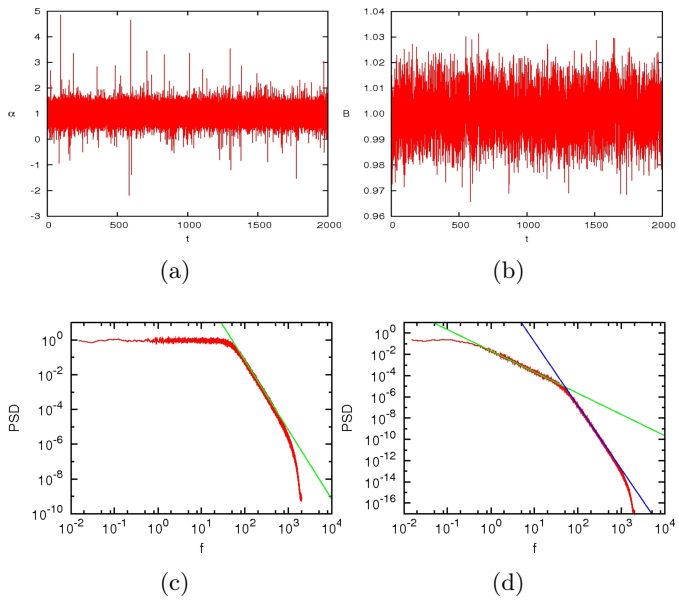


FIG. 4.2: Numerical solution of Eq.(4.3) for $\langle\alpha\rangle = 1$ and $\alpha$ has been filtered. a) Time series of $\alpha$. b) Time series of $B$. c) PSD of $\alpha$ and straight line indicates the power law $1/f^4$. d) PSD of $B$; the straight lines indicate the power laws $1/f^2$ and $1/f^6$.

In order to test these ideas, we have solved eq. 4.3 numerically using the Runge-Kutta method. The first solution is shown in fig. 4.1. Fig. 4.1a shows the time series of $\alpha$ generated from a Gaussian random number generator with a mean of zero. Fig. 4.1c depicts the PSD of $\alpha$, which is white noise. Fig. 4.1b shows the numerical solution for B and its PSD is shown in fig. 4.1d. The PSD obeys the $1/f^2$ power law where $f = \omega/(2\pi)$. We previously concluded that if $\alpha$ has a white noise spectrum, then a $1/f^2$ factor results from integration, and finally we get the result $1/f^2$ for the PSD of $B$. Hence, the simulation results and our considerations are consistent.

As a second example, we will use the random number $\alpha(t)$ with a white noise spectrum and $\langle\alpha\rangle = 1$. However, this time we have filtered the high frequency fluctuations. The random number $\alpha(t)$ was generated by sending the output of a Gaussian deviate random number generator through a Butterworth filter ([Moreau], [Rabiner and Gold, 1975]). This filter uses a function in the form $1/(1+(f/f_c)^{2n})$ and passes frequencies lower than $f_c$. Here $f_c$ is the cut off frequency and $n$ is the order of the filter, which defines power law in the filtering. The filter was adjusted such that its output had a spectrum as a function of frequency $f$ in $1/(1+(f/f_1)^4)$ with $f_1 = 50$. The time series of $\alpha(t)$ is shown in fig. 4.2a. Its PSD is shown in fig. 4.2c and here, the $1/f^4$ power law due to filtering is easily observable. Fig. 4.2b shows the numerical solution for $B$ and its PSD is given in fig. 4.2d. There we see the $1/f^6$ power law for high frequencies. In this frequency interval, integration gives a $1/f^2$ factor and multiplication with $1/f^4$ gives this $1/f^6$ power law. Then as we proceed to the low frequencies we see the $1/f^2$ power law, which comes from the integration of white noise. This is exactly the same as with the previous example. If we look at the lowest frequency range for $B$, we observe a section of white noise. Since the mean of $\alpha(t)$ is 1, it affects the integration. We have also mentioned that in this range, the nonlinear term $B^3$ plays a role because it is no longer small. This explains the white noise in the PSD of $B$ at low frequencies.

Fig. 4.3 shows the PSD of three numerical solutions of $B$, with one of them being the second example discussed above for $\langle\alpha\rangle = 1$. We used the same random number sequence for $\alpha$ in all three cases. The changing variable for these three examples is the mean of $\alpha$, which takes values of 1,5 and 15. From our previous considerations, we know that the mean of $\alpha$ affects the low frequency range. This effect is easily observed in fig. 4.3. As the mean of $\alpha$ increases, the white noise range for the spectrum of $B$ increases. This is what we expected. In the high frequency range, the arguments of the second example are valid for all three cases.

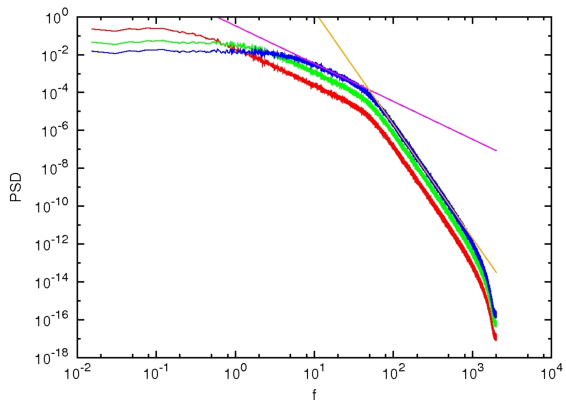


Fig. 4.3: The PSD of $B$, the solution of eq. 4.3, as a function of frequency $f$ for $\langle\alpha\rangle = 1$ (red), 5 (green) and 15 (blue). The straight lines indicate the power laws $1/f^2$ and $1/f^6$.

## 4.2 Several magnetic modes

We will now investigate several magnetic modes and the conditions under which the single mode model is applicable to more general systems. We will show that the predictions of the single mode model are recovered in the limit of small fluctuations.

The precise form of the dynamical system used as a model does not really matter for the following analysis, but a specific system must be chosen for the numerical examples. In order to stay as close as possible to the previous section, let us assume $\nabla \cdot \vec{v} = 0$ and rewrite the left hand side of eq. 4.1 as $\partial_t B_i + \sum_j v_j \partial_j B_i - \sum_j B_j \partial_j v_i$. We then proceed through the same steps as before, but replace the combination of velocity and derivation with a random variable in which we absorb the dissipative term and the right hand side, remove dimensions, and model saturation via a cubic term. This leads to the following system:

$$\partial_t B_i + (\alpha_1(t) + \alpha_2(t) + \alpha_3(t))B_i - \alpha_i(t)(B_1 + B_2 + B_3) = -B_i^3 \quad , \quad i = 1, 2, 3, \quad (4.6)$$

in which $\alpha_i(t)$ are random variables. This system bears only a metaphorical relation with the original induction equation and will be used to exemplify three different cases: 1)if the fluctuations of the $\alpha_i(t)$ are small compared with the mean of the $\alpha_i(t)$, 2)if the fluctuations of the $\alpha_i(t)$ are large and 3)if the fluctuations of the $\alpha_i(t)$ are of the same order as the mean of the $\alpha_i(t)$.

In case 1, where the fluctuations of the $\alpha_i(t)$ are small compared with the mean of the $\alpha_i(t)$, the solution of (4.6) will be close to the solution of the time independent system

in which each $\alpha_i(t)$ in (4.6) is replaced by its mean $\langle\alpha_i\rangle$. Let us assume $\langle\alpha_1\rangle = \langle\alpha_2\rangle = \langle\alpha_3\rangle < 0$. An eigenvalue analysis of the left hand side of (4.6) then reveals one neutral mode and two modes with equal and positive growth rate. In the presence of small fluctuations, the neutral mode will not contribute significantly to the dynamics. If the initial conditions and nonlinear term select an arbitrary direction in the space spanned by the two degenerate growing modes, we expect (4.6) to behave the same as the single mode model. However, there are some differences.

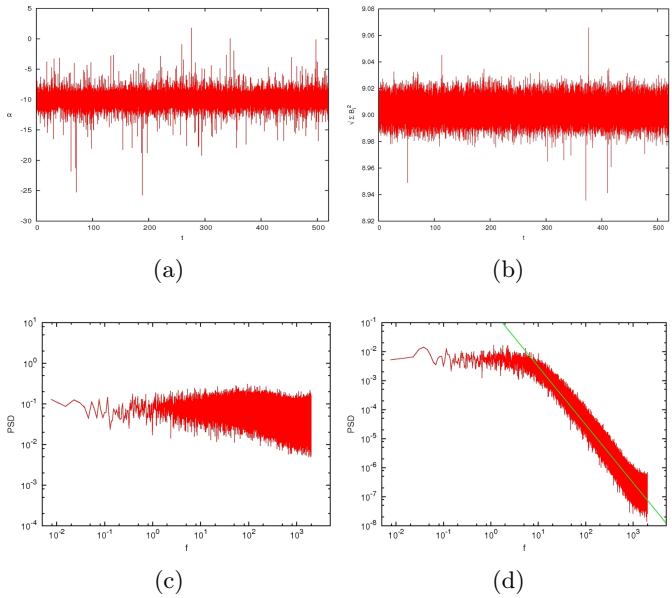


Fig. 4.4: Numerical solution of eq.(4.6) for $\langle\alpha_i\rangle = -10$. a) Time series of $\alpha_1$. b) Time series of $\sqrt{\sum B_i^2}$. c) PSD of $\alpha_1$. d) PSD of $\sqrt{\sum B_i^2}$; the straight line indicates the $1/f^2$ power law.

Fig. 4.4 shows the numerical solution of eq. 4.6. In this solution, $\langle\alpha_i^2\rangle = 1$, $\langle\alpha_i\rangle = -10$ and its spectrum is white noise. The time series of $\alpha_i$ is shown in fig. 4.4a and its PSD is shown in fig. 4.4c. The numerically obtained solution of $\sqrt{\sum B_i^2}$ is shown in fig. 4.4b. The numerical solution yields the $1/f^2$ type of power law for $\sqrt{\sum B_i^2}$, which is shown in fig. 4.4d. If we compare this solution with the one shown in fig. 4.2, the results appear similar. The exceptions are that there is not a $1/f^4$ dependence in the high frequency regime for $\alpha$ and $\sqrt{\sum B_i^2}$ has a $1/f^6$ dependence. Similar to the solution in 4.2, here we also observe white noise for the low frequency regime and the $1/f^2$ power law for the high frequency regime, as expected. The white noise in the PSD of $\sqrt{\sum B_i^2}$ is related to the mean of $\alpha$ and we explained this feature in the previous section.

On the other hand, if the fluctuations of $\alpha_i$ are large compared to their means, the dynamics are no longer dominated by a single mode and the analysis provided in the previous section breaks down. In this case, the other modes start to show themselves and analysis becomes much more complicated than the single mode computation. The spectrum of the fluctuations of $\sqrt{\sum B_i^2}$ may now be different due to these complicated interactions. Now we will attempt to analyze this complicated structure both numerically and analytically.

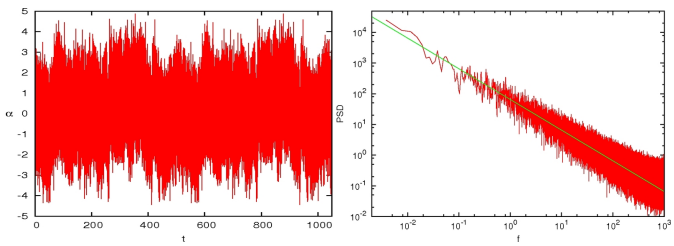


(a) (b)

Fig. 4.5: a) Time series of $\alpha$ with mean -0.01. b) PSD of $\alpha$; the straight line indicates the $1/f$ power law.

Fig. 4.5 shows the time series of $\alpha_i$ and its PSD at $\langle\alpha_i\rangle = -0.01$ and $\langle\alpha_i^2\rangle = 1$. Here we see that its PSD obeys the $1/f$ power law and is chosen due to the existence of the velocity field's $1/f$ power law in some of the gravitational dynamo simulations. The random number sequence is obtained by applying the method of ([Kasdin, 1995]). In this method, the response function is $h_k = \left(\frac{\alpha}{2} + k - 1\right)\frac{h_{k-1}}{k}$ together with $h_0 = 1$. In this equation, $\alpha$ gives the power law. This response function is used to obtain a $1/f^\alpha$ power law in the PSD from a Gaussian deviate random number sequence. In our case, we need a $1/f$ power law, and we have taken $\alpha$ as 1. This method is also used to obtain the other random number sequences for $\langle\alpha_i\rangle = -0.3$ and $\langle\alpha_i\rangle = -5$ with $\langle\alpha_i^2\rangle = 1$. These values will also have the $1/f$ power law in their power spectrum. Fig. 4.5 is a typical example for the $\alpha_i$, which will be used in the next calculations. The only difference will be the mean of $\alpha_i$ and this difference does not effect its spectrum.

Fig. 4.6 shows some examples of solutions of eq. 4.6. Let us first consider the case in which the fluctuations of $\alpha_i$ are small compared to their mean. The time series and PSD of $\sqrt{\sum B_i^2}$ are shown in fig. 4.6c and fig. 4.6f for $\langle\alpha_i\rangle = -5$. Since the fluctuations are small in this case, it should then behave in a similar way to the single mode model: at the lowermost frequencies, the PSD of $\sqrt{\sum B_i^2}$ must decay in the same way as the PSD of $\alpha_i$, i.e. $1/f$ in the present example. However, there is a difference in this case compared

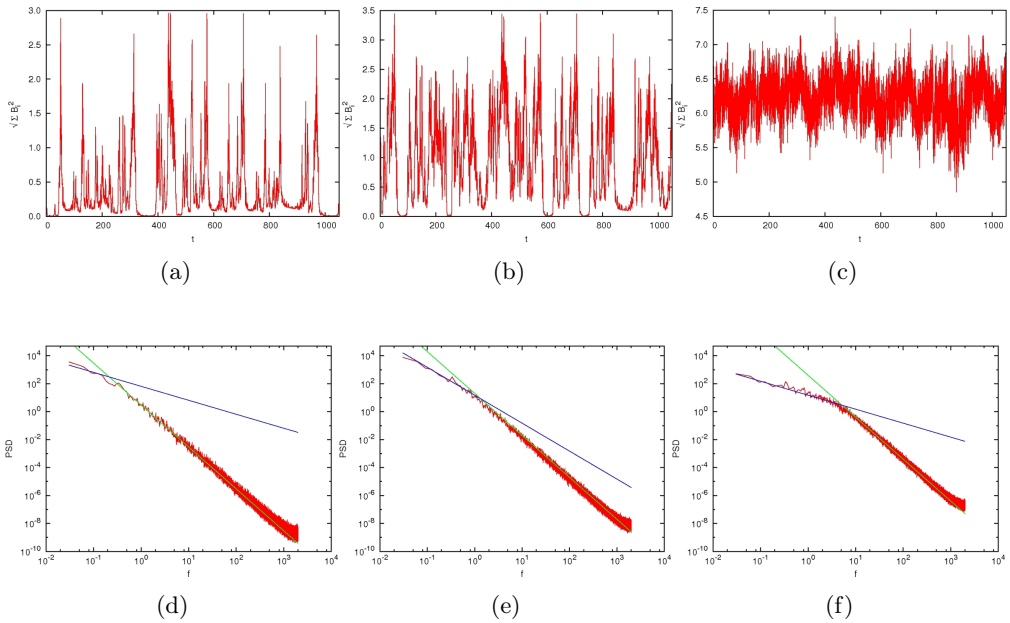


Fig. 4.6: Numerical solutions of eq.(4.6) for $\langle\alpha_i\rangle = -0.01, -0.3, -5$. a) Time series of $\sqrt{\sum B_i^2}$ for $\langle\alpha_i\rangle = -0.01$. b) Time series of $\sqrt{\sum B_i^2}$ for $\langle\alpha_i\rangle = -0.3$. c) Time series of $\sqrt{\sum B_i^2}$ for $\langle\alpha_i\rangle = -5$. d) PSD of $\sqrt{\sum B_i^2}$ for $\langle\alpha_i\rangle = -0.01$; straight lines indicate the $1/f$ and $1/f^3$ power laws. e) PSD of $\sqrt{\sum B_i^2}$ for $\langle\alpha_i\rangle = -0.3$; straight lines indicate the $1/f^2$ and $1/f^3$ power laws. f) PSD of $\sqrt{\sum B_i^2}$ for $\langle\alpha_i\rangle = -5$; straight lines indicate the $1/f$ and $1/f^3$ power laws.

to the single mode and we will discuss this difference later. Above a frequency of the order of $\langle\alpha_i\rangle$, there must be a factor $f^2$ between the power laws followed by the PSD of $\sqrt{\sum B_i^2}$ and $\alpha_i$. This implies a spectrum in $1/f^3$ for $\sqrt{\sum B_i^2}$ in the example considered here. These predictions fit the spectrum shown in fig. 4.6f for $\langle\alpha_i\rangle = -5$. We will leave the example with the $1/f^2$ power law to the end and look at the time series and PSD of $\sqrt{\sum B_i^2}$ shown in fig. 4.6a and fig. 4.6d for $\langle\alpha_i\rangle = -0.01$. Our previous considerations for high frequencies are still valid, but with a few changes. In this high frequency interval, we have the $1/f^3$ power law and this continues until the frequencies reach the order of $\langle\alpha_i\rangle = -0.01$. Then we have the $1/f$ power law and this is due to the other modes as well as nonlinear effects. Now let us look at the last case: $\langle\alpha_i\rangle$ is close to $\langle\alpha_i^2\rangle$. The time series and PSD of $\sqrt{\sum B_i^2}$ are shown in fig. 4.6b and fig. 4.6e for $\langle\alpha_i\rangle = -0.3$. Again, we have the $1/f^3$ power law for high frequencies. However, the situation is completely different for low frequencies. In this case, we have the $1/f^2$ power law, which cannot be explained

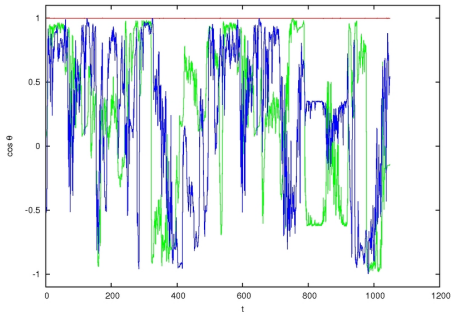


Fig. 4.7: $cos\theta$ at $\langle\alpha_i\rangle = -0.01$ (green), -0.3 (blue) and -5 (red).

by the single mode considerations. Single mode calculations give the $1/f$ or $1/f^3$ power laws. This $1/f^2$ power law for low frequencies is an important result for this work since it gives the combination seen in the gravitational dynamo simulations: the $1/f$ power law for $u_{rms}$ and the $1/f^2$ power law for $B_{rms}$. We could only obtain this combination by considering several modes; the single mode calculations did not give this solution. This several magnetic mode model reproduced the power laws of the our dynamo simulations for low frequencies without solving the Navier-Stokes equation. This means that we do not need to know the individual interactions in the Navier-Stokes equation in order to obtain the PSD of $B_{rms}$. The important parameters are the $|\langle\alpha_i\rangle|/\langle\alpha_i^2\rangle$ ratio and the power law(s) of the fluctuations.

In order to further support the applicability of the single mode model, we also computed the angle between the instantaneous vector $\vec{B}(t) = (B_1(t), B_2(t), B_3(t))$ and its mean $\langle\vec{B}\rangle$. The cosine of that angle $cos\theta = \langle\vec{B}\rangle \cdot \vec{B}(t)/\sqrt{|\langle\vec{B}\rangle|^2\ |\vec{B}(t)|^2}$ is shown in fig. 4.7. for $\langle\alpha_i\rangle = -5$, it is in the statistically stationary state and stays larger than 0.99. This result means that in this case, $\langle\vec{B}\rangle$ and $\vec{B}(t)$ are nearly in the same direction. So the other modes rarely affect the result. However $cos\theta$ is scattered over a large interval for $\langle\alpha_i\rangle = -0.01$ and $-0.3$. In these cases, the fluctuations of $\alpha_i$ are large compared to their means and different exponents unrelated to the single mode model become possible. So several modes appear and its effect is bigger than in the $\langle\alpha_i\rangle = -5$ case.

Let us summarize these results in terms of the $|\langle\alpha_i\rangle|/\langle\alpha_i^2\rangle$ ratio. Our simulations show that if $|\langle\alpha_i\rangle|/\langle\alpha_i^2\rangle \geq 5$, the single mode considerations are dominant and we have the $1/f$ and $1/f^3$ power laws. If $|\langle\alpha_i\rangle|/\langle\alpha_i^2\rangle \approx 0.3$, the other modes appear and we have the $1/f^2$ and $1/f^3$ power laws. If $|\langle\alpha_i\rangle|/\langle\alpha_i^2\rangle \approx 0.01$, the other modes are observed and we have the $1/f$ and $1/f^3$ power laws. If $|\langle\alpha_i\rangle|/\langle\alpha_i^2\rangle$ increases or decreases from 0.3, the $1/f^2$ power law will gradually change to the $1/f$ power law. Here, the importance of 0.3

is related to the structure of the induction equation. The frequency at which the power law changes depends on $\langle\alpha_i\rangle$. There is a linear relationship between them and $f \approx \langle\alpha_i\rangle$ gives the approximate value of that frequency.

## 4.3 Spectral analyses

Now we will conduct further analysis in attempt to explain the origin of the power laws for the PSDs shown in fig. 4.6. The numerical solution yields nearly the same solution for two components of $\vec{B}$ and a negative solution for the third component. However. these small changes and sign differences do not affect the PSD of any of the components of $\vec{B}$. Because of this, we will consider only the $B_1$ component of $\vec{B}$ in deeper spectral analysis. From eq. 4.6, we can write the following for $B_1$

$$\partial_t B_1 = -(\alpha_2(t) + \alpha_3(t)) \cdot B_1 - B_1^3 + \alpha_1(t) \cdot (B_2 + B_3). \tag{4.7}$$

In the numerical solution, we integrate the right side of the equation. We know that the PSD of $B_1$ is the multiple of the PSD of right hand side and a factor $1/f^2$. This factor $1/f^2$ comes from the integration. So we should firstly look at and analyze the PSD of the right hand side of eq. 4.7. Hereafter, we will use some abbreviations. We will use rhs, ①, ② and ③ for the right hand side, the first term $-(\alpha_2(t)+\alpha_3(t)) \cdot B_1$, the second term $-B_1^3$ and the third term $\alpha_1(t) \cdot (B_2 + B_3)$ on the right hand side, respectively. We will show different combinations of these terms with an addition.

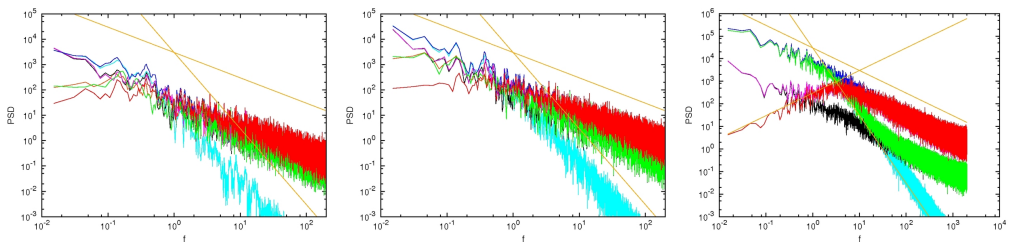


(a) (b) (c)

Fig. 4.8: PSDs of the rhs (red line), ①+② (pink line), ①+③ (orange line), ②+③ (green line), ① (blue line), ② (turquoise line), ③ (black line). Straight lines show the $1/f$, $1/f^3$ and $f$ power laws. a) $\langle\alpha_i\rangle = -0.01$. b) $\langle\alpha_i\rangle = -0.3$. c) $\langle\alpha_i\rangle = -5$.

To analyze rhs, we have calculated all combinations of the terms on the rhs. These calculated spectra are shown in fig. 4.8. We will determine which regime (which combinations of ①, ② and ③) gives the true PSD of rhs. The PSD of a function, in this case rhs,

has complicated properties. It depends on the function type and multiplications and additions can have different effects as well. These effects are complex and can depend on the variances and means of the multiplicatives and additives. Fig. 4.8a shows the PSDs of all combinations of ①, ② and ③ at $\langle \alpha_i \rangle = -0.01$. At high frequencies, the PSD of rhs is same as the PSD of ①+③. In this interval, the PSD of ② is low compared to the other two terms and does not affect the PSD of rhs. The powers of ① and ③ are nearly equal and they both contribute to the PSD of rhs. For the low frequency regime, the PSD of rhs (indicated by the red line) is distinct from all other lines. In this case, no simplification is possible; the only PSD of rhs is itself. In this interval, the PSD of rhs is totally different than the other combinations and its power is less than either of them. Since it exhibits such a complicated property, we will try to explain this later with a detailed analysis. In fig. 4.8b, we see again the PSDs of the same combinations at $\langle \alpha_i \rangle = -0.3$. This case is not very different from the first case. If we consider the high frequency interval, the PSD of rhs is same as the PSD of ①+③. If we consider the low frequency interval, again it is only the PSD of rhs itself. The difference between this case and the first lies in the power law in the low frequency interval. It is $f$ at $\langle \alpha_i \rangle = -0.01$ and constant at $\langle \alpha_i \rangle = -0.3$. This gives the corresponding $1/f$ and $1/f^2$ power laws for $\sqrt{\sum B_i^2}$. Fig. 4.8c shows the PSDs of the same combinations at $\langle \alpha_i \rangle = -5$. Here, we cannot easily separate the frequency into high and low frequency intervals. The PSD of rhs changes its dependence on the different combinations of ①, ② and ③ at a lower frequency than the changing point of the power law of the PSD of rhs. This time change occurs at $f = 0.8$, which is clearly lower than the frequency of the turning point of the PSD of rhs. At frequencies higher than 0.8, the PSD of rhs is same as the PSD of ①+②. At lower frequencies, it is same as the PSD of rhs itself. Now, to be able to understand the different and complex

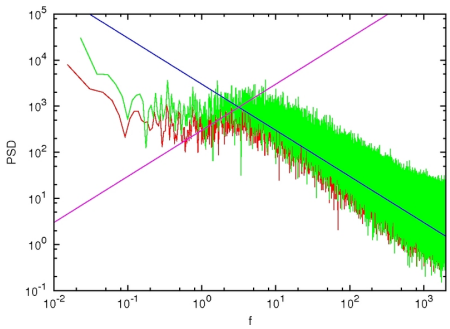


Fig. 4.9: PSDs of the ①+② from direct spectrum calculation (red line) and from the correlation (green line) at $\langle \alpha_i \rangle = -5$. The straight lines represent $f$ and $1/f$.

structure of the low frequency interval, we will first consider low frequencies of the PSD

at $\langle\alpha_i\rangle = -5$. Its different and complicated structure, which can be easily seen in fig. 4.9, deserves a detailed analysis. We will start with a relatively simpler structure in this analysis. The PSD of ①+② also shows a $f$ power law and it includes two terms. It is obviously simpler than full rhs. Since the PSD of ①+② is different than either the PSDs of ① or ② alone, there must be a different relationship among the PSDs in this combination. To be able to understand this different relationship, let us start by writing analytical expressions for PSD of it

$$|-\int_{-\infty}^{\infty}(\alpha_2+\alpha_3)\cdot B_1\cdot e^{-iwt}dt-\int_{-\infty}^{\infty}B_1^3\cdot e^{-iwt}dt|^2=|\int_{-\infty}^{\infty}B_1^3\cdot e^{-iwt}dt|^2 \quad (4.8)$$

$$+|\int_{-\infty}^{\infty}(\alpha_2+\alpha_3)\cdot B_1\cdot e^{-iwt}dt|^2+2\cdot\iint_{-\infty}^{\infty}(\alpha_2+\alpha_3)\cdot B_1(t)\cdot e^{-iwt}B_1^3(t')\cdot e^{iwt'}dtdt'$$

In this equation, we see that there is a cross term in addition to the PSDs of ① and ②. We can use the correlation function to calculate PSD by using the relationship between the correlation and PSD ([Press et al., 1992])

$$G(f)H^*(f)=\int_{-\infty}^{\infty}corr(g,h)\cdot e^{-ift}dt. \quad (4.9)$$

So after calculating the correlation among $(\alpha_2+\alpha_3)\cdot B_1$ and $B_1^3$ we take the Fourier transform to obtain the PSD of these multiplicands. We will use this to calculate the PSD of this multiplication. In this calculation, none of the individual terms give the correct result. The addition of all these terms gives the result that is shown in fig. 4.9. It is obvious that both results in the calculation of PSD are in good agreement.

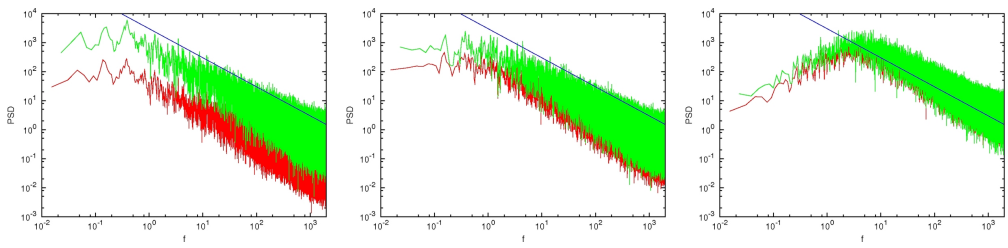


(a) (b) (c)

Fig. 4.10: PSDs of the rhs from direct spectrum calculation (red line) and from the correlation (green line). The straight line represents $1/f$. a) $\langle\alpha_i\rangle = -0.01$ b) $\langle\alpha_i\rangle = -0.3$ c) $\langle\alpha_i\rangle = -5$.

We also calculated rhs' PSD using correlation at $\langle\alpha_i\rangle = -0.01$, $\langle\alpha_i\rangle = -0.3$ and $\langle\alpha_i\rangle = -5$ and observed the same relationship. In fig. 4.10, we see the PSD of rhs from both

direct PSD calculation and correlation calculation. There is also agreement between these two calculation types. This means that all three terms on the right hand side affects the PSD and this effect is observed due to all individual terms and their correlations in the low frequency interval.

# 5 Conclusion

In this work, we investigated numerical simulations of the dynamo and conducted spectral analysis. The dynamo is the accepted mechanism for the generation of the magnetic field in the fluid cores of the cosmological bodies. The generation of the magnetic field takes place in the relevant fluid part of the Earth and also in other cosmological bodies, such as stars, planets and some of the moons in the solar system. The main dynamo process concerns the evolution of the velocity field and subsequent production of a magnetic field from this velocity field. This process can be described by three equations. Within the core, electrically conducting fluid moves under different forces; these forces and the motion of the fluid are described by the Navier-Stokes equation. So it is evident that the Navier-Stokes equation defines how the velocity field evolves under pressure, viscous, Coriolis, Lorentz and buoyancy forces. The induction equation is another important equation because it defines the evolution of the magnetic field. In the induction equation, the evolution of the magnetic field depends on the dissipation of the magnetic field and generation of a magnetic field from the velocity field. The third equation, the heat or buoyancy transport equation, describes the evolution of heat or the buoyancy variable. There are also some other basic relationships arising from the incompressibility of the fluid and the solenoid structure of the magnetic field, which are defined based on the properties of the fluid and structure of the magnetic field, respectively. All the abovementioned equations must be simultaneously solved, a feat which is only possible with computer simulations. Present day computer technology does not enable us to define control parameters within our simulations that are equal to those estimated for Earth. We can only simulate the equations within a narrow range of control parameters.

In this work, we considered two cases for the dynamo process: gravitationally driven dynamos and convection driven dynamos. The difference is seen in the heat equation. It is used as the heat transfer equation in convection driven dynamo and as the buoyancy transport equation in gravitational dynamo. In both cases, convection and gravitation are also at play. The difference between these two dynamo types is related to the source of the

density difference. In the convection driven dynamos it is temperature difference between the boundaries and in the gravitationally driven dynamos it is the solidification of higher density material in the inner boundary. We obtained successful results for both scenarios and also observed magnetic reversals. The dynamo simulations showed that magnetic field generation and reversals are possible from the motion of a conducting fluid. We can understand these magnetic field generation and reversals in a better way by exploring the simulations and the mechanisms described in the work in more detail. Hence, we also conducted spectral analysis. These analyses showed that the distribution of power density over different frequencies can also change with the configuration of control parameters. There are some significant results from the power spectral analysis. One important finding was that the power density decreased with increasing frequency for the magnetic field. This means that long term variations are most important and the contribution of short term variations are less effective. We also observed an agreement between the power law of the PSD of the magnetic field in our simulations with the calculated one for Earth by paleomagnetic research. This agreement occurred at the frequency interval, which shows paleosecular variations, lengths of reversals and excursions. This PSD graph is shown in Section 2.1.5. However, it is hard to say if the $-2$ power law at low frequencies is related to reversals since we also observed this power law in nonreversing cases. Then it should be related to paleosecular variations or excursions. The power distribution in the velocity field was different than the magnetic field. In most cases, we observed nearly equally distributed power in the low frequency range. This shows that due to the forces in the Navier-Stokes equation there are equally distributed fluctuations at small frequencies and each of these fluctuations contribute to the power. This explains our observation of nearly white noise in the low frequency range in most cases. However, in some cases we observed the $-1$ power law, such as in the highest $Ra$ case. We also know that $Ra$ is the ratio of buoyancy force to diffusive forces. The increase in the ratio of buoyancy force against diffusive ones changed this structure and the effect of diffusive forces is weakened and we observed the $-1$ power law. If we consider high frequency interval it was different for both the velocity and magnetic fields. The power laws change in many ways in the high frequency interval and a white noise structure was observed in the highest frequency interval.

Experimental results for spectrum analysis are much different compared to simulation results. In the experiments, the flows or rotation rate of the propellers are either steady or depend on simple rules. This must be one reason for the lack of variations in the velocity field. There are other differences among the simulations and experiments due to

the differences in the control parameters and the shape of the flowing fluid. Resultantly, these fluctuations and differences affect the generation of the magnetic field. These are the possible reasons for the difference between experimental and simulation results.

In the last chapter, we investigated phenomenological models. These models were successful in explaining the power laws. We used only the induction equation in these models and considered the velocity field to be a fluctuating stochastic variable. We chose its power law based on the obtained laws in the dynamo simulations. The analytical considerations explained some cases but there were some instances in which our analytical considerations were not enough. The white noise for the velocity field and the $-2$ power law for the magnetic field combination was obtained by a single magnetic mode model. The $-1$ power law for the velocity field and the $-2$ power law for the magnetic field combination was obtained only by several magnetic modes model. Our starting considerations were not sufficient to explain this last combination. At the end, we concluded that all terms in the induction equation contribute to the power distributions in different ways. Even their correlations are important and we gave analytical and simulated evidence for them.

To sum it up in its entirety, this work contributes to the understanding of the dynamo mechanism. Our gravitationally driven and convection driven dynamo simulations were conducted based on previous works. We analyzed dynamo mostly from the spectral point of view and also investigated a explanatory phenomenological model. The results of this model and dynamo simulations help us to understand magnetic field generation and reversals as well as power spectrum analysis. However, future research and simulations in the dynamo mechanism require improvements in order to obtain results more close to the Earth's case. We will continue our research to obtain more accomplished understanding and results.

# A Simulation results

The following 5 pages contain the simulation results. There is some extra information than previously given tables. The first piece of information is the run duration time. It is given in Earth years. To determine run duration time, we firstly calculated dipole decay time $t_d = \frac{Pm}{E}\left(\frac{r_0}{\pi d}\right)^2$ and the fraction of the total run duration to the calculated dipole decay time. Then we obtained the result by multiplying this fraction by Earth's dipole decay time 20kyr. We also added another part to represent reversing dynamos. In another column time average of the dipole moment is represented. The table also shows $B_{rms}$ and $u_{rms}$ values. $B_{rms}$ is new information compared with previous tables. However, $u_{rms}$ is equal to $Ro$ and we have shown this value in previous tables. Lastly, we have shown the resolution and the time interval of the simulations. We also have shown more simulations similar to the previous situations including some decaying cases. From these shown simulations we can make an extra comment on the reversals that as $Pm$ increases the possibility to have a reversal increases.

In tab. A.1, gravitational dynamos at $E = 6.5{\cdot}10^{-3}$, $Pr = 1$, $Ra = 1{\cdot}10^6$ and $Ra = 5{\cdot}10^5$ with different $Pm$ values are shown. In tab. A.2, gravitational dynamos at $E = 6.5{\cdot}10^{-3}$, $Pr = 1$, $Ra = 1 \cdot 10^5$ with different $Pm$ values are represented. In tab. A.3, gravitational dynamos at $E = 6.5 \cdot 10^{-3}$, $Pr = 1$, $Ra = 3 \cdot 10^5$ and $Ra = 5 \cdot 10^4$ with different $Pm$ values are present. In tab. A.4, we see convection driven dynamos at $E = 6.5 \cdot 10^{-3}$, $Pr = 1$, $Ra = 5 \cdot 10^5$ and $Ra = 1 \cdot 10^5$ and $Ra = 5 \cdot 10^4$ with different $Pm$ values. The last table tab. A.5 shows gravitational dynamos with different $E$. In this table $E$ takes values between $1 \cdot 10^{-4}$ and $1 \cdot 10^{-2}$, $Ra$ can take values between $5 \cdot 10^6$ and $1 \cdot 10^5$ and $Pm$ can take values from 3 to 20. It is obvious that non-decaying dynamo simulations can be carried out in these parameter ranges. However, in some cases, oscillations are so slow that it is not possible to obtain the usual PSD analysis and corresponding power laws.

| $Ra$ ($10^4$) | $E$ ($10^{-3}$) | $Pm$ | t (kyr) | Rev | $B_d$ | $B_{rms}$ | $u_{rms}$ | $\Lambda$ | $Re$ | $Rm$ | L$f$ PL ($B_{rms}$) | H$f$ PL ($B_{rms}$) | L$f$ PL ($u_{rms}$) | H$f$ PL ($u_{rms}$) | Rsl. |
|---|---|---|---|---|---|---|---|---|---|---|---|---|---|---|---|
| 100 | 6.5 | 4.75 | - | - | - | - | - | - | - | - | - | - | - | - | r1t1 |
| | | 5 | 655 | r | $5.26 \cdot 10^{-9}$ | $1.56 \cdot 10^{-4}$ | $4.86 \cdot 10^{-1}$ | 0.00002 | 74.8 | 182 | -2 | -12 | - | -13 | r1t2 |
| | | 5.5 | 435 | r | $-1.61 \cdot 10^{-5}$ | $2.29 \cdot 10^{-2}$ | $4.86 \cdot 10^{-1}$ | 0.442 | 74.7 | 200 | -2 | -11 | - | -13 | r1t2 |
| | | 5.75 | 456 | r | $-6.04 \cdot 10^{-5}$ | $4.79 \cdot 10^{-2}$ | $5.05 \cdot 10^{-1}$ | 2.03 | 77.8 | 226 | -2 | -9 | -1 | -10 | r1t2 |
| | | 6 | 342 | r | $2.68 \cdot 10^{-4}$ | $5.45 \cdot 10^{-2}$ | $5.35 \cdot 10^{-1}$ | 2.74 | 82.4 | 265 | -2 | -8 | -1 | -10 | r1t2 |
| | | 13 | 112 | r | $-3.06 \cdot 10^{-3}$ | $1.91 \cdot 10^{-1}$ | $4.26 \cdot 10^{-1}$ | 73 | 65.5 | 362 | -2 | -7 | -1 | -9 | r1t2 |
| | | 20 | 32.1 | r | $7.20 \cdot 10^{-4}$ | $2.36 \cdot 10^{-1}$ | $3.89 \cdot 10^{-1}$ | 172 | 59.9 | 467 | -2 | -6 | -1 | -8.5 | r1t2 |
| | | 25 | 138 | r | $-5.82 \cdot 10^{-4}$ | $2.52 \cdot 10^{-1}$ | $3.74 \cdot 10^{-1}$ | 244 | 57.5 | 538 | -2 | -6 | -1 | -8.5 | r1t2 |
| | | 35 | 14.1 | r | $-6.84 \cdot 10^{-4}$ | $2.76 \cdot 10^{-1}$ | $3.61 \cdot 10^{-1}$ | 409 | 55.6 | 703 | -1.6 | -5.5 | -1 | -8 | r1t2 |
| 50 | 6.5 | 7 | - | - | - | - | - | - | - | - | - | - | - | - | r2t3 |
| | | 8 | 99.7 | r | $5.22 \cdot 10^{-6}$ | $1.05 \cdot 10^{-2}$ | $3.49 \cdot 10^{-1}$ | 0.135 | 53.6 | 150 | -2 | -8 | -1 | -8 | r2t2 |
| | | 10 | 69.9 | r | $3.83 \cdot 10^{-4}$ | $8.18 \cdot 10^{-2}$ | $3.35 \cdot 10^{-1}$ | 10.3 | 51.5 | 172 | -2 | -8 | -1 | -10 | r2t2 |
| | | 15 | 28.4 | r | $-4.99 \cdot 10^{-4}$ | $4.05 \cdot 10^{-2}$ | $1.35 \cdot 10^{-1}$ | 3.79 | 20.8 | 42.3 | -2 | -7 | -0.8 | -9 | r2t2 |
| | | 20 | 17.4 | r | $1.55 \cdot 10^{-3}$ | $7.25 \cdot 10^{-2}$ | $1.32 \cdot 10^{-1}$ | 16.2 | 20.3 | 53.7 | -2 | -6.5 | -1 | -9 | r2t2 |
| | | 30 | 17 | r | $-1.21 \cdot 10^{-4}$ | $2.05 \cdot 10^{-1}$ | $2.78 \cdot 10^{-1}$ | 194 | 42.8 | 357 | -2 | -6.5 | -1 | -9 | r2t2 |

Tab. A.1: *Gravitational dynamo simulation results. Columns from left to right: The first three columns show Rayleigh, Ekman and magnetic Prandtl numbers Ra, E and Pm respectively. The* $4^{th}$ *column depicts run duration corresponding to Earth's dipole decay time in years. The* $5^{th}$ *column represents the magnetic reversals (r:reversing, non:non-reversing). The* $6^{th}$ *column is the time average of dipole moment. The* $7^{th}$ *and* $8^{th}$ *columns are* $B_{rms}$ *and* $u_{rms}$ *respectively (in our case* $Ro = u_{rms}$ *due to scalings). The next three columns are three output parameters: Elsasser, Reynolds and magnetic Reynolds numbers* $\Lambda$*, Re and Rm, respectively. The next four columns show power laws for* $B_{rms}$ *and* $u_{rms}$ *in low and high frequencies Lf PL and Hf PL, respectively. The last colums stands for resolution (r1:33-64-64, r2:33-128-128 for spatial resolution and t1:*$5 \cdot 10^{-3}$*, t2:*$5 \cdot 10^{-4}$ *and t3:*$1 \cdot 10^{-3}$ *for the time step). The dashes correspond to either decaying cases or non-calculable situations. In all cases, the magnetic Prandtl number is set to 1,* $Pr = 1$.

| $Ra$ ($10^4$) | $E$ ($10^{-3}$) | $Pm$ | t (kyr) | Rev. | $B_d$ | $B_{rms}$ | $u_{rms}$ | $\Lambda$ | $Re$ | $Rm$ | L$f$ PL ($B_{rms}$) | H$f$ PL ($B_{rms}$) | L$f$ PL ($u_{rms}$) | H$f$ PL ($u_{rms}$) | Rsl. |
|---|---|---|---|---|---|---|---|---|---|---|---|---|---|---|---|
| | | 12 | - | - | - | - | - | - | - | - | - | - | - | - | r1t1 |
| | | 12.5 | 2770 | r | $1.41 \cdot 10^{-4}$ | $1.18 \cdot 10^{-2}$ | $1.38 \cdot 10^{-1}$ | 0.266 | 21.3 | 36.7 | -2 | -10 | 0 | -12 | r1t2 |
| | | 13 | 336 | r | $1.71 \cdot 10^{-4}$ | $1.70 \cdot 10^{-2}$ | $1.38 \cdot 10^{-1}$ | 0.580 | 21.2 | 38.1 | -2 | -10 | 0 | -12 | r1t1 |
| | | 13.5 | 2710 | r | $3.60 \cdot 10^{-4}$ | $2.73 \cdot 10^{-2}$ | $1.37 \cdot 10^{-1}$ | 1.55 | 21 | 38.9 | -2 | -10 | 0 | -12 | r1t1 |
| | | 14 | 1400 | r | $-2.39 \cdot 10^{-4}$ | $2.62 \cdot 10^{-2}$ | $1.37 \cdot 10^{-1}$ | 1.48 | 21 | 40.3 | -2 | -9.5 | 0 | -12 | r1t1 |
| | | 15 | 3190 | r | $-4.99 \cdot 10^{-4}$ | $4.05 \cdot 10^{-2}$ | $1.35 \cdot 10^{-1}$ | 3.79 | 20.8 | 42.3 | -2 | -10 | 0 | -12 | r1t1 |
| 10 | 6.5 | 20 | 709 | r | $1.55 \cdot 10^{-3}$ | $7.25 \cdot 10^{-2}$ | $1.32 \cdot 10^{-1}$ | 16.2 | 20.3 | 53.7 | -2 | -9 | 0 | -12 | r2t1 |
| | | 25 | 54.2 | r | $-5.01 \cdot 10^{-3}$ | $9.67 \cdot 10^{-2}$ | $1.33 \cdot 10^{-1}$ | 36 | 20.5 | 68.0 | -2 | -9 | 0 | -12 | r2t3 |
| | | 30 | 128 | r | $-4.89 \cdot 10^{-3}$ | $1.05 \cdot 10^{-1}$ | $1.34 \cdot 10^{-1}$ | 51 | 20.5 | 82.3 | -2 | -9 | 0 | -12 | r2t1 |
| | | 35 | 196 | r | $5.99 \cdot 10^{-4}$ | $1.13 \cdot 10^{-1}$ | $1.33 \cdot 10^{-1}$ | 68.9 | 20.5 | 95.5 | -2 | -9 | 0 | -11 | r2t1 |
| | | 50 | 132 | r | $1.08 \cdot 10^{-3}$ | $1.30 \cdot 10^{-1}$ | $1.32 \cdot 10^{-1}$ | 130 | 20.3 | 134 | -2 | -9 | 0 | -11 | r2t1 |
| | | 70 | 94.7 | r | $1.27 \cdot 10^{-3}$ | $1.47 \cdot 10^{-1}$ | $1.30 \cdot 10^{-1}$ | 231 | 19.9 | 181 | -2 | -8 | 0 | -10 | r2t1 |
| | | 100 | 62.8 | r | $8.34 \cdot 10^{-4}$ | $1.58 \cdot 10^{-1}$ | $1.27 \cdot 10^{-1}$ | 386 | 19.6 | 249 | -2 | -7 | 0 | -11 | r2t1 |

Tab. A.2: *Gravitational dynamo simulation results. Columns from left to right: The first three columns show Rayleigh, Ekman and magnetic Prandtl numbers Ra, E and Pm respectively. The* $4^{th}$ *column depicts run duration corresponding to Earth's dipole decay time in years. The* $5^{th}$ *column represents the magnetic reversals (r:reversing, non:non-reversing). The* $6^{th}$ *column is the time average of dipole moment. The* $7^{th}$ *and* $8^{th}$ *columns are* $B_{rms}$ *and* $u_{rms}$ *respectively (in our case* $Ro = u_{rms}$ *due to scalings). The next three columns are three output parameters: Elsasser, Reynolds and magnetic Reynolds numbers* $\Lambda$*, Re and Rm, respectively. The next four columns show power laws for* $B_{rms}$ *and* $u_{rms}$ *in low and high frequencies Lf PL and Hf PL, respectively. The last colums stands for resolution (r1:33-64-64, r2:33-128-128 for spatial resolution and t1:*$5 \cdot 10^{-3}$*, t2:*$5 \cdot 10^{-4}$ *and t3:*$1 \cdot 10^{-3}$ *for the time step). The dashes correspond to either decaying cases or non-calculable situations. In all cases, the magnetic Prandtl number is set to 1,* $Pr = 1$.

| $Ra$ ($10^4$) | $E$ ($10^{-3}$) | $Pm$ | t (kyr) | Rev. | $B_d$ | $B_{rms}$ | $u_{rms}$ | $\Lambda$ | $Re$ | $Rm$ | L$f$ PL ($B_{rms}$) | H$f$ PL ($B_{rms}$) | L$f$ PL ($u_{rms}$) | H$f$ PL ($u_{rms}$) | Rsl. |
|---|---|---|---|---|---|---|---|---|---|---|---|---|---|---|---|
| 30 | 6.5 | 8 | - | - | - | - | - | - | - | - | - | - | - | - | r2t1 |
| | | 9 | 619 | r | $1.28 \cdot 10^{-4}$ | $1.45 \cdot 10^{-2}$ | $2.58 \cdot 10^{-1}$ | 0.292 | 39.6 | 91.9 | -2 | -9 | 0 | -11 | r2t1 |
| | | 10 | 98 | r | $3.01 \cdot 10^{-4}$ | $6.96 \cdot 10^{-2}$ | $2.48 \cdot 10^{-1}$ | 7.45 | 38.2 | 94.9 | -2 | -9 | -1 | -11 | r2t2 |
| | | 20 | 23.2 | r | $2.48 \cdot 10^{-3}$ | $1.40 \cdot 10^{-1}$ | $2.32 \cdot 10^{-1}$ | 60 | 35.7 | 166 | -2 | -7 | -1 | -9 | r2t2 |
| | | 30 | 129 | r | $-1.54 \cdot 10^{-3}$ | $6.01 \cdot 10^{-2}$ | $8.51 \cdot 10^{-2}$ | 16.7 | 13.1 | 33.5 | -2 | -7 | -0.8 | -10 | r2t2 |
| 5 | 6.5 | 7 | 1340 | non | $-6.56 \cdot 10^{-3}$ | $1.70 \cdot 10^{-2}$ | $9.69 \cdot 10^{-2}$ | 0.313 | 14.9 | 10.1 | -2 | -11 | 0 | -13 | r2t1 |
| | | 8 | 188 | non | $-6.54 \cdot 10^{-3}$ | $1.82 \cdot 10^{-2}$ | $9.73 \cdot 10^{-2}$ | 0.408 | 15 | 11.7 | -2 | -11 | 0 | -13 | r2t3 |
| | | 10 | 857 | non | $-5.65 \cdot 10^{-3}$ | $1.82 \cdot 10^{-2}$ | $9.70 \cdot 10^{-2}$ | 0.508 | 14.9 | 14.5 | -2 | -11 | 0 | -13 | r2t1 |
| | | 12 | 114 | non | $-5.62 \cdot 10^{-3}$ | $2.05 \cdot 10^{-2}$ | $9.64 \cdot 10^{-2}$ | 0.778 | 14.8 | 17.2 | -2 | -11 | 0 | -13 | r2t3 |
| | | 15 | 232 | non | $-3.21 \cdot 10^{-3}$ | $1.40 \cdot 10^{-2}$ | $9.77 \cdot 10^{-2}$ | 0.455 | 15 | 22 | -2 | -11 | 0 | -15 | r2t1 |
| | | 20 | 149 | non | $-2.57 \cdot 10^{-3}$ | $1.41 \cdot 10^{-2}$ | $9.76 \cdot 10^{-2}$ | 0.614 | 15 | 29.3 | -2 | -11 | 0 | -15 | r2t1 |
| | | 30 | 129 | r | $-1.54 \cdot 10^{-3}$ | $6.01 \cdot 10^{-2}$ | $8.51 \cdot 10^{-2}$ | 16.7 | 13.1 | 33.5 | -2 | -9 | 0 | -14 | r2t1 |

Tab. A.3: *Gravitational dynamo simulation results. Columns from left to right: The first three columns show Rayleigh, Ekman and magnetic Prandtl numbers Ra, E and Pm respectively. The* $4^{th}$ *column depicts run duration corresponding to Earth's dipole decay time in years. The* $5^{th}$ *column represents the magnetic reversals (r:reversing, non:non-reversing). The* $6^{th}$ *column is the time average of dipole moment. The* $7^{th}$ *and* $8^{th}$ *columns are* $B_{rms}$ *and* $u_{rms}$ *respectively (in our case* $Ro = u_{rms}$ *due to scalings). The next three columns are three output parameters: Elsasser, Reynolds and magnetic Reynolds numbers* $\Lambda$*, Re and Rm, respectively. The next four columns show power laws for* $B_{rms}$ *and* $u_{rms}$ *in low and high frequencies Lf PL and Hf PL, respectively. The last colums stands for resolution (r1:33-64-64, r2:33-128-128 for spatial resolution and t1:*$5 \cdot 10^{-3}$*, t2:*$5 \cdot 10^{-4}$ *and t3:*$1 \cdot 10^{-3}$ *for the time step). The dashes correspond to either decaying cases or non-calculable situations. In all cases, the magnetic Prandtl number is set to 1,* $Pr = 1$.

| $Ra$ ($10^4$) | $E$ ($10^{-3}$) | $Pm$ | t (kyr) | Rev. | $B_d$ | $B_{rms}$ | $u_{rms}$ | $\Lambda$ | $Re$ | $Rm$ | L$f$ PL ($B_{rms}$) | H$f$ PL ($B_{rms}$) | L$f$ PL ($u_{rms}$) | H$f$ PL ($u_{rms}$) | Rsl. |
|---|---|---|---|---|---|---|---|---|---|---|---|---|---|---|---|
| 50 | 6.5 | 5 | 57.4 | non | $-1.82 \cdot 10^{-2}$ | $1.84 \cdot 10^{-1}$ | $5.17 \cdot 10^{-1}$ | 26.1 | 79.6 | 206 | -2 | -8 | 0 | -10 | r2t2 |
| | | 10 | 80.7 | r | $2.91 \cdot 10^{-3}$ | $2.68 \cdot 10^{-1}$ | $4.78 \cdot 10^{-1}$ | 110 | 73.5 | 351 | -2 | -7 | -1&0 | -9 | r2t2 |
| | | 20 | 18.8 | r | $4.64 \cdot 10^{-3}$ | $3.08 \cdot 10^{-1}$ | $4.51 \cdot 10^{-1}$ | 292 | 69.4 | 627 | -2 | -6 | -1&0 | -8 | r2t2 |
| | | 30 | 10.8 | r | $8.22 \cdot 10^{-4}$ | $3.34 \cdot 10^{-1}$ | $4.39 \cdot 10^{-1}$ | 516 | 67.5 | 888 | -1.6 | -6 | -1&0 | -8 | r2t2 |
| 10 | 6.5 | 5 | 359 | r | $9.85 \cdot 10^{-5}$ | $6.70 \cdot 10^{-3}$ | $2.12 \cdot 10^{-1}$ | 0.035 | 32.6 | 34.6 | -2 | -10 | 0 | -12 | r2t1 |
| | | 10 | 35.9 | r | $1.55 \cdot 10^{-3}$ | $1.08 \cdot 10^{-1}$ | $1.96 \cdot 10^{-1}$ | 17.8 | 30.1 | 58.9 | -2.5 | -8 | 0 | -10 | r2t2 |
| | | 20 | 43.9 | r | $-2.93 \cdot 10^{-4}$ | $1.36 \cdot 10^{-1}$ | $1.87 \cdot 10^{-1}$ | 57 | 28.7 | 107 | -2 | -8 | 0 | -9 | r2t2 |
| | | 30 | 12.6 | r | $-1.08 \cdot 10^{-2}$ | $1.80 \cdot 10^{-1}$ | $1.76 \cdot 10^{-1}$ | 150 | 27.1 | 144 | -2.5 | -8 | 0 | -9 | r2t2 |
| 5 | 6.5 | 10 | 377 | r | $7.49 \cdot 10^{-5}$ | $3.65 \cdot 10^{-3}$ | $1.25 \cdot 10^{-1}$ | 0.021 | 19.3 | 24.2 | -2 | -10 | 0 | -14 | r2t1 |
| | | 20 | 251 | r | $4.74 \cdot 10^{-3}$ | $7.83 \cdot 10^{-2}$ | $1.14 \cdot 10^{-1}$ | 18.9 | 17.6 | 40.2 | -2 | -8 | 0 | -10 | r2t1 |
| | | 30 | 239 | r | $-4.19 \cdot 10^{-3}$ | $1.02 \cdot 10^{-1}$ | $1.09 \cdot 10^{-1}$ | 48.1 | 16.8 | 54.9 | -2 | -8 | -0.6 | -9 | r2t1 |

Tab. A.4: *Convection driven dynamo simulation results. Columns from left to right: The first three columns show Rayleigh, Ekman and magnetic Prandtl numbers Ra, E and Pm respectively. The* $4^{th}$ *column depicts run duration corresponding to Earth's dipole decay time in years. The* $5^{th}$ *column represents the magnetic reversals (r:reversing, non:non-reversing). The* $6^{th}$ *column is the time average of dipole moment. The* $7^{th}$ *and* $8^{th}$ *columns are* $B_{rms}$ *and* $u_{rms}$ *respectively (in our case* $Ro = u_{rms}$ *due to scalings). The next three columns are three output parameters: Elsasser, Reynolds and magnetic Reynolds numbers* $\Lambda$*, Re and Rm, respectively. The next four columns show power laws for* $B_{rms}$ *and* $u_{rms}$ *in low and high frequencies Lf PL and Hf PL, respectively. The last colums stands for resolution (r1:33-64-64, r2:33-128-128 for spatial resolution and t1:*$5 \cdot 10^{-3}$*, t2:*$5 \cdot 10^{-4}$ *and t3:*$1 \cdot 10^{-3}$ *for the time step). In all cases, the magnetic Prandtl number is set to 1,* $Pr = 1$.

| $Ra$ ($10^4$) | $E$ ($10^{-3}$) | $Pm$ | t (kyr) | Rev. | $B_d$ | $B_{rms}$ | $u_{rms}$ | $\Lambda$ | $Re$ | $Rm$ | L$f$ PL ($B_{rms}$) | H$f$ PL ($B_{rms}$) | L$f$ PL ($u_{rms}$) | H$f$ PL ($u_{rms}$) | Rsl. |
|---|---|---|---|---|---|---|---|---|---|---|---|---|---|---|---|
| 500 | 0.1 | 20 | 0.45 | non | $-8.06 \cdot 10^{-5}$ | $1.46 \cdot 10^{-2}$ | $1.95 \cdot 10^{-2}$ | 42.5 | 195 | 75.8 | -2 | -12 | -1 | -11 | r2t2 |
| 100 | 1 | 3 | 78.8 | non | $-3.73 \cdot 10^{-3}$ | $1.02 \cdot 10^{-2}$ | $4.52 \cdot 10^{-2}$ | 0.315 | 45.2 | 6.14 | -2 | -12 | 0 | -13 | r1t2 |
| | | 5 | 54.4 | non | $-5.96 \cdot 10^{-3}$ | $2.19 \cdot 10^{-2}$ | $4.34 \cdot 10^{-2}$ | 2.4 | 43.4 | 9.43 | -2 | -9 | 0 | -14 | r1t2 |
| | | 10 | 22.3 | non | $-7.81 \cdot 10^{-3}$ | $4.04 \cdot 10^{-2}$ | $3.92 \cdot 10^{-2}$ | 16.3 | 39.2 | 15.4 | -2 | -8 | 0 | -10 | r1t2 |
| | 0.1 | 20 | 2.17 | non | $-1.60 \cdot 10^{-4}$ | $1.62 \cdot 10^{-3}$ | $4.62 \cdot 10^{-5}$ | 0.525 | 0.46 | 0.0004 | - | - | - | - | r2t1 |
| | 0.3 | 3 | - | - | - | - | - | - | - | - | - | - | - | - | r2t4 |
| | | 10 | 20.4 | non | $9.29 \cdot 10^{-5}$ | $9.86 \cdot 10^{-4}$ | $8.24 \cdot 10^{-3}$ | 0.0324 | 27.5 | 2.26 | -2 | -8 | 0 | -12 | r2t1 |
| | | 20 | 7.86 | r | $-2.86 \cdot 10^{-5}$ | $7.09 \cdot 10^{-3}$ | $8.68 \cdot 10^{-3}$ | 3.35 | 28.9 | 5.02 | -3 | -7 | -1 | -7 | r2t1 |
| 95 | 0.3 | 3 | 42.3 | non | $-2.58 \cdot 10^{-6}$ | $6.73 \cdot 10^{-6}$ | $8.41 \cdot 10^{-3}$ | $45 \cdot 10^{-8}$ | 28.1 | 0.71 | - | - | - | - | r1t2 |
| 41 | 0.3 | 10 | - | - | - | - | - | - | - | - | - | - | - | - | r2t1 |
| | | 20 | 14.7 | non | $8.81 \cdot 10^{-5}$ | $3.64 \cdot 10^{-4}$ | $3.20 \cdot 10^{-3}$ | 0.0089 | 10.7 | 0.68 | - | - | - | - | r2t1 |
| 30 | 1 | 10 | 20.2 | non | $-2.04 \cdot 10^{-2}$ | $4.58 \cdot 10^{-2}$ | $1.73 \cdot 10^{-2}$ | 21 | 17.3 | 2.98 | - | - | - | - | r1t2 |
| 10 | 10 | 14 | 2346 | r | $3.89 \cdot 10^{-4}$ | $6.76 \cdot 10^{-2}$ | $2.29 \cdot 10^{-1}$ | 6.41 | 22.9 | 73.2 | -2 | -10 | 0 | -12 | r1t1 |
| | | 20 | 52.3 | r | $4.06 \cdot 10^{-3}$ | $1.17 \cdot 10^{-1}$ | $2.21 \cdot 10^{-1}$ | 27.5 | 22.1 | 97.6 | -2 | -8 | 0 | -10 | r2t2 |

Tab. A.5: *Gravitational dynamo simulation results. Columns from left to right: The first three columns show Rayleigh, Ekman and magnetic Prandtl numbers $Ra$, $E$ and $Pm$ respectively. The $4^{th}$ column depicts run duration corresponding to Earth's dipole decay time in years. The $5^{th}$ column represents the magnetic reversals (r:reversing, non:non-reversing). The $6^{th}$ column is the time average of dipole moment. The $7^{th}$ and $8^{th}$ columns are $B_{rms}$ and $u_{rms}$ respectively (in our case $Ro = u_{rms}$ due to scalings). The next three columns are three output parameters: Elsasser, Reynolds and magnetic Reynolds numbers $\Lambda$, $Re$ and $Rm$, respectively. The next four columns show power laws for $B_{rms}$ and $u_{rms}$ in low and high frequencies L$f$ PL and H$f$ PL, respectively. The last colums stands for resolution (r1:33-64-64, r2:33-128-128 for spatial resolution and t1:$5 \cdot 10^{-3}$, t2:$5 \cdot 10^{-4}$, t3:$1 \cdot 10^{-3}$ and t4:$5 \cdot 10^{-2}$ for the time step). The dashes correspond to either decaying cases or non-calculable situations. In all cases, the magnetic Prandtl number is set to 1, $Pr = 1$.*

# Bibliography

[Acheson, 1990] Acheson, D. J. (1990) *Elementary fluid dynamics* Oxford University Press.

[Barenghi and Jones, 1991] Barenghi, C. F. and Jones, C. A. (1991) *Nonlinear planetary dynamos in a rotating spherical shell I. Numerical Methods* Geophysical and Astrophysical Fluid Dynamics, Vol. 60.

[Barenghi, 1992] Barenghi, C. F. (1992) *Nonlinear planetary dynamos in a rotating spherical shell. II. The post-Taylor equilibration for Alpha-squared-dynamos* Geophysical and Astrophysical Fluid Dynamics, Vol. 67.

[Batchelor, 1967] Batchelor, G. K. (1967) *An introduction to fluid dynamics* Cambridge University Press.

[Bone, 2007] Bone, N. (2007) *Aurora: observing and recording nature's spectacular light show* Springer Science + Business Media, LLC.

[Bourgoin et al., 2006] Bourgoin et al. (2006) *An experimental Bullard-von Karman dynamo* New Journal of Physics, Vol. 8.

[Bourgoin et al., 2002] Bourgoin, M. et al., (2002) *Magnetohydrodynamics measurements in the von Karman sodium experiment* Physics of Fluids, Vol. 14.

[Brown et al., 1992] Brown, G., Hawkesworth, C. and Wilson, C. (1992) *Understanding the Earth* Cambridge University Press.

[Buffett, 2009] Buffett, B. (2009) *Geodynamo: A matter of boundaries* Nature Geoscience 2.

[Busse et al., 1998] Busse, F. H., Grote, E. and Tilgner, A. (1998) *On Convection Driven Dynamos in Rotating Spherical Shells* Studia Geophysica et Geodaetica, Vol. 42.

[Cande and Kent, 1995] Cande, S.C. and Kent, D.V. (1995) *Revised calibration of the geomagnetic polarity timescale for the late Cretaceous and Cenozoic* Journal of Geophysical Researches, Vol. 100.

[Channell, 1999] Channell, J.E.T. (1999) *Geomagnetic paleointensity and directional secular variation at Ocean Drilling Program (ODP) Site 984 (Bjorn Drift) since 500 ka; comparisons with ODP Site 983 (Gardar Drift).* Journal of Geophysical Researches B, Vol. 104.

[Childress and Gilbert, 1995] Childress, S. and Gilbert, D. (1995) *Stretch, twist, fold: the fast dynamo* Springer-Verlag Berlin Heidelberg.

[Childress and Soward, 1972] Childress, S. and Soward, A. M. (1972) *Convection-Driven Hydromagnetic Dynamo* Physical Review Letters, 29.

[Christensen and Aubert, 2006] Christensen, U. R. and Aubert, J. (2006) *Scaling properties of convection-driven dynamos in rotating spherical shells and application to planetary magnetic fields* Geophysical Journal International, Vol. 166.

[Constable et al., 1998] Constable, C.G., Tauxe, L. and Parker, R.L. (1998) *Analysis of 11 Myr of geomagnetic intensity variation.* Journal of Geophysical Researches, Vol. 103.

[Constable and Johnson, 2005] Constable, C. and Johnson, C. (2005) *A paleomagnetic power spectrum* Physics of the Earth and Planetary Interiors, Vol. 153.

[Cox, 1969] Cox, A. (1969) *Geomagnetic Reversals* Science, Vol. 163.

[Davidson, 2001] Davidson, P. A. (2001) *An introduction to magnetohydrodynamics* Cambridge University Press.

[Dreizler and Ludde, 2010] Dreizler, R. M. and Ludde, C. S. (2010) *Theoretical Mechanics. Graduate Texts in Physics* Springer-Verlag Berlin Heidelberg.

[Dyer, 2001] Dyer, S. A. (2001) *Survey of instrumentation and measurement* John Wiley & Sons.

[Fix, 2004] Fix, J. D. (2004) *Astronomy: Journey to the Cosmic Frontier* The McGraw-Hill Companies, Inc.

[Gailitis et al., 2004] Gailitis, A., Lielausis, O., Platacis, E., Gerbert, G. and Stefani, F. (2004) *Riga dynamo experiment and its theoretical background* Physics of Plasmas, Vol. 11.

[Gailitis et al., 2003] Gailitis, A., Lielausis, O., Platacis, E., Gerbert, G. and Stefani, F. (2003) *The Riga dynamo experiment* Surveys in geophysic, Vol. 24.

[Gailitis et al., 2001] Gailitis et al. (2001) *Magnetic Field Saturation in the Riga Dynamo Experiment* Physical Review Letters, Vol. 86.

[Guyodo and Valet, 1999] Guyodo, Y. and Valet, J.P. (1999) *Global changes in geomagnetic intensity during the past 800 thousand years.* Nature 399.

[Hollerbach and Ierley, 1991] Hollerbach, R. and Ierley, G. R. (1991) *Nonlinear planetary dynamos in a rotating spherical shell I. Numerical Methods* Geophysical and Astrophysical Fluid Dynamics, Vol. 56.

[Jackson, 1962] Jackson, J. D., (1962) *Classical Electrodynamics* John Wiley & Sons., Inc.

[Jacobs, 1994] Jacobs, J. A. (1994) *Reversals of the Earth's Magnetic Field* Cambridge University Press.

[Jacobs, 1987] Jacobs, J. A. (1987) *Geomagnetism* Academic Press.

[Jones, 2000] Jones, C. A. (2000) *Convection-driven geodynamo models* Philosophical Transactions of Royal Society A, Vol. 358.

[Jones and Roberts, 2000] Jones, C. A. and Roberts, P. H. (2000) *Convection-driven dynamos in a rotating plane layer* Journal of Fluid Mechanics, Vol. 404.

[Kasdin, 1995] Kasdin, N. J. (1995) *Discrete simulation of colored noise and stochastic processes and* $1/f^{\alpha}$ *power law noise generation* Proceedings of the IEEE, Vol. 83.

[Korte and Constable, 2005] Korte, M. and Constable, C.G. (2005) *Continuous geomagnetic models for the past 7 millennia* Geochemistry Geophysics Geosystems, Vol. 6.

[Krause and Radler, 1980] Krause, F. and Radler, K. H. (1980) *Mean-Field Magnetohydrodynamicsand Dynamo Theory* New York: Pergamon.

[Kundu and Cohen, 2002] Kundu, P. K. and Cohen, I. M. (2002) *Fluid mechanics* Academic Press.

[Kutzner and Christensen, 2002] Kutzner, C. and Christensen, U. R. (2002) *From stable dipolar towards reversing numerical dynamos* Physics of the Earth and Planetary Interiors, Vol. 131.

[Lister and Buffett, 1995] Lister, J. R. and Buffett, B. A. (1995) *The strength and efficiency of thermal and compositional convection in the geodynamo* Physics of the Earth and Planetary Interiors, Vol. 91.

[Loper, 2007] Loper, D. E. (2007) *The gravitationally powered dynamo* Geophysical Journal of the Royal Astronomical Society, Vol. 54.

[McFadden, 2007] McFadden, L. A. L. (2007) *Encyclopedia of the Solar System* Elsevier Inc.

[McElhinny and McFadden, 2000] McElhinny, M. W. and McFadden, P. L. (2000) *Paleomagnetism: Continents and Oceans* Academic Press.

[McMillan et al., 2004] McMillan, D.G., Constable, C.G. and Parker, R.L. (2004) *Assessing the dipolar signal in stacked paleointensity records using a statistical error model and geodynamo simulations* Physics of The Earth and Planetary Interiors, Vol. 145.

[Merrill and McElhinny, 1983] Merrill, R. and McElhinny, M. (1983). *The Earth's Magnetic Field: Its History, Origin and Planetary Perspective* Academic Press London.

[Merrill et al., 1998] Merrill, R. T., McElhinny, M. W. and McFadden, P. L. (1998) *The magnetic field of the earth: paleomagnetism, the core, and the deep mantle* Academic Press.

[Monchaux et al., 2009] Monchaux, R. et al., (2009) *The von Karman Sodium experiment: Turbulent dynamical dynamos* Physics of Fluids, Vol. 21.

[Moreau] Moreau, J. P. *A Fortran Code Filtering a signal F(t) by Butterworth method* http://jean-pierre.moreau.pagesperso-orange.fr/Fortran/tfilters_f90.txt

[Muller et al., 2002] Muller, U., Stieglitz, R. and Horanyi, S. (2002) *The Karlsruhe Dynamo Experiment* Forschungszentrum Karlsruhe GmbH Postfach 3640, 76021 Karlsruhe.

[Mueller and Stieglitz, 2003] Mueller, U. and Stieglitz, R. (2003) *The geodynamo: Models and supporting experiments* http://bibliothek.fzk.de/zb/berichte/FZKA6797.pdf

[Olson, 2007] Olson, P. (2007) Gravitational dynamos and the low-frequency geomagnetic secular variation Proceeding of the Natural Academy of Sciences, Vol. 104.

[Olson and Christensen, 2006] Olson, P. and Christensen, U. R. (2006) *Dipole moment scaling for convection-driven planetary dynamos* Earth and Planetary Science Letters, Vol. 250.

[Pater and Lissauer, 2001] de Pater, I. and Lissauer, J. J. (2001) *Planetary Sciences* Cambridge University Press.

[Pedlosky, 1979] Pedlosky, J. (1979) *Geophysical fluid dynamics* Springer-Verlag New York Inc.

[Pekeris et al., 1973] Pekeris, C. L., Accad, Y. and Shkoller, B. (1973) *Kinematic Dynamos and the Earth's Magnetic Field* Philosophical Transactions of Royal Society A, Vol. 275.

[Press et al., 1992] Press, W. H., Teukolsky, S. A., Vetterling, W. T. and Flannery, B. P. (1992) *Numerical Recipes in fortran* Cambridge university press.

[Rabiner and Gold, 1975] Rabiner, L. R. and Gold, B. (1975) *Theory and Application of Digital Signal Processing* Englewood Cliffs, New Jersey: Prentice-Hall.

[Roberts, 1972] Roberts, P. H. (1972) *Kinematic Dynamo Models* Philosophical Transactions of Royal Society A, Vol. 272.

[Rose and Kindersley, 2000] Rose, C. and Kindersley, D. (2000) *Earth's structure* http://mediatheek.thinkquest.nl/ ll125/en/fullstruct.htm

[Russell, 1999] Russell, C. T. (1999) *Magnetic Stress in Solar System Plasmas* Australian Journal of Physics, Vol. 52.

[D. Schmitt, 2009] Schmitt, D. (2009) *Lecture: Geomagnetic dynamo theory* http://www.solar-system-school.de/

[Schubert et al., 2001] Schubert, G., Turcotte, D. L. and Olson, P. (2001) *Mantle convection in the earth and planets* Cambridge University Press.

[Stieglitz and Muller, 2001] Stieglitz, R. and Muller, U.(2001) *Experimental demonstration of a homogeneous two-scale dynamo* Physics of Fluids, Vol. 13.

[Soward and Jones, 2005] Soward, A. M and Jones, C. A. (2005) *Alpha-squared-dynamos and Taylor's constraint* Geophysical and Astrophysical Fluid Dynamics, Vol. 27.

[Soward, 1974] Soward, A. M. (1974) *A Convection-Driven Dynamo: I. The Weak Field Case* Philosophical Transactions of Royal Society A, Vol. 275.

[Tanriverdi and Tilgner, 2011] Tanriverdi, V. and Tilgner, A. (2011) *Global fluctuations in magnetohydrodynamic dynamos* New Journal of Physics, Vol. 13.

[Tilgner, 1997] Tilgner, A. (1997) *A kinematic dynamo with a small scale velocity field* Physics Letters A, Vol. 226.

[Tilgner, 1999] Tilgner, A. (1999) *Spectral mthods for the simulation of imcompressible flows in spherical shells* International Journal for Numerical Methods in Fluids, Vol. 30.

[Tilgner, 2005] Tilgner, A. (2005) *Precession driven dynamos* Physics of Fluids, Vol. 17.

[Tritton, 1988] Tritton, D. J. (1988) *Physical fluid dynamics* Oxford University Press.

[Valet and Meynadier, 1993] Valet, J.-P. and Meynadier, L. (1993) *Geomagnetic field intensity and reversals during the last four million years* Nature 366.

[Volk et al., 2006] Volk, R., Odier, P. and Pinton, J. F. (2006) *Fluctuation of magnetic induction in von Karman swirling flows* Physics of Fluids, Vol. 18.

[Wu and Roberts, 2008] Wu, C. C. and Roberts, P. H. (2008) *A precessionally-driven dynamo in a plane layer* Geophysical and Astrophysical Fluid Dynamics, Vol. 102.

[Zhang et al., 2010] Zhang, K., Chan, K. H. and Liao, X. (2010) *On fluid flows in precessing spheres in the mantle frame of reference* Physics of Fluids, Vol. 22.

You have been a prisoner

of a little pond

I am the ocean

and its turbulent flood

Come merge with me

leave this world of ignorance

Be with me,

I will open the gate to your love.

Mevlana Celaleddin-i Rumi

# Acknowledgments

I would like to thank my supervisor Prof. Andreas Tilgner. He had played a significant role in the completion of this thesis. During the three and half year of my work he always had time for discussion. His kindness was one of the nicest things in the Göttingen for me.

I would also like to thank Prof. Wolfgang Glatzel for being my co-supervisor and his kind attitudes. I would like to thank Prof. Kneer, Prof. Gizon and Dr. Reiners. Special thanks to Dr. Dieter Schmitt, the International Max-Planck Researches School coordinator, for his help and support.

I am also thankful to my colleagues Ellen, Mark, Ronny, Konstantin, Simon, Niels and others in our institute and Rainer, Einike, Frau Eggert-Heise, Manfred, Alexandra...

I want to also say thanks to Nicole.

Göttingen'de tanıştığım Türk arkadaşlarım Emre, Nilda, Eren, Cansu, Mehmet, Sibel, Erdem ve diğer tüm arkadaşlarıma da ayrıca teşekkür etmek isterim.

Birlikte eğlendiğimiz, güzel zamanlar paylaştımız arkadaşlarım Rengin, Döndü, Haydar, Emel, İlker, Barış size buradan bir kez daha güzellikler dilerim :)

Benim için en önemli kısmı, son kısmı, aileme ayırmak istedim. Anneme ve babama destekleri ve iyi dilekleri için ayrı ayrı sevgiyle teşekkür ederim. En küçükleri olarak kardeşlerim Ali, Ayşe, Nuray, Reyhan ve Hürol'a ve onların eşlerine varlıkları ve yanımda oldukları icin teşekkür ederim. Kuzenlerime ve diğer yakınlarıma da ayrıca teşekkür eder ve güzellikler dilerim. Benim için farklı bir anlamları ve yerleri olan, her birine hissettiğim farklı bir sevgiyle yeğenlerime, hayata ve hayatıma kattıkları ve katacakları güzellikler için kucak dolusu sevgilerimi dile getiririm. Arda, Berkay, Buse, Büşra, Efe, Erhan, Fırat, İdil, İkbal, Süleyman ve Duru, benim dünya tatlısı yeğenlerim, hepinize güzelliklerle, sevgiyle, iyilikle dolu bir ömür dilerim :)

Many thanks... Çooook teşekkürler...

# Lebenslauf

**Persönliche Daten:**

| | |
|---|---|
| Name: | Vedat Tanrıverdi |
| geboren: | 20. February 1979 in Sorgun |
| Staatsangehörigkeit: | Türke |
| Familienstand: | ledig |

**Schulbildung:**

| | |
|---|---|
| 09. 1985 - 07. 1990: | Bahadın İlköğretim İlkokulu, Bahadın |
| 08. 1990 - 06. 1993: | Bahadın Ortaokulu, Bahadın |
| 08. 1993 - 06. 1995: | Keçiören Çevre Sağlık Meslek Lisesi, Ankara |
| 08. 1995 - 06. 1997: | Torbalı Sağlık Meslek Lisesi, Torbalı |

**Studium:**

| | |
|---|---|
| 10. 1997 - 07. 2002: | B.Sc. in Physics METU, ANKARA |
| 09. 2002 - 03. 2004: | M.Sc. in Physics METU, ANKARA |
| 04. 2004 - 01. 2008: | PhD. in Physics METU, ANKARA(Not finished) |
| 01. 2008 - 07. 20011: | Promotion am Institut für Geophysik der Universitat Göttingen |